Ph.D. DISSERTATION

Electrical and Interfacial Characterization of GaSb MOS Capacitors by Using Sulfuric Passivation, and Post- and Pre-Deposition Rapid Thermal Process

황화 부동화와 후증착 및 전증착 열처리를 이용한
갈륨안티모나이드 MOS 축전기의 전기적 계면적 특성

by

Seongkyung Kim

August 2017

DEPARTMENT OF MATERIALS SCIENCE AND ENGINEERING

COLLEGE OF ENGINEERING

SEOUL NATIONAL UNIVERSITY

Electrical and Interfacial Characterization of GaSb MOS Capacitors by Using Sulfuric Passivation, and Post- and Pre-Deposition Rapid Thermal Process

Advisor : Prof. Hyeong Joon Kim

by

Seongkyung Kim

A thesis submitted to the Graduate Faculty of Seoul National University in partial fulfillment of the requirements for the Degree of Doctor of Philosophy
Department of Materials Science and Engineering

August 2017

Approved
by

Chairman of Advisory Committee : Cheol Seong Hwang
Vice-chairman of Advisory Committee : Hyeong Joon Kim
Advisory Committee : Young-Chang Joo
Advisory Committee : Jae Kyeong Jeong
Advisory Committee : Hajin Lim

Abstract

GaSb has attracted significant attention as a strong channel candidate for next generation nanoscale logic metal oxide semiconductor field-effect transistors (MOSFETs), since it has extraordinary hole mobility(~ 3000 cm^2/Vs) compared to conventional silicon devices, chemical resistance of its native oxides towards water, and high effective density of states(1.8×10^{19} cm^{-3}). However, there are some drawbacks to adopt GaSb to the MOSFETs such as high interface states. When it comes to the operation of MOSFETs with Ⅲ-Ⅴ channel materials, because of the high interface states, the Fermi-level pinning phenomena lead to severe stretch-out of capacitance-voltage (C-V) and is one of the issues as well. The Fermi-level pinning comes especially from the native oxides and elemental Sb of GaSb upon exposure to oxygen. GaSb is also known to form the native oxides rapidly with air exposure, which makes it more difficult to reduce the native oxides.

In this study, GaSb metal oxide semiconductor (MOS) capacitors were fabricated with low temperature atomic layer deposition (ALD). Electrical properties were evaluated by C-V frequency dispersion and interface traps' density (D_{it}) from the Terman method. Interfacial analysis was performed to investigate the compositions, roughness, thickness, and density by Auger electron spectroscopy (AES), spectroscopic ellipsometer (SE), x-ray

reflectometry (XRR), atomic-force microscopy (AFM), x-ray photoelectron spectroscopy (XPS), and transmission electron microscopy (TEM).

Low temperature ALD was conducted to deposit Al_2O_3 on top of GaSb substrates as a gate oxide at various deposition process temperatures(100 ~ 310 ℃). It showed that the D_{it} level was lowered and the Fermi-level pinning behavior was alleviated in a C-V curve with low temperature ALD at 150 ℃. From the XPS results, the ratio of pure Ga_2O_3 over metastable Ga_2O increased as the deposition temperature decreased and was highest with low temperature ALD at 150 ℃. The C-V curve deteriorated with low temperature ALD at 100 ℃. It can be explained by the XRR results that demonstrate the significant decrease in density of the Al_2O_3 film with low temperature ALD at 100 ℃.

To reduce the D_{it}, a post deposition annealing process with N_2 ambient at various temperatures (150 ~ 300 ℃) for 30 seconds was adopted after depositing Al_2O_3. The stretch-out of the C-V curve was alleviated by post deposition rapid thermal process (RTP) at 250 ℃ but the C-V curve was more stretched out by the post-deposition RTP at 300 ℃. The roughness decreased as the RTP temperature increased, then increased when the RTP temperature was over 300 ℃. The ratio of pure Ga_2O_3 over metastable Ga_2O increased as the RTP temperature increased then decreased when the RTP temperature was over 300 ℃. The D_{it} is very consistent with the interfacial results. Forming gas annealing (FGA) is known as one of the effective ways to reduce the D_{it} in the

SiO_2/Si systems by filling up dangling bonds with hydrogen. To verify these hydrogen annealing effects, Al_2O_3/GaSb had been annealed with hydrogen including gases (5% H_2/95 % N_2 and 10 % H_2/90 % N_2). Results from both experiments with two different gases showed that the reduction of pure Ga_2O_3 to metastable Ga_2O occurred by hydrogen annealing. The ratio of Ga_2O_3 over Ga_2O decreased as the process temperature increased and the flux of hydrogen increased. The stretch-out in the C-V curves became worse and the D_{it} level significantly increased by hydrogen annealing due to the decreased ratio of pure Ga_2O_3 over metastable Ga_2O.

As mentioned before, GaSb forms the native oxide quickly with air exposure. Therefore, passivation is essential to be considered for fabricating the GaSb capacitors in ex-situ. Sulfuric passivation was chosen to be used, since the surface of GaSb can be passivated by forming Ga-S and Sb-S bonds, which would improve the electrical properties of the MOS capacitors. Each sample was immersed in the sulfuric solution (5 % $(NH_4)_2S$) for various times (1 ~ 15 minutes). The stretch-out of the C-V curve was successfully alleviated with immersion in the sulfuric solution for 5 minutes. However, immersion time longer than 5 minutes aggravated the C-V curves. The AFM results showed that the roughness increased as the immersion time increased. The inter layer (IL) between Al_2O_3 and GaSb also became longer with longer immersion duration.

Sb-oxide is not able to be perfectly cleaned by HCl even though HCl is known as the most effective wet chemical to get rid of the native oxides of GaSb. This remaining Sb-oxide oxidizes GaSb to Ga-oxide and changes itself to elemental Sb. For this, pre-deposition RTP (N_2 ambient), for improving electrical properties of the Al_2O_3/GaSb MOS capacitors, was adopted for the first time in this study. The improvement of stretch-out of the C-V curves was outstanding. The the D_{it} was also successfully reduced by the pre-deposition RTP at 550 and 575 ℃ and this the D_{it} value is the lowest one among the ones of sulfur treated GaSb MOS capacitors in literature(1.06×10^{12} $cm^{-2}ev^{-1}$ @ $E-E_v=0.004$). The Fermi-level pinning phenomenon deteriorated by pre-deposition RTP at 500 ℃ because chemical reactions for making the native oxides were accelerated at 500 ℃. The accelerated chemical reactions were proven by XPS, AFM, AES, and TEM analysis. The ratio of Ga_2O_3 over Ga_2O is also very consistent with electrical results.

In conclusion, low temperature ALD, post-deposition RTP, sulfuric passivation, and pre-deposition RTP are the effective ways to alleviate the Fermi-level pinning phenomenon that leads to the significant stretch-out in the C-V curves.

Keywords: GaSb, interface state, Fermi-level pinning, Ga oxide (Ga_2O_3), elemental Sb, atomic layer deposition, sulfuric passivation, pre-

deposition RTP

Student Number: 2014-30207

Seongkyung Kim

Table of Contents

Abstract i

Table of Contents vi

List of Tables x

List of Figures xi

List of Abbreviations xxiii

1. Introduction 24

1.1. Indispensability and Issues to Adopt III-V Channel Materials for MOSFETs 24

1.2. Objective and Chapter Overview 28

2. Literature Review 30

2.1. Native Oxide Formation of GaSb 30

2.1.1. Fast Oxidation of GaSb with Air Exposure 32

2.1.2. Effects of the Native Oxide on Electrical Properties 36

2.1.3. Thermal Desorption Behavior of the Native Oxide of GaSb 42

2.2. Surface Treatments and Passivation of GaSb 46

2.2.1. Chemical Wet Cleaning 46

2.2.2. Hydrogen Plasma 48

2.2.3. Sulfuric Passivation.....60

2.2.4. Insertion of Passivation Layers.....71

2.3. Oxide Deposition on GaSb by Atomic Layer Deposition 75

2.3.1. Deposition of Almina by Atomic Layer Deposition 75

2.3.2. Low Temperature Atomic Layer Deposition 78

2.4. Post-Deposition Thermal Annealing Process 80

2.4.1. Rapid Thermal Process.....80

2.4.2. Forming Gas Annealing 82

2.5. Electrical Characterization of III-V MOS Devices.....83

2.5.1. The Terman Method for the D_{it} Extraction.....83

3. Deposition of Alumina on GaSb by Low-Temperature Atomic Layer Deposition 86

3.1. Introduction 86

3.2. Experimental Procedures.....87

3.3. Results and Discussions 92

3.4. Summary.....99

4. Post-Deposition Rapid Thermal Process of Alumina Deposited GaSb 100

4.1. Introduction 100

4.2. Experimental Procedures.....101

4.3. Results and Discussions 107

4.3.1. Post-Deposition Rapid Thermal Process in a Nitrogen Ambience 107

4.3.2.Post-Deposition Annealing in a Gas Mixture Ambience (5 % H_2 and 95 % N_2) 115

4.3.3.Post-Deposition Annealing in a Gas Mixture Ambience (10 % H_2 and 90 % N_2) 119

4.4. Summary.....127

5. Sulfuric Passivation of GaSb 130

5.1. Introduction 130

5.2. Experimental Procedures.....131

5.3. Results and Discussions 134

5.4. Summary.....141

6. Pre-Deposition Rapid Thermal Annealing of GaSb in a Nitrogen Ambient 142

6.1. Introduction 142

6.2. Experimental Procedures.....144

6.3. Results and Discussions 147

6.4. Summary.....156

7. Conclusion 158

8. References 162

Abstract (in Korean) 174

List of Tables

Table 2.1 List of relevant native oxides of GaSb [96]..... 31

List of Figures

Figure 1.1 Technology innovations driven by scaling [1] 27

Figure 2.1 Ther typical XPS spectra from (a) GaSb, (b) GaAs and (c) GaP as a function of air exposure time. The exposure times are several seconds, 10 min, 25 h, 554 days from the bottom to the top in each series of spectra [47]. 33

Figure 2.2 Oxide thickness versus air exposure time for GaSb, GaAs and GaP [47]..... 34

Figure 2.3 The tapping mode AFM maps of the GaSb wafer: immediately taken out of a N_2 sealed pakage (left), exposed to air for a week (right). GaSb reacts with atmosphere rapidly to form thick native oxide on the surface [66]. 35

Figure 2.4 Terminology for charges associated with thermally grown SiO_2 [99]. 39

Figure 2.5 Effect of a fixed charge Q_f on a MIS capacitor with an n-type semiconductor (left) and the resulting parallel shifts of the C-V

curves relative to ideal ones for a p-type semiconductor (right) [99]. 40

Figure 2.6 Stretch out in the C-V curves due to interface-state charge Q_{it} [99]. 41

Figure 2.7 XPS spectra of the Ga $2p_{3/2}$, Sb 3d, C 1s core levels for a GaSb surface (a) chemically cleaned (solvent cleaning plus 50 % NH_4OH for 1 min); (b) after exposure to a 30 min ECR-H plasma at room temperature. [76] 52

Figure 2.8 I-V characteristics before and after exposure to direct H_2 plasma at 250 and 450 ℃ for 0.5 h.[108] 53

Figure 2.9 the C-V characteristics as a function of frequency of (a)n-type ALD and PEALD samples with HCl treatment and (b) p-type ALD and PEALD samples with HCl treatment. Measurement temperature is indicated in the figures. [58]..... 54

Figure 2.10 XPS data comparing the concentration of Sb_2O_3 in ALD and PEALD samples. Reduction in Sb_2O_3 in the (higher temperature) ALD samples in evident. [58] 55

Figure 2.11 Frequency-resolved the C-V measurements for GaSb MOS capacitors exposed to 10min, 150 ℃ plasma treatment with (a) 0W (no plasma treatment), (b) 25 W, (c) 50W, (d) 75W, and (e) 100W plasma power. (f) 2MHz the C-V curves from each sample in the power series showing variation in capacitance modulation. [64]56

Figure 2.12 (a) Sb 3d and (b) Ga 3d XPS scans from untreated (black) and 100W, 10 min, 150 ℃ hydrogen-plasma treated (red) samples. [64] 57

Figure 2.13 Sb 3d and Ga 3d core-level XPS spectra for (a) the untreated 500 nm thick GaSb epilayer with native oxide and after exposure to an H_2 plasma for 10 min with varying plasma powers of (b) 25 W, (c) 50 W, (d) 75 W, and (e) 100 W. Following plasma exposure, samples (b)–(e) were coated with TMA. [71] 58

Figure 2.14 (a) Sb3d and (b) Ga3d XPS spectra from the surface..... 59

Figure 2.15 Ga 2p3 and Sb 4d XPS spectra of n-GaSb after various surface treatments. (a) degreased surface (b) dipped in HCl for 5 min. and rinsed by 2-propanol, followed by 1-h Na_2S aqueous passivation

and DI water rinse (c) dipped in HCl for 5 min. and rinsed by 2-propanol, followed by 1-h Na_2S nonaqueous passivation (anthraquinone as oxidizing agent) and methanol rinse. [109]... 63

Figure 2.16 I–V curves of Au/n-GaSb Schottky contacts under forward and reverse biases. The diodes were fabricated on n-GaSb surfaces prepared by the processes (a) through (d). [110] 64

Figure 2.17 Forward and reverse bias I–V characteristics of Au/n-GaSb Schottky contacts, for samples (A–D). [79] 65

Figure 2.18 The process of sulfide passivation (a) breaking of bonds between Ga and Sb, (b) chemical reaction, (c) escape of an electron from the semiconductor into the solution, (d) formation of chemical bonds between sulfur and atoms of the semiconductor. [115].... 66

Figure 2.19 AFM images of the GaSb untreated, passivated by $(NH_4)_2S$ and Na_2S, respectively. [116] 67

Figure 2.20 (a) Typical measured parallel Gp/w versus frequency curves for different gate biases of MOSCAPs passivated with 20% neutralized $(NH_4)_2S$ solution III. (b) Interface trap density (D_{it})

distribution of MOSCAPs treated with four different solutions. [74] 68

Figure 2.21 Multi-frequency (1 kHz to 1 MHz) CV characteristics (~295 K) of Au/Ni/Al2O3/p-GaSb MOS capacitors with (a) no treatment (control) along with (b) 1%, (c) 5%, (d) 10%, and (e) 22% $(NH_4)_2S$ treatments. [75] 69

Figure 2.22 Cross-sectional TEM micrographs of (a) 1% and (b) 22% $(NH_4)_2S$ treated W/Al_2O_3/p-GaSb samples. [75] 70

Figure 2.23 C–V characteristics at different frequencies of (a) n-GaSb MOS capacitor with 10 nm ALD Al_2O_3 and HCl pretreatment with no oxide annealing, (b) with interface InAs layer showing improved frequency dispersion in accumulation, and (c) the D_{it} extracted from High–Low frequency method showing that the InAs passivation layer results in a significant reduction in the D_{it}. [81] 72

Figure 2.24 The D_{it}-($E-E_i$) characteristics of Al_2O_3/InAs/p-GaSb MOSCAPs with the InAs thickness of 0, 0.5, 1.0, 1.5, and 2.0 nm, respectively,

estimated by the Terman method using the 1MHz the C-V curves measured at 100 K. The black, orange, green, red, and blue colored curves are for the curves of the 0, 0.5, 1.0, 1.5, and 2.0 nm, respectively. The Al_2O_3 layers were deposited at 150 ℃. [78]... 73

Figure 2.25 Analytical fit to the Ga $2p_{3/2}$, Sb 3d, and Y 3p states. [91]..... 74

Figure 2.26 Schematic representation of ALD using self-limiting surface chemistry and an AB binary reaction sequence. (Reprinted with permission from ref 5. Copyright 1996 American Chemical Society.) [117] 77

Figure 2.27 Density of Al_2O_3 ALD films versus growth temperature from 33 to 177 °C for the various methods. [126]..... 79

Figure 2.28 Difference between (a) furnace annealing 900 ℃ 120 min and (b) rapid thermal annealing 1100 ℃ 64 seconds. [132] 81

Figure 2.29 Effect of bias voltage on surface-state occupancy. [158]..... 85

Figure 3.1 The schematic configuration of thermal ALD machine employed in this study. Color red indicates heating area. 89

Figure 3.2 The experimental process conditions for MOS capacitors fabrication. 91

Figure 3.3 Normalized capacitance-voltage curves of GaSb MOS capacitors at various deposition temperatures. 95

Figure 3.4 X-ray reflectometry (XRR) results of Al_2O_3 on Si wafers with various deposition temperatures. The right bottom graph shows the effects of deposition temperature on density of Al_2O_3 on Si wafers. 96

Figure 3.5 XPS spectra of Ga 3d for 2 nm thick Al_2O_3 on GaSb. The left bottom shows the effects of deposition temperature on the ratio of Ga_2O_3 over Ga_2O. 97

Figure 3.6 Energy distribution of the D_{it} of Al_2O_3/GaSb MOS capacitors. 98

Figure 4.1 The experimental process conditions for MOS capacitors fabrication. (to see the effects of post deposition RTP in a nitrogen ambience on Al_2O_3/GaSb.)..... 104

Figure 4.2 The experimental process conditions for MOS capacitors fabrication.

(to see the effects of 5 % H_2 thermal treatment on Al_2O_3/GaSb.)

..... 105

Figure 4.3 The experimental process conditions for MOS capacitors fabrication.

(to see the effects of 5 % H_2 thermal treatment on Al_2O_3/GaSb.)

..... 106

Figure 4.4 Normalized capacitance-voltage curves of GaSb MOS capacitors with the post-deposition RTP at various RTP temperatures in a nitrogen ambience. 109

Figure 4.5 The normalized capacitance-voltage curves at 1 MHz frequency.

..... 110

Figure 4.6 AFM analysis results of 10 nm thick Al_2O_3 on GaSb after the post-deposition RTP in a nitrogen ambience at various temperatures for 30 seconds. 111

Figure 4.7 XPS spectra of Ga 3d for 2 nm thick Al_2O_3 on GaSb. The right bottom shows the effects of RTP temperature in a nitrogen ambience on the ratio of Ga_2O_3 over Ga_2O. 112

Figure 4.8 XPS spectra of Sb 3d for 2 nm thick Al_2O_3 on GaSb. The right bottom

shows the effects of RTP temperature in a nitrogen ambience on the ratio of elemental Sb over Sb-oxide. 113

Figure 4.9 Energy distribution of the D_{it} of Al_2O_3/GaSb MOS capacitors. .. 114

Figure 4.10 Normalized capacitance-voltage curves of GaSb MOS capacitors with the hydrogen annealing at various temperatures in a gas mixture (5 % H_2/95 % N_2) ambience. 116

Figure 4.11 Energy distribution of the D_{it} of Al_2O_3/GaSb MOS capacitors. 117

Figure 4.12 XPS spectra of Ga 3d for 2 nm thick Al_2O_3 on GaSb. The right bottom shows the effects of the hydrogen annealing in a gas mixture (5 % H_2/95 % N_2) ambience on the ratio of Ga_2O_3 over Ga_2O..... 118

Figure 4.13 Normalized capacitance-voltage curves of GaSb MOS capacitors with the hydrogen annealing at various temperatures in a gas mixture(10 % H_2/90 % N_2) ambience. 121

Figure 4.14 Energy distribution of the D_{it} of Al_2O_3/GaSb MOS capacitors. 122

Figure 4.15 XPS spectra of Ga 3d for 2 nm thick Al_2O_3 on GaSb. The right bottom shows the effects of the hydrogen annealing in a gas

mixture (10 % H_2/90 % N_2) ambience on the ratio of Ga_2O_3 over Ga_2O..... 123

Figure 4.16 Comparison of the normalized capacitance-voltage curves of GaSb MOS capacitors under different hydrogen contents (left: 5 % H_2/95 % N_2, right: 10 % H_2/90 % N_2)..... 124

Figure 4.17 Comparison of the energy distribution of the D_{it} of GaSb MOS capacitors under different hydrogen contents..... 125

Figure 4.18 Comparison of the XPS spectra of Ga 3d for 2 nm thick Al_2O_3 on GaSb under different hydrogen contents (left: 5 % H_2/95 % N_2, right: 10 % H_2/90 % N_2)..... 126

Figure 5.1 The experimental process conditions for MOS capacitors fabrication. (to see the effects of sulfuric passivation on Al_2O_3/GaSb.)..... 133

Figure 5.2 Normalized capacitance-voltage curves of GaSb MOS capacitors with immersing the samples in $(NH_4)_2S$ solution for various times. 136

Figure 5.3 AFM analysis results of GaSb after immersing the samples in

$(NH_4)_2S$ solution for various times. 137

Figure 5.4 AES analysis results of 10 nm thick Al_2O_3 on GaSb after immersing the samples in $(NH_4)_2S$ solution for various times. 138

Figure 5.5 XPS spectra of Ga 3d for 2 nm thick Al_2O_3 on GaSb. The right bottom shows the effects of sulfuric passivation by immersing the samples in $(NH_4)_2S$ solution for various times on the ratio of Ga_2O_3 over Ga_2O. 139

Figure 5.6 Energy distribution of the D_{it} of Al_2O_3/GaSb MOS capacitors. .. 140

Figure 6.1 The schematic of surface reactions for the heating the GaSb wafers in a ultra high vacuum system ($<10^{-9}$ Torr). The informations are from these two papers [68, 100]. 143

Figure 6.2 The experimental process conditions for MOS capacitors fabrication. (to see the effects of pre-deposition RTP on GaSb.) 146

Figure 6.3 Normalized capacitance-voltage curves of GaSb MOS capacitors with the pre-deposition RTP at various RTP temperatures in a nitrogen ambience. 149

Figure 6.4 The C-V hysteresis of Al_2O_3 on GaSb substrates. (left: without pre-deposition RTP, right: with pre-deposition RTP at 575 ℃)..... 150

Figure 6.5 Energy distribution of the D_{it} of Al_2O_3/GaSb MOS capacitors. .. 151

Figure 6.6 XPS spectra of Ga 3d for 2 nm thick Al_2O_3 on GaSb. The right bottom shows the effects of the pre-deposition RTP temperature in a nitrogen ambience on the ratio of Ga_2O_3 over Ga2O. 152

Figure 6.7 AFM analysis results of 10 nm thick Al_2O_3 on GaSb after the pre-deposition RTP in a nitrogen ambience at various temperatures for 30 seconds. 153

Figure 6.8 AES analysis results of 10 nm thick Al_2O_3 on GaSb after the pre-deposition RTP in a nitrogen ambience at various temperatures for 30 seconds. 154

Figure 6.9 TEM images of 10 nm thick Al_2O_3 on GaSb after the pre-deposition RTP in a nitrogen ambience at various temperature for 30 seconds. 155

List of Abbreviations

ALD	Atomic Layer Deposition
MOS	Metal-Oxide-Semiconductor
MOSFET	Metal-Oxide-Semiconductor Field-Effect-Transistor
XRR	X-Ray Reflectivity
XPS	X-Ray Photoelectron Spectroscope
AFM	Atomic-Force Microscopy
AES	Auger Electron Spectroscopy
SE	Spectroscopic Ellipsometer
TEM	Transmission Electron Microscopy
C-V	Capacitance-Voltage
D_{it}	Density of Interface Traps
D_{itm}	Density of Interface Traps in Midgap
Q_{it}	Interface Traps Charge
Q_f	Fixed Oxide Charge
EOT	Effective Oxide Thickness
Vth	Threshold Voltage
N_f	Density of Fixed Oxide Charge
CMOS	Complementary Metal-Oxide-Semiconductor
RTP	Rapid Thermal Process
IL	Inter Layer
E_f	Fermi-Level
Q_{ot}	Oxide Trapped Charge
Q_m	Mobile Ionic Charges
SEM	Secondary Electron Microscope
TMA	Trimethylaluminium
PMA	Post-Metallization Anneal
IPA	Isopropyl Alcohol
FGA	Forming Gas Annealing
UHV	Ultra High Vacuum
C_{mg}	Midgap Capacitance

1. Introduction

1.1. Indispensability and Issues to Adopt III-V Channel Materials for MOSFETs

To achieve high performance and low power consumption of semiconductor devices, the requirement of shrinkage of the devices are continuing. For the past 50 years the semiconductor industry has marched at the pace of Moore's Law. Following this Moore's Law, transistor scaling is associated with that the number of transistors should be doubled every two years. Figure 1.1 shows the technology innovations driven by scaling [1]. The first generation of transistor scaling was geometrical scaling which was characterized in the 70s, 80s and 90s. The Equivalent Scaling started to be considered since mid-90s when major material and structural limitations were identified. The well known issues for it would be short channel effect, V_{th} mismatch for smaller transistors, and large gate leakage current for thinner gate oxides. Such as a strain technology and high-k/metal gate, there were lots of studies to replace the conventional SiON/Poli-Si [2-13].

Even with these equivalent scaling methods, new issues had to be solved by implementing new materials and structures in order to fabricate further scaled devices beyond 20 nm [14-16]. Ultimate effective oxide thickness (EOT)

scaling, multi-gate transistors, and high mobility channel devices were mainly discussed to achieve further scaling [15]. For ultimate EOT scaling, materials that have higher-k than HfO_2 were considered [17-18]. The multi-gate transistors were to increase the area of current path to make operation speed fast [19-24]. III-V compound materials and Ge have been studied as promising candidates for high mobility channel materials because of their extraordinary electrical properties especially their high carriers mobility [25-35]. GaAs and Ge have been researched for nMOSFETs and pMOSFETs respectively. In spite of being widely studied for pMOSFETs, Ge still has very critical issues to be adopted in the fabrication process of Si-based devices because of hygroscopicity and water solubility of its native oxide [36-39]. These can be problematic because most of the fabrication processes are related to water. Considering Ge's problems, GaSb has been attracted a great attention since GaSb has the native oxide which is chemically stable toward water and the outstanding electrical properties such as the highest hole mobility among III-V materials and high effective density of states [40-41].

For implementation of high-mobility complementary metal-oxide-semiconductor (CMOS) channel materials, III-V and Ge, there are some issues to be considered. Basic issues are same as the ones of Si devices for scaling Si CMOS. Other main issues are high-k dielectrics and interface state (D_{it}) control, CMOS solution with monolithic material integration, epitaxy of lattice-mismatched materials on Si substrate, and process complexity and

compatibility with significant thermal budge limitations [15]. Thermal instability of the native oxides of III-V and Ge has been mainly discussed as the most crucial issues [42-56].

Among these, interface state control should be the first thing to be pondered in the fabrication of metal-oxide-semiconductor (MOS) capacitors because of the Fermi-level pinning behavior. The Fermi-level pinning behavior is known from the bunched interface traps. The Fermi-level pinning behavior induces severe stretch-out of the C-V curve even with differentiating gate voltage [57-63]. The main causes for the interface states of GaSb are known as Ga-oxide, Sb-oxide, and elemental Sb [58, 64-65]. GaSb forms the native oxide rapidly and it is faster than GaAs and GaP do [47, 66]. There is plentiful research on cleaning the surface of GaSb, passivating the surface and inserting a layer [40, 58, 64-65, 67-92]. Even with these abundant studies, controlling the interface has been still problematic.

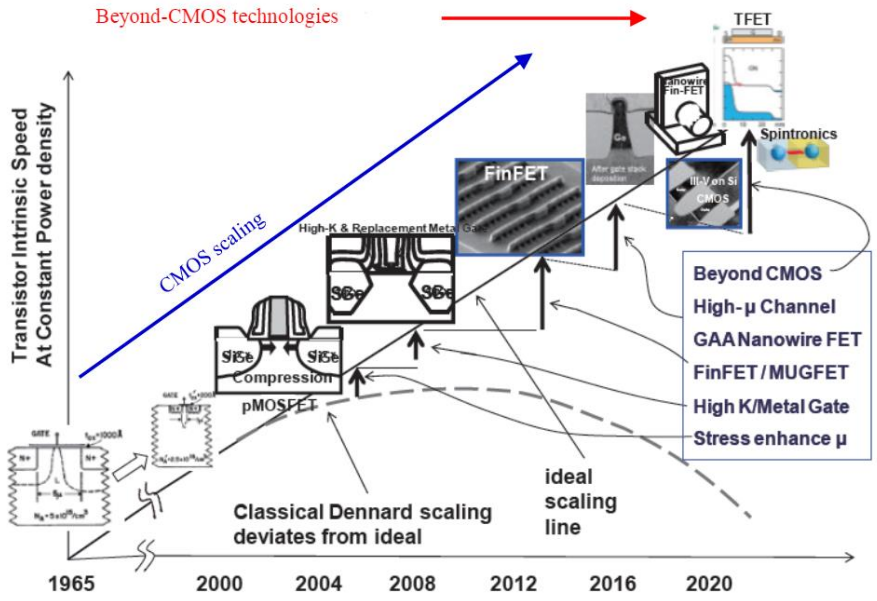

Figure 1.1 Technology innovations driven by scaling [1]

1.2. Objective and Chapter Overview

The objective of this dissertation is to successfully alleviate the stretch-out in the C-V curves for the GaSb MOS capacitors, which is from the Fermi-level pinning.

Chapter 2 presents the background studies of the native oxide formation of GaSb, its effects on electrical properties, various surface treatments, a deposition method, and electrical measurements.

Chapter 3 covers low temperature atomic layer deposition for depositing alumina on top of GaSb to alleviate the stretch-out of the C-V curve. The deposition temperatures were differentiated from 100 ~ 310 ℃. The stretch-out of the C-V curve was successfully reduced by lowering process temperature at 150 ℃ since the ratio of Ga_2O_3 over Ga_2O was increased. The deposition temperature lower than 100 ℃ was limited because of the low density of alumina.

Chapter 4 covers post-deposition rapid thermal process in a nitrogen ambience and hydrogen including gases' ambience on alumina deposited GaSb to reduce traps. The RTP temperatures varied from 150 ~ 300 ℃. The Dit value was reduced by the post-deposition rapid thermal process with a nitrogen ambience at 250 ℃ since the ratio of Ga_2O_3 over Ga_2O was increased. The

post-deposition annealing with hydrogen including gases exacerbated the C-V curves. It was resaulted from the reduction of pure Ga_2O_3 to meta-stable Ga_2O.

Chapter 5 covers sulfuric passivation of GaSb surfaces. Due to the fast oxidation of GaSb with air exposure, it is essential to adopt surface passivation. GaSb was immersed in sulfuric solution for various times (1 ~ 15 minutes). The stretch-out of the C-V curve was successfully alleviated with immersion in sulfuric solution for 5 minutes. The AFM results showed that the surface roughness increases with immersion in sulfuric solution for 10 and 15 minutes and these aggravated the C-V curve.

Chapter 6 covers implementing pre-deposition rapid thermal process on GaSb to improve its electrical properties for the first time by this author. The RTP temperature were from 500 ~ 575 ℃. The stretch-out of the C-V curve was successfully alleviated by pre-deposition RTP at 575 ℃ since the ratio of Ga_2O_3 over Ga_2O was increased.

Finally, in chapter 7, the conclusion of the dissertation is made.

2. Literature Review

2.1. Native Oxide Formation of GaSb

GaSb forms native oxides which are well known as Ga_2O_3, Ga2O, Sb_2O_5, Sb_2O_4, and elemental Sb [42, 58, 68, 71, 93-95]. Gibbs free energies of the native oxides of GaSb are shown in Table 2.1 [96]. Well known reactions of the native oxide formations and possible reactions are as below [97-98].

$$2GaSb + 3O_2 \rightarrow Ga_2O_3 + Sb_2O_3 \ (\Delta G^o = -311.2 kcal/mol)$$

$$2GaSb + Sb_2O_3 \rightarrow Ga_2O_3 + 4Sb \ (\Delta G^o = -12 kcal/mol)$$

$$2GaSb + Sb_2O_3 \rightarrow Ga_2O_3 + 4Sb \ (\Delta G^o = -68.5 \ kcal/mol)$$

$$8GaSb + 3Sb_2O_4 \rightarrow 4Ga_2O_3 + 14Sb \ (\Delta G^o = -309.4 \ kcal/mol)$$

$$5Sb_2O_3 + 2GaSb \rightarrow 3Sb_2O_4 + Ga_2O_3 + 6Sb \ (\Delta G^o = -33.1 \ kcal/mol)$$

$$6Sb_2O_3 + 2GaSb \rightarrow 3Sb_2O_5 + Ga_2O_3 + 8Sb \ (\Delta G^o = +94.4 \ kcal/mol)$$

Table 2.1 List of relevant native oxides of GaSb [96].

Oxide	**Gibbs free energy of formation [kJ/mol]**
Sb_2O_3	-634.344
Sb_2O_4	-795.8
Sb_2O_5	-829.144
Ga_2O	-128.425
Ga_2O_3	-998.339

2.1.1. Fast Oxidation of GaSb with Air Exposure

Mizokawa[47] showed XPS results about the oxidation of GaSb, GaAs, and GaP with long time air exposure as a function of time (figure2.1). Mizokawa eliminated the native oxides of GaSb, GaAs, and GaP with hydrochloric acid and then checked the variation of XPS spectra with air exposure for years. Even within several seconds of air exposure, GaSb formed the native oxides (about 5 Å). The oxide thickness in 3 years was estimated to be about 40 Å for GaSb and 20 Å for GaAs and GaP. Mizokawa also plotted oxide thickness of GaSb, GaAs, and GaP versus air exposure time (figure 2.2.). From these results, it is clear that GaSb forms the native oxide faster than GaAs and GaP do. Nainani's study[66] also demonstrated the fast oxidation of GaSb with air exposure. Nainani measured roughness of two GaSb substrates; one was immediately taken out of a N_2 sealed package and another was exposed to air for a week. The roughness increased from 0.73 nm to 4.01 nm with air exposure for a week (figure 2.3).

From the Mizokawa and Nainani's studies, it was turned out that GaSb forms the native oxide quickly and even faster than other III-V materials do. It would not be a matter for in-situ processes but should be critical for ex-situ processes because of the native oxide formation by air exposure. GaSb requires extra passivation procedures for ex-situ.

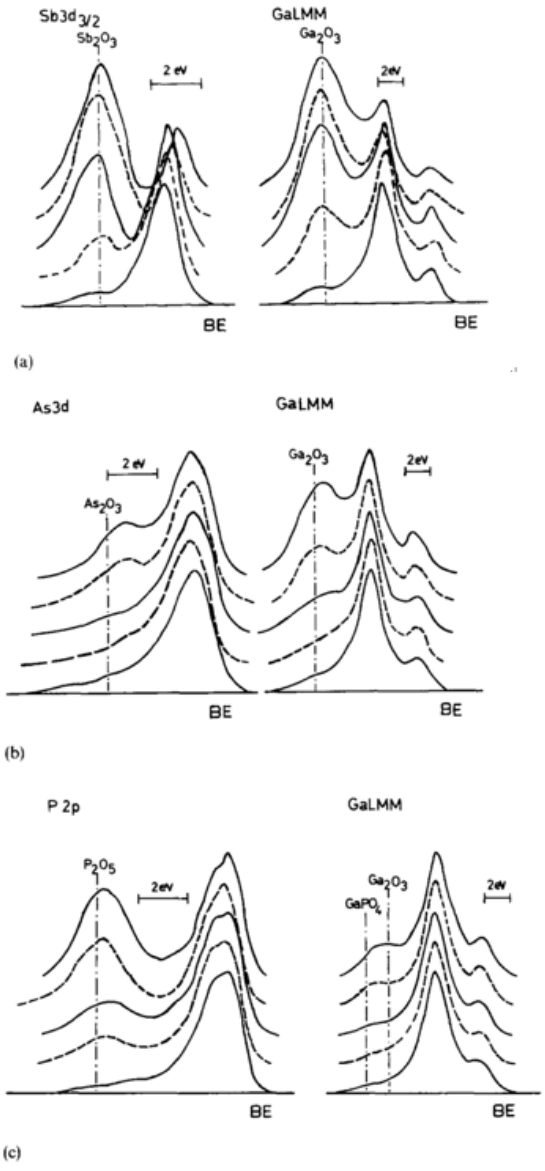

Figure 2.1 Ther typical XPS spectra from (a) GaSb, (b) GaAs and (c) GaP as a function of air exposure time. The exposure times are several seconds, 10 min, 25 h, 554 days from the bottom to the top in each series of spectra [47].

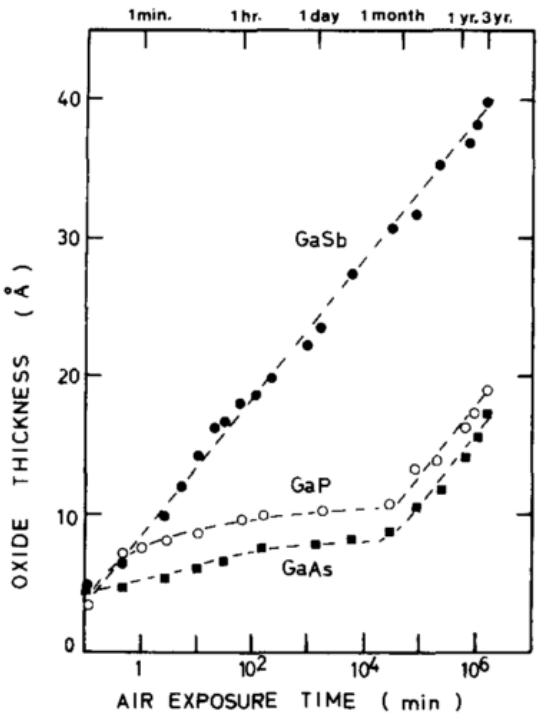

Figure 2.2 Oxide thickness versus air exposure time for GaSb, GaAs and GaP [47].

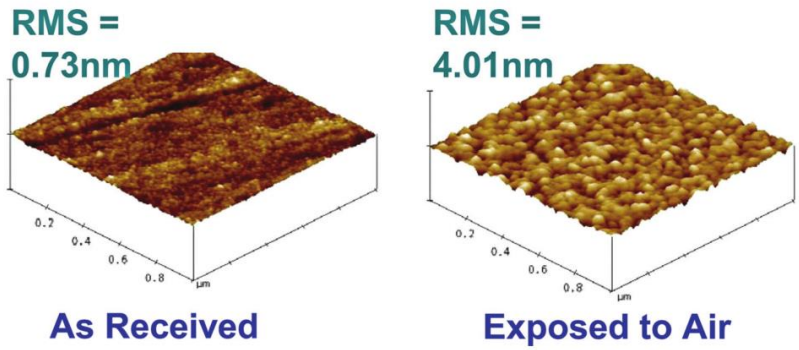

Figure 2.3 The tapping mode AFM maps of the GaSb wafer: immediately taken out of a N_2 sealed pakage (left), exposed to air for a week (right). GaSb reacts with atmosphere rapidly to form thick native oxide on the surface [66].

2.1.2. Effects of the Native Oxide on Electrical Properties

To grab a fast incite on charges, Hori introduced charges and electrical properties of Si-SiO_2 MOS [99]. Most of the explanations that are displayed in this section about traps are from Hori's book [99].

There are 4 different types of charges related to thermally grown SiO_2. Terminology for charges associated with thermally grown SiO_2 is shown in figure 2.4 [99]. The charges are classified with respect to their location and actions as follows.

(1) Interface-state charges (Q_{it}) are located so close to the Si-SiO_2 interface. Q_{it} has energy states so close to the Fermi-energy level (E_f) variation range of the semiconductor. It means that Q_{it} exists within the silicon forbidden bandgap as to be able to exchange charges with the semiconductor in a short time. [99]

(2) Fixed charges (Q_f) are located at or very near the interface. Unlike Q_{it}, Q_f cannot exchange charges. [99]

(3) Dielectric-trapped charges or oxide trapped charges (Q_{ot}) are distributed inside the bulk dielectric and capture (or emit) the charges brought into the dielectric film by hot-carrier injection, and so on. [99]

(4) Mobile ionic charges (Q_m) are mobile within the oxide under bias-temperature aging conditions. Q_m is treated less important in the recent technology. [99]

Figure 2.5 shows the effects of Q_f for n-type silicon. Since there are some fields that are lined from Q_f to the charges in the gate, the fields lined from the ionized donors to the charges in the gate are fewer than the fields when $Q_f = 0$ according to the charge neutrality requirement. Because fewer donors are ionized, the depletion-layer width w in the semiconductor will be narrower than that with $Q_f = 0$ at any given V_G. As a consequence, Q_f causes the parallel shift ΔV along the V axis in a the C-V curve. ΔV is expressed as follow.

$$\Delta V = - Q_f / C_i = - Q_f d / \varepsilon_i$$

Since Q_f is usually positive in the Si-SiO_2 system, ΔV is negative. If $Q_f < 0$, ΔV will be positive. Taking into account of the work-function difference and the effects from Q_f, the C-V curves will be like the right figure in figure 2.6.

Interface states change their charge state depending on whether they are filled or empty, and are categorized as two charge types. The interface states above the midgap (E_i) are acceptor-like interface states while those below E_i are donor-like interface states. Acceptor-like interface states are negative when filled with electrons and neutral when empty. Donor-like traps are neutral when filled and positive when empty. It happens when it crosses E_f.

Figure 2.6 shows the stretch out in the C-V curves due to interface-state charge Q_{it}. Q_{it} will not simply shift the C-V curves in parallel but stretch them out because the interface-state occupancy varies with V_g. Since acceptor- and donor-like interface states are only in the upper and lower halves of the bandgap, respectively, as mentioned above, interface states, if any, are considered not to be charged when the surface potential Φ_s is zero. Therefore, no shift due to Q_{it} is observed in a high-frequency the C-V curve when C is equal to the midgap capacitance C_{mg} defined for $\psi_s=\Phi_s$. When V_g is swept into the negative direction under steady-state condition so that $\Phi_s<0$, donor-like interface states above E_f are charged positive, resulting in a negative the C-V shift ΔV given by

$$\Delta V = -\frac{q}{C_i}\int_{\Phi_s}^{0} D_{it}(\Phi)d\Phi \quad \text{for } \Phi s < 0.$$

Similarly, when V_g is positive so that $\Phi_s>0$, acceptor-like interface states below E_f are charged negative, resulting in a positive the C-V shift ΔV according to

$$\Delta V = \frac{q}{C_i}\int_{0}^{\Phi_s} D_{it}(\Phi)d\Phi \quad \text{for } \Phi s > 0.$$

In addition to the stretch-out along the V axis, the low-frequency the C-V curve is distorted by the capacitance increase ΔC according to the total capacitance which is expressed by

$$1/C = 1/C_i + 1/(C_s + C_{it}).$$

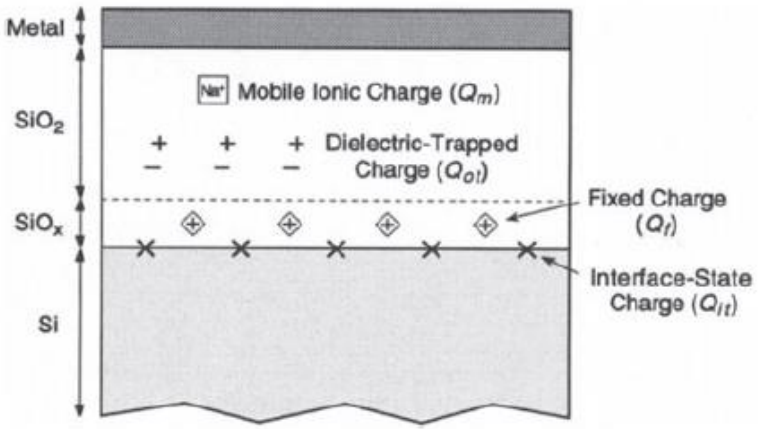

Figure 2.4 Terminology for charges associated with thermally grown SiO_2 [99].

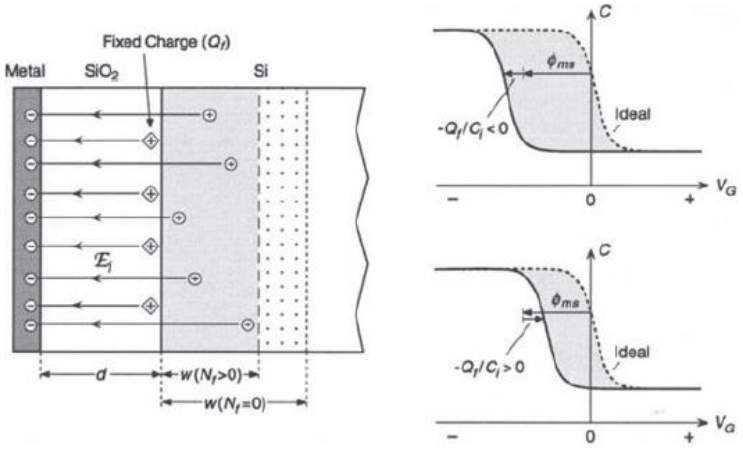

Figure 2.5 Effect of a fixed charge Q_f on a MIS capacitor with an n-type semiconductor (left) and the resulting parallel shifts of the C-V curves relative to ideal ones for a p-type semiconductor (right) [99].

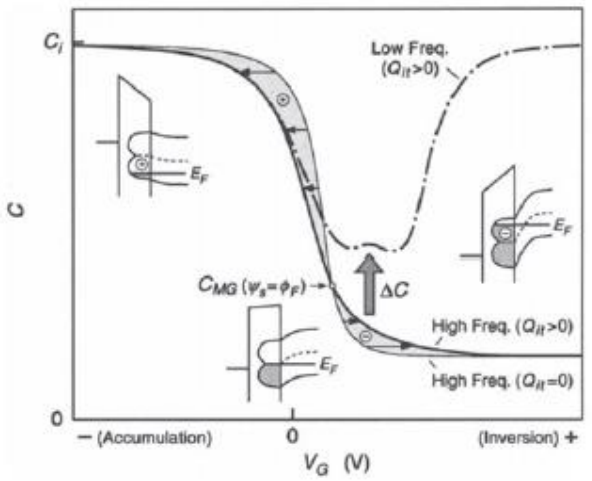

Figure 2.6 Stretch out in the C-V curves due to interface-state charge Q_{it} [99].

2.1.3. Thermal Desorption Behavior of the Native Oxide of GaSb

L. J. Gomez Zazo [100] had conducted various chemical cleaning methods on GaSb and then observed the changes in Auger spectra and RHEED diffraction patterns with heating the samples at various temperatures with an Sb flux. From the Auger spectra, L. J. Gomez Zazo explained how the peaks' intensities varied from the surface changes depending on the heating temperatures. The six temperature regions were differentiated as follow [100]

(1) Room temperature ~ 80 ℃ : The Sb oxide peak decreases and the pure Sb peak grows. It indicates that a certain amount of the oxide is reduced. It can be from temperature effect but more probably from the electron bombardment during the initial stages of the Auger spectra recording [100].

(2) 80 ~ 160 ℃ : There is no noticeable change [100].

(3) above 160 ℃ : The pure Sb peak starts to decrease reaching a minimum value, clearly distinguished from the noise level, at around 250 ℃. This pure Sb decrease is accompanied by a quick growing of the Ga peak [100].

(4) 200 ~ 400 ℃: A gradual and complete elimination of the Sb oxide takes place. In this temperature range, the Ga peak continues to grow, although more slowly than in the above region. Since the oxide elimination takes place over a

wide temperature range, an explanation via a desorption process does not seem suitable. Near the GaSb interface a Sb_2O_3 reduction giving rise to Ga_2O_3 and metallic Sb could take place via the reaction $Sb_2O_3 + 2GaSb \rightarrow Ga_2O_3+4Sb$. Later, the pure Sb out diffuses reaching the surface. The pure Sb evaporates from the surface in such a way that once a certain rate is achieved, the surface becomes depleted of pure Sb and the overall process can continue [100].

(5) 400 ~ around 460 ℃: The surface layer consists almost exclusively of Ga oxide. The small Sb signal observed may be due to a small amount of pure Sb dissolved in the Ga oxide. However, it seems more probable that this signal comes from the GaSb substrate, because at these temperatures the vapor pressure of Sb in high enough to completely deplete pure Sb from the surface layer [100].

(6) 480 ~ 510 ℃: The Ga oxide desorbs quickly leaving a clean GaSb surface [100].

From the results, it can be deduced as that the elemental Sb decreases with thermal annealing over 300 ℃.

Z. Y. Liu [68] showed XPS evolution with annealing GaSb in a vacuum chamber at various temperatures. Z. Y. Liu also described the changes in the XPS spectra depending on the heating temperatures and the explanation is as below [68].

(1) ~ 100 ℃: The intensity of the antimony oxide-related peak begins to

decrease, accompanied by an increase in the intensity of the gallium oxide-based peak. At the same time, the elemental antimony concentration continues to increase, although at a slower rate than that of peak intensities of Ga and Sb oxides until a maximum value is reached at around 350 ℃. When using AlK_{α} radiation in the XPS measurements, the Ga $2p_{3/2}$ spectra are more surface sensitive than Sb 4d spectra. Therefore, if the bulk GaSb peak intensity is used as a reference, the rate of change for Ga-oxide on the surface is larger than that for Sb oxides or elemental Sb. The trends of these changes are consistent with reaction ($2GaSb + Sb_2O_3 \rightarrow Ga_2O_3+4Sb$), which suggests that Sb_2O_3 reacts with GaSb near the oxide-GaSb interface to yield Ga_2O_3 and elemental Sb. Thermal annealing provides the necessary energy to overcome reaction and diffusional barriers and reaction occurs rapidly at a temperature of ~ 100 [68].

(2) Above 350 ℃: The Sb-oxide peak intensity continues to decrease at a high rate, while Ga oxide intensity remains almost unchanged over the temperature range of 350-450 ℃, and the intensity of elemental Sb begins to decrease slightly. This result implies that the reaction ($2GaSb + Sb_2O_3 \rightarrow Ga_2O_3+4Sb$) may not be a dominant factor in the reduction of the remaining Sb oxide over that temperature range. A temperature of 350 ℃ leads to the thermal desorption of Sb oxide from the surface. Elemental Sb diffuses out from the oxide-GaSb interface and also desorbs from the surface [68].

(3) ~ 500 ℃: Ga oxides quickly desorb from the surface evidenced by the rapid reduction of its peak intensity [68].

(4) 550 ℃: The peak intensity associated with metallic gallium begins to increase rapidly. Since this thermal treatment was done in a vacuum chamber without an antimony flux, high-temperature thermal annealing results in the decomposition of GaSb substrates and Sb loss [68].

(5) 600 ℃: After being kept at 600 ℃ for half an hour, Ga oxides disappear completely, leaving an oxide-free surface [68].

From these results, it can be again deduced as that the elemental Sb decreases with thermal annealing over 350 ℃.

2.2. Surface Treatments and Passivation of GaSb

2.2.1. Chemical Wet Cleaning

One of the most common methods to get rid of the native oxides is immersing the samples in acidic chemicals for a while. Because of this, the first thing that should be considered is comparing the effects of acidic chemicals. In the case of the GaSb based devices, there have been various attempts to find the best acidic chemical for eliminating the native oxides of GaSb [66, 68, 87, 94, 98, 100-106]. L.J. Gomez [100] had used H_2SO_3:H_2O_2:H_2O, HCl:H_2O_2:NaK(tartrate), HF:HNO_3:CH_3COOH, and Br:methanol as etchants at various temperatures and time and then annealed the GaSb samples to see how the native oxides change. Eric K [101] had investigated photoelectrochemical behavior of GaSb in aqueous NaOH, NaCl, and HCl solutions. E. Papis [102] had employed variable angle spectroscopic ellipsometry to study (100) GaSb surface under various chemical treatments providing information on the thickness, refractive index and dielectric function of residual oxides. HCl-based solutions, HF-based solutions, NH_4OH- based solutions, and sulfuric solutions such as Na_2S and $(NH_4)_2S$ at various concentrations and temperatures for different time were used in the E. Papis' study. E. Papis [103] mentioned in a different journal that HCl-base solutions seem to be more favorable than the HF-based ones because of the low surface

roughness and summarized GaSb surface preparation for deposition of metal and dielectric films. E. Hwang[104] also showed that the native oxides from GaSb surface were effectively removed by HCl but leaved slightly antimony rich. However E. Hwang [104] mentioned that integrate pre-deposition surface treatments of GaSb with subsequent atomic layer deposition of high-k dielectric would be needed. Aneesh Nainani [66] had studied the surface cleaning of the Sb-based compound semiconductors using HF, NH_4OH, and HCl and the metal-oxide-semiconductor capacitors fabricated subsequently. This group [66] had concluded that 9 % HCl cleaning for 2-3 minutes showed the best cleaning effects on the native oxides of GaSb compared to the effects by HF and NH_4OH.

2.2.2. Hydrogen Plasma

As recommended by E. Hwang[104], integrate pre-deposition surface treatments of GaSb with subsequent atomic layer deposition of high-k dielectric are needed. For this, many have researched on in-situ cleaning methods such as hydrogen plasma cleaning [58, 64, 71, 76, 98, 107]. Z. Lu [76] described the use of a low-temperature technique, which is based on H atoms from a microwave electron cyclotron resonance (ECR) H_2 plasma, to remove surface oxides and carbon from a single-crystal GaSb surface. Their experiments indicated that oxide removal occurs at a temperature of ~ 250 ℃, much lower than that for thermal evaporation of the oxide. They showed XPS spectra of the Ga $2p_{3/2}$, Sb 3d, C 1s core levels for a GaSb surface. From the XPS results, Sb-oxide and carbon traces disappeared completely after the ECR hydrogen treatment, whereas the Ga-oxide trace is reduced (figure 2.7). They explained the removal of the Sb oxide and free carbon attributed to the ready formation of volatile species from atomic hydrogen, such as H_2O and hydrocarbon, in the vacuum chamber. Dutta [98] had summarized the effects of hydrogen plasma passivation. Dutta mentioned Polyakov's study [108]. Polyakov [108] had used atomic hydrogen and atomic nitrogen flows in a microwave plasma crossed beams machine and in direct H_2 and N_2 plasma on the GaSb/InGaAsSb diodes. The increased leakage current in I-V curve showed the degradation in the devices by the direct H_2 plasma (figure 2.8). A. Ali [58] suggested to use plasma

enhanced atomic layer deposition (PEALD) for the Fermi level unpinning of GaSb (100). Figure 2.9 shows the improvement of the C-V characteristics. This group insisted that the reduction in Sb_2O_3 to metallic Sb was suppressed for the PEALD samples due to a low process temperature (figure 2.10), which was identified by x-ray photoelectron spectroscopy analysis. They also insisted that the absence of elemental Sb ended up with unpinning of the Fermi level at PEALD Al_2O_3/GaSb interface. They explained the absence of the Sb oxide was a clue of the existence of elemental Sb because the Sb oxides change to the elemental Sb while depositing thinfilms. Laura B. Ruppalt [64] studied the effectiveness of hydrogen plasma surface treatments for improving the electrical properties of the GaSb/Al_2O_3 interface. Here is what they had conducted, prior to atomic layer deposition of an Al_2O_3 dielectric, p-GaSb surfaces were exposed to hydrogen plasma in situ, with varing plasma powers, exposure times, and substrate temperatures. The various C-V curves depending on the plasma power are in figure 2.11. This group explained that hydrogen species decompose Sb-oxide present in the native film, resulting in the formation of elemental Sb and Ga-oxides and the elemental Sb is then removed by thermal desorption or by formation of volatile SbH_3 (figure 2.12). Erin R. [71] showed the influence of an in situ hydrogen plasma pre-treatment on the modification of native oxides of GaSb surfaces prior to atomic layer deposition is presented. This group varied rf-plasma power, exposure time, and substrate temperature and checked the electrical and chemical properties of the samples

by atomic force microscopy (AFM), ex situ X-ray photoelectron spectroscopy (XPS), as well as capacitance-voltage (C-V) measurements. Since the most effective hydrogen plasma treatments resulted in the absence of Sb-oxides, a reduction in elemental Sb, and an increase in the Ga_2O_3 content at the interface in their study, they thought that obtaining a completely oxide free surface may not be necessary to produce a good electrical interface with a subsequent ALD Al_2O_3 dielectric. They could effectively get rid of Sb-oxide and showed the increased amount of Ga_2O_3 (figure 2.13). The reduction of Sb-oxide charged from the ready formation of volatile species following the reaction [71]:

$$Sb_2O_5 + 10H^0 \rightarrow Sb_2O_3 + 2H_2O\uparrow + 3H_2 \rightarrow 2Sb\uparrow + 3H_2O$$

They also said that the Ga_2O_3 rich layer is created by the reoxidation of the Ga_2O due to surplus oxygen in the system arising from the production of H_2O in the above equation, desorption of water from the reactor walls, as well as migrating O_2 from the decomposition of Sb-oxides [71]:

$$2Sb_2O_5 \rightarrow 2Sb_2O_3 + 2O_2 \rightarrow 4Sb + 5O_2$$

$$4GaSb + 3O_2 \rightarrow 2Ga_2O_3 + 4Sb$$

The Ga_2O is unstable in bulk and can undergo the following disproportionation reaction [71]:

$$2Ga_2O \rightarrow 4Ga + Ga_2O_3$$

They also mentioned that the Sb-oxides react with GaSb substrates and form Ga_2O_3 as follows [71]:

$$2GaSb + Sb_2O_3 \rightarrow Ga_2O_3 + 4Sb$$

Laura B. Ruppalt [107] finally figured out the formation of pure Ga_2O_3 is the key for lowering the D_{it} level for the GaSb based devices. The authors [107] investigated the use of H_2/Ar-plasma exposure to fabricate Al_2O_3/GaSb MOS capacitors. Figure 2.14 shows the XPS spectra.

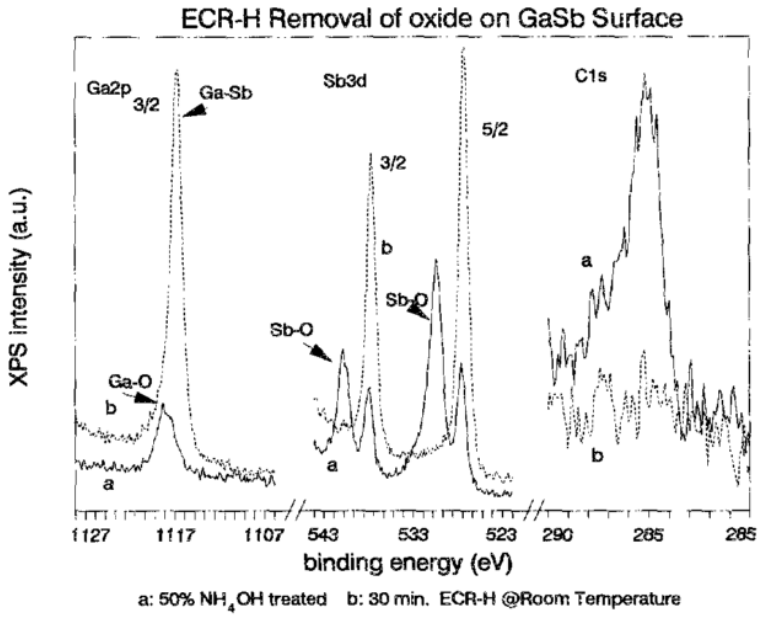

Figure 2.7 XPS spectra of the Ga $2p_{3/2}$, Sb 3d, C 1s core levels for a GaSb surface (a) chemically cleaned (solvent cleaning plus 50 % NH_4OH for 1 min); (b) after exposure to a 30 min ECR-H plasma at room temperature. [76]

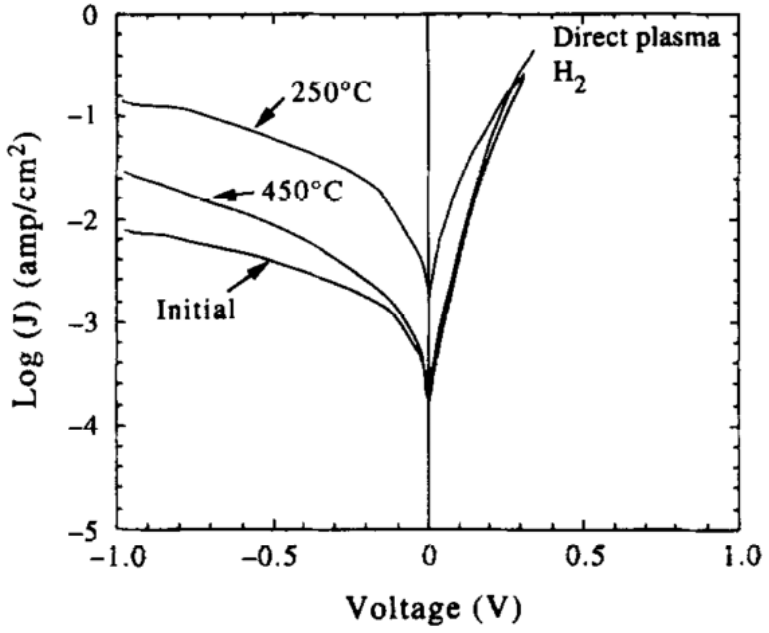

Figure 2.8 I-V characteristics before and after exposure to direct H_2 plasma at 250 and 450 ℃ for 0.5 h.[108]

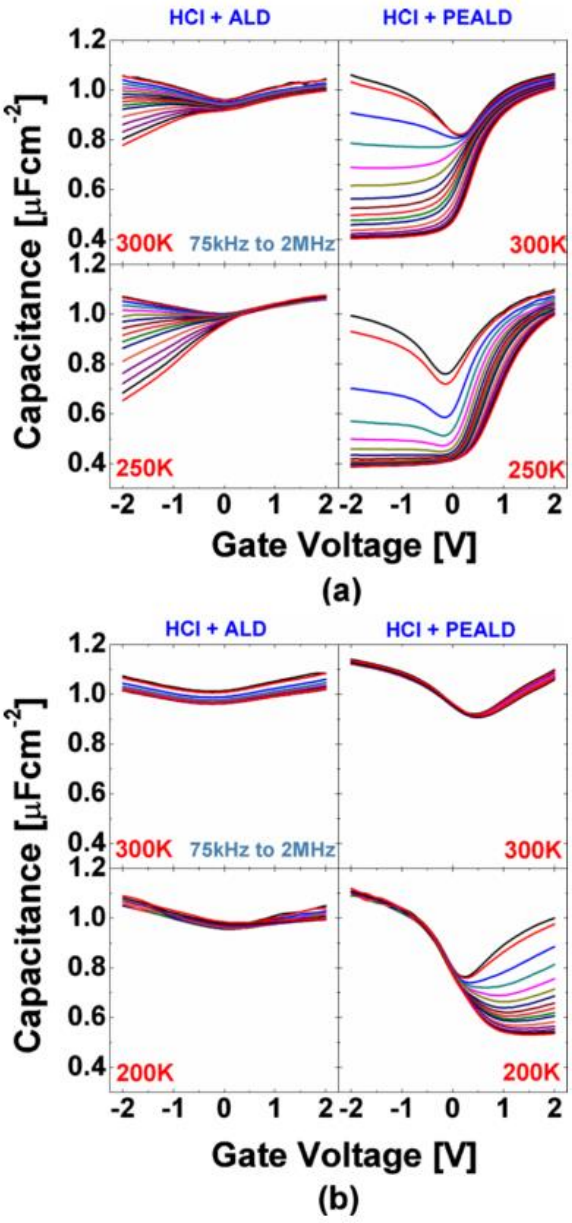

Figure 2.9 the C-V characteristics as a function of frequency of (a)n-type ALD and PEALD samples with HCl treatment and (b) p-type ALD and PEALD samples with HCl treatment. Measurement temperature is indicated in the figures. [58]

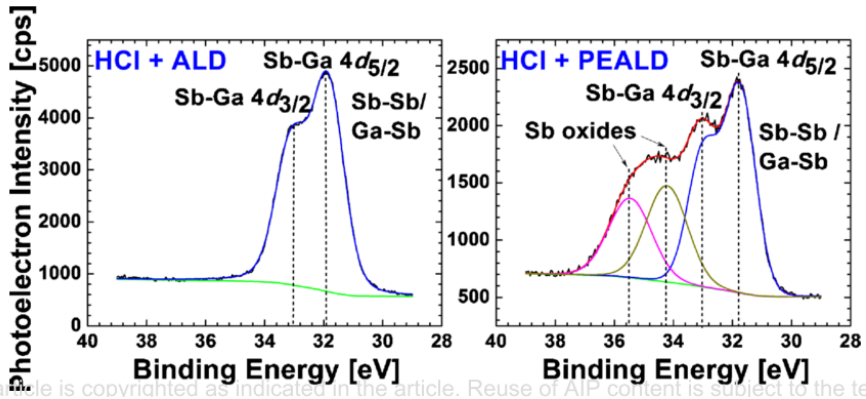

Figure 2.10 XPS data comparing the concentration of Sb_2O_3 in ALD and PEALD samples. Reduction in Sb_2O_3 in the (higher temperature) ALD samples in evident. [58]

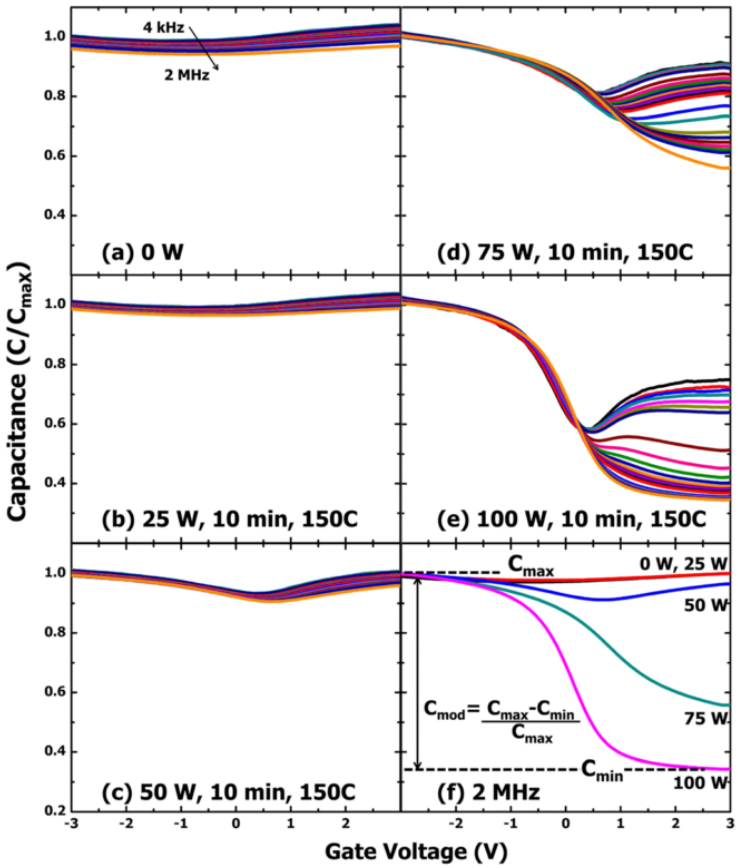

Figure 2.11 Frequency-resolved the C-V measurements for GaSb MOS capacitors exposed to 10min, 150 ℃ plasma treatment with (a) 0W (no plasma treatment), (b) 25 W, (c) 50W, (d) 75W, and (e) 100W plasma power. (f) 2MHz the C-V curves from each sample in the power series showing variation in capacitance modulation. [64]

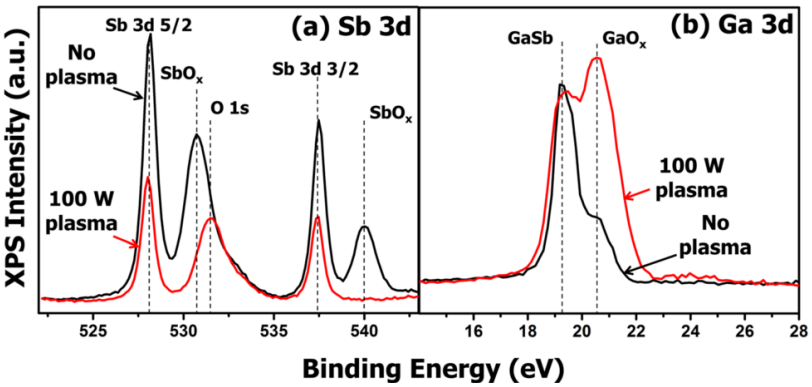

Figure 2.12 (a) Sb 3d and (b) Ga 3d XPS scans from untreated (black) and 100W, 10 min, 150 ℃ hydrogen-plasma treated (red) samples. [64]

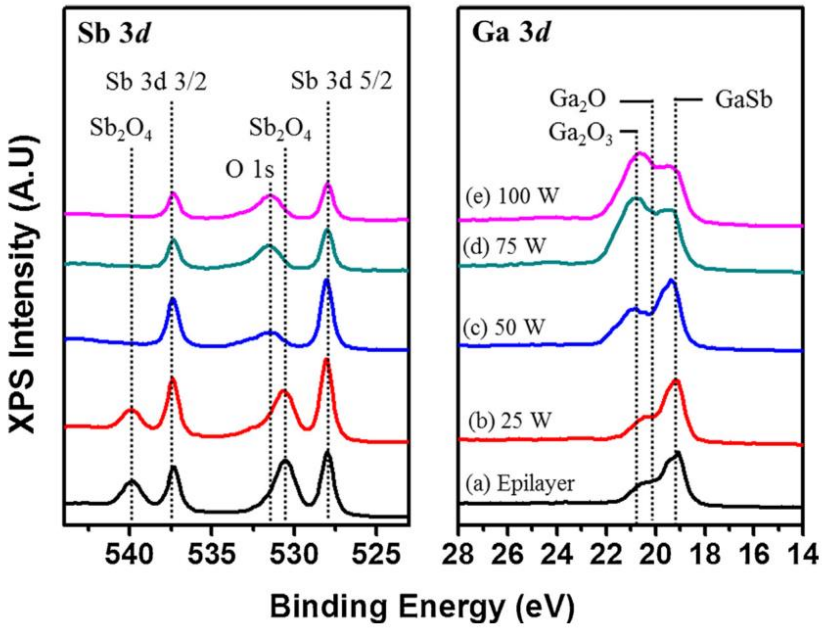

Figure 2.13 Sb 3d and Ga 3d core-level XPS spectra for (a) the untreated 500 nm thick GaSb epilayer with native oxide and after exposure to an H_2 plasma for 10 min with varying plasma powers of (b) 25 W, (c) 50 W, (d) 75 W, and (e) 100 W. Following plasma exposure, samples (b)–(e) were coated with TMA. [71]

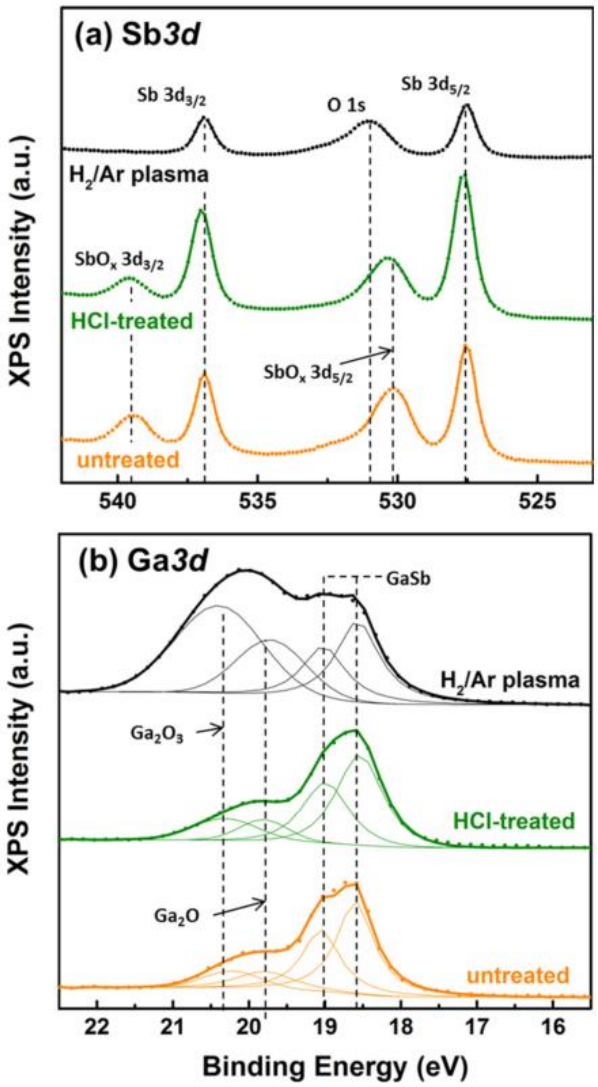

Figure 2.14 (a) Sb3d and (b) Ga3d XPS spectra from the surface of an untreated (orange), HCl-treated (green), and H2/Ar-plasma treated (black) GaSb sample, as indicated. Curve fits are shown in (b) to indicate the contribution of various Ga-oxide components. [107]

2.2.3. Sulfuric Passivation

Since GaSb forms the native oxides promptly with air exposure, it is essential to adopt extra passivation processes after cleaning the native oxides for ex-situ oxide deposition. Sulfuric passivation has excessively studied by many researchers[65, 74-75, 79-80, 82-83, 85, 88-89, 92, 95, 98, 102-103, 109-116].

Chuing L. Lin [95] insisted that sulfuric treatment on GaSb was an effective method for preventing the formation of the leakage path due to the transformation of Sb (Sb-oxides to Sb_2S_5) by a $(NH_4)_2S$ treatment. The mechanism that prevented the formation of the leakage path at the as-etched GaSb surface was elucidated by X-ray photoelectron spectroscopy. Z. Y. Liu [109] reported a nonaqueous passivation regime consisting of Na_2S/benzene/15-crown-5/oxidant. The optical and chemical properties of GaSb surfaces were investigated after aqueous and nonaqueous sulfide treatments. The XPS spectra were demonstrated in figure 2.15. In his next study [110], Z. Y. Liu showed the improved I-V curves of Au/n-GaSb Schottky contacts (figure 2.16). S. McDonnell [111] offered the evolution of the interfacial chemistry of GaSb(001), which was treated with $(NH_4)_2S$ in situ, with monochromatic X-ray photoelectron spectroscopy, following heat treatment and exposure to trimethylaluminum (TMA) and deionized water in an atomic layer deposition reactor. D.M. Murape [79] showed improved GaSb

surfaces using a $(NH_4)_2S/(NH_4)_2SO_4$ solution. The Sb-oxides were effectively removed on treating with ($[(NH_4)_2S/(NH_4)_2SO_4]^+S$) and $(NH_4)_2S$. Figure 2.17 shows the I-V characteristics of Au Shottky barrier diodes (SBDs) fabricated on the GaSb as-received, with $(NH_4)_2S$ and ($[(NH4)2S/(NH4)2SO4]^+S$). Compared to other samples, the sample A, which is the reference material, showed a larger reverse leakage current. Bo Wang [115] reported a systematic study on modulating optical properties in GaSb with the sulfur passivation. They used $(NH_4)_2S$ solution for various times. Figure 2.18 demonstrates the process of sulfide passivation. They also explained chemical reactions associated with the passivation process were [115]:

$$2GaSb + 3O_2 \rightarrow Ga_2O_3 + Sb_2O_3$$

$$2GaSb + Sb_2O_3 \rightarrow Ga_2O_3 + 4Sb$$

$$A^{III}B^{V} + HS^- + H_2O \rightarrow (A^{III})_{x'}S_{y'} + (B^{V})_{x''}S_{y''} + OH^- + H_2 \uparrow$$

where reactant compounds are A and B and the value of x and y is in the range from 1 to 5.

Bo Wang [116] compared the sulfur solutions, $(NH_4)_2S$ and Na_2S. The etching rate of Na_2S was faster than that of $(NH_4)_2S$ and it caused the high roughness. Figure 2.19 shows the roughness data from AFM. Lianfeng Zhao [74] reported the effects of sulfur passivation on HfO_2/GaSb MOS capacitors with neutralized and unneutralized $(NH_4)_2S$ solutions at varied concentrations.

With neutralized sulfur solution, the interface became smoother and the D_{it} level was reduced. Figure 2.20 shows the distribution of the D_{it}. Uthayasankaran Peralagu [75] studied the impact of $(NH_4)_2S$ surface treatment on the electrical and interfacial properties of the Al_2O_3/p-GaSb by varying sulfide concentration. Prior to ALD of Al_2O_3, GaSb surfaces were treated in 1 %, 5 %, 10 %, and 22 % $(NH_4)_2S$ solutions for 10 minutes. The C-V characteristics changed by distinguished concentration of the sulfur solutions (figure 2.21). The C-V curve deteriorated with 22 % $(NH_4)_2S$ treatment. The author explained this was resulted from the increased roughness of interface and the interfacial layer between Al_2O_3 and GaSb (figure 2.22). The author also said that the interfacial layer was composed of Ga and S and so antimony-rich voids ranging from 15-25 nm in diameters, also appeared to form at non-specific regions along the interfacial layer.

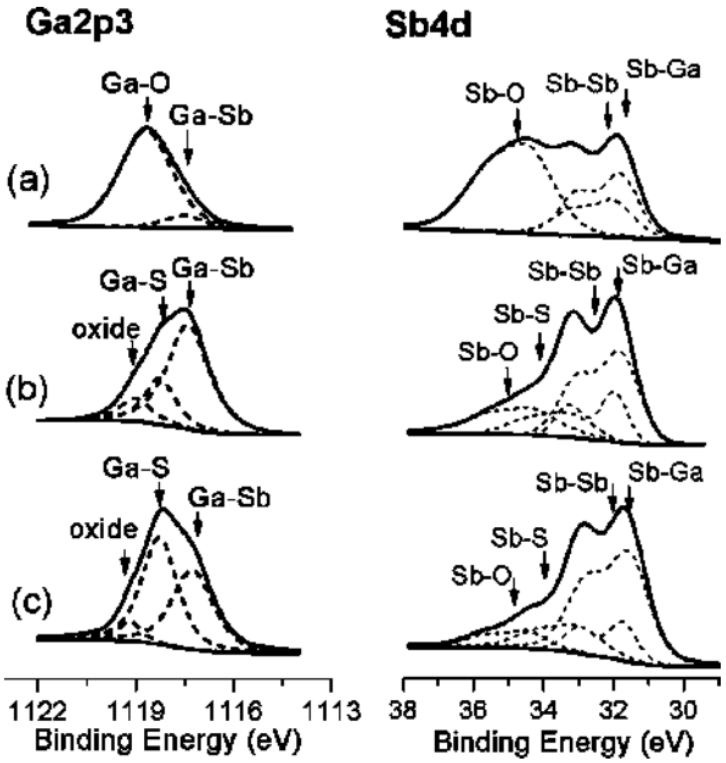

Figure 2.15 Ga 2p3 and Sb 4d XPS spectra of n-GaSb after various surface treatments. (a) degreased surface (b) dipped in HCl for 5 min. and rinsed by 2-propanol, followed by 1-h Na_2S aqueous passivation and DI water rinse (c) dipped in HCl for 5 min. and rinsed by 2-propanol, followed by 1-h Na_2S nonaqueous passivation (anthraquinone as oxidizing agent) and methanol rinse. [109]

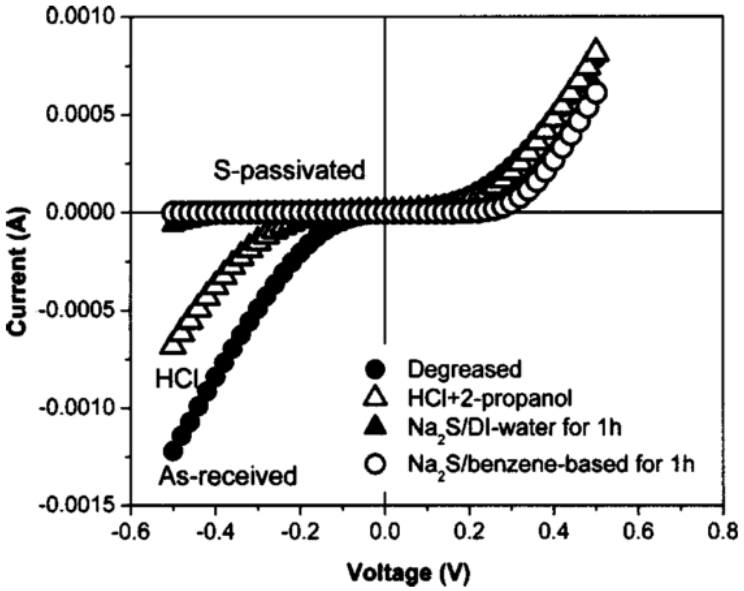

Figure 2.16 I–V curves of Au/n-GaSb Schottky contacts under forward and reverse biases. The diodes were fabricated on n-GaSb surfaces prepared by the processes (a) through (d). [110]

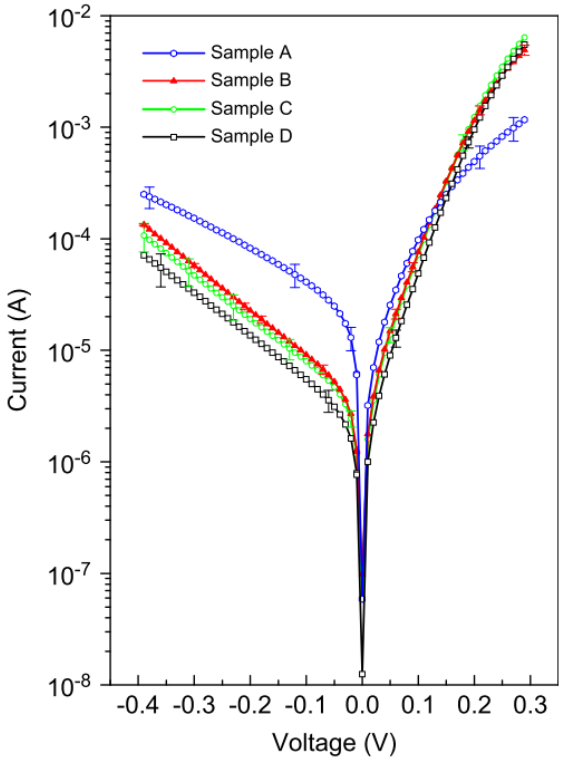

Figure 2.17 Forward and reverse bias I–V characteristics of Au/n-GaSb Schottky contacts, for samples (A–D). [79]

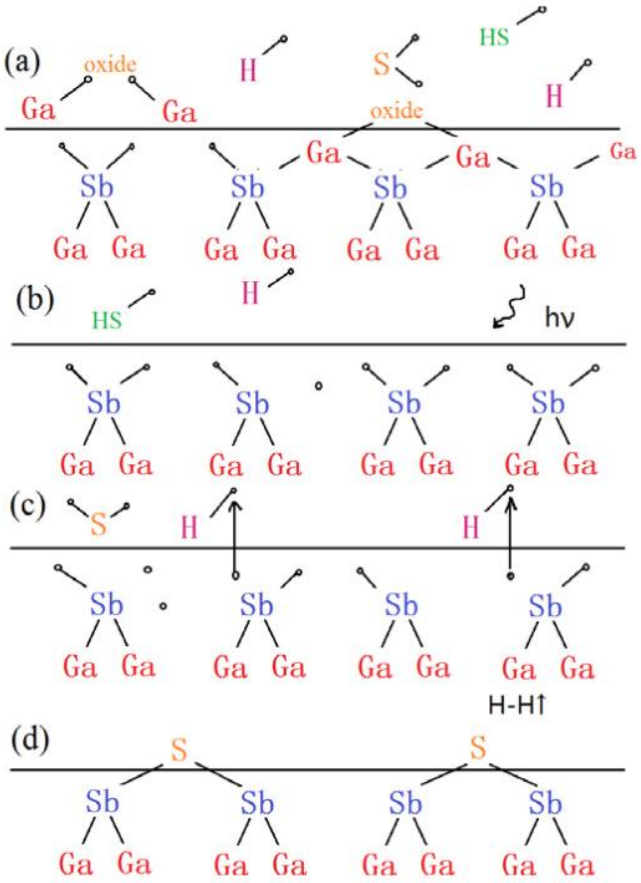

Figure 2.18 The process of sulfide passivation (a) breaking of bonds between Ga and Sb, (b) chemical reaction, (c) escape of an electron from the semiconductor into the solution, (d) formation of chemical bonds between sulfur and atoms of the semiconductor. [115]

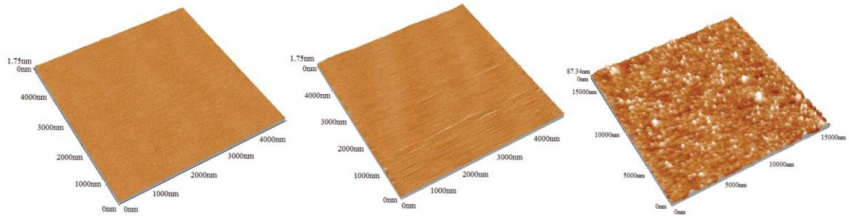

Figure 2.19 AFM images of the GaSb untreated, passivated by $(NH_4)_2S$ and Na_2S, respectively. [116]

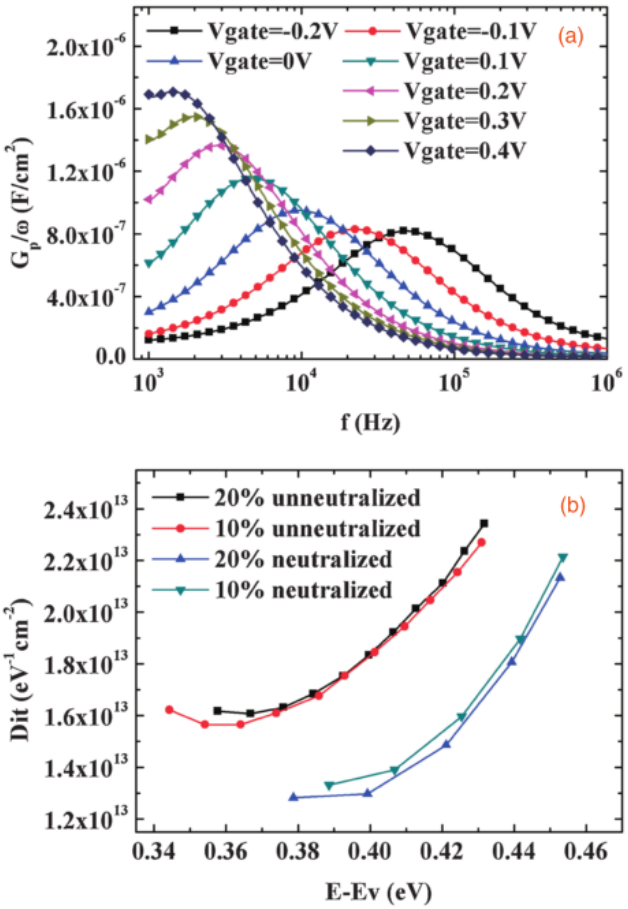

Figure 2.20 (a) Typical measured parallel Gp/w versus frequency curves for different gate biases of MOSCAPs passivated with 20% neutralized $(NH_4)_2S$ solution III. (b) Interface trap density (D_{it}) distribution of MOSCAPs treated with four different solutions. [74]

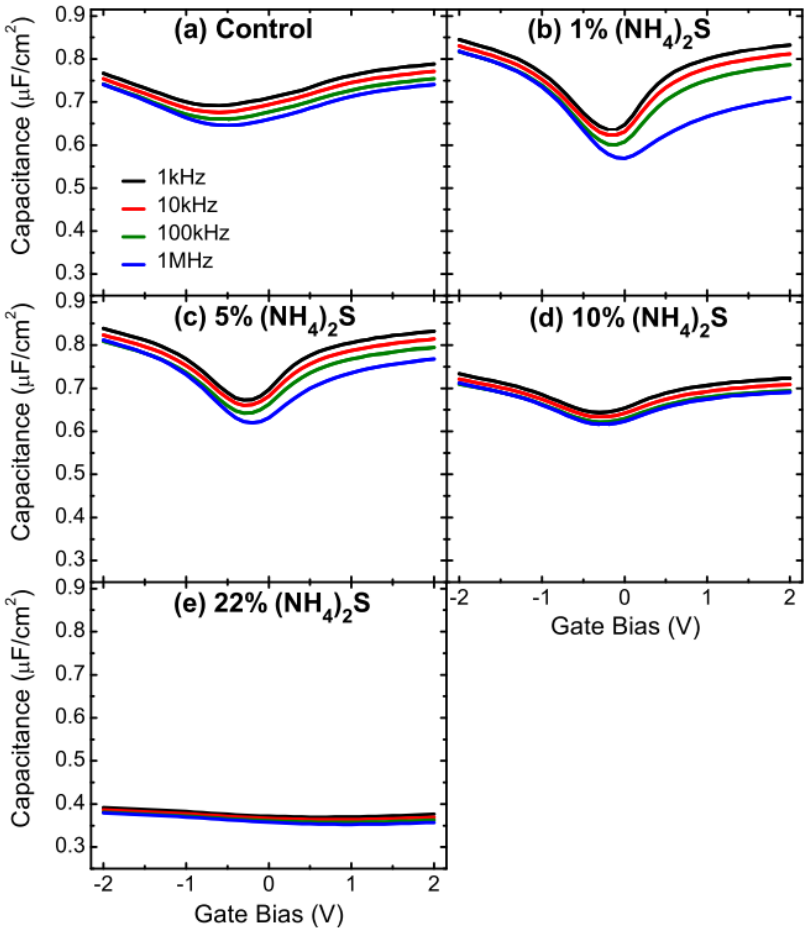

Figure 2.21 Multi-frequency (1 kHz to 1 MHz) CV characteristics (~295 K) of Au/Ni/Al2O3/p-GaSb MOS capacitors with (a) no treatment (control) along with (b) 1%, (c) 5%, (d) 10%, and (e) 22% $(NH_4)_2S$ treatments. [75]

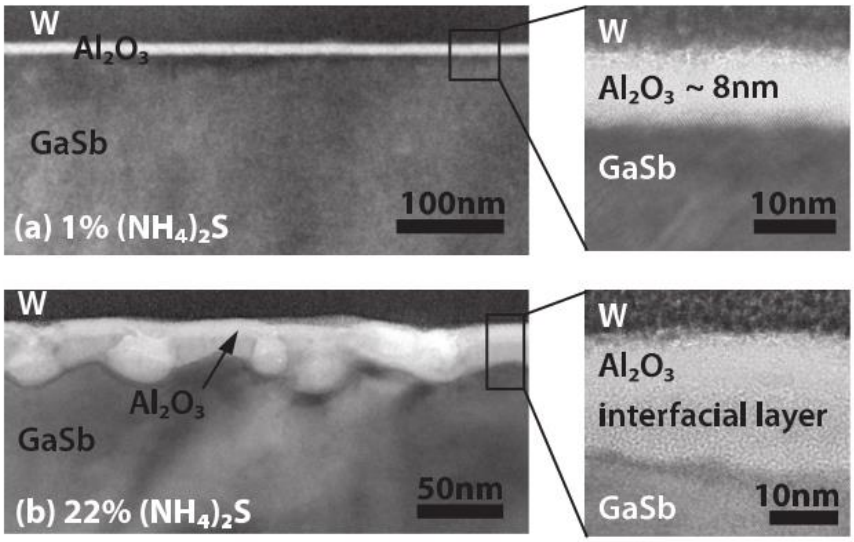

Figure 2.22 Cross-sectional TEM micrographs of (a) 1% and (b) 22% $(NH_4)_2S$ treated W/Al_2O_3/p-GaSb samples. [75]

2.2.4. Insertion of Passivation Layers

There have been numerous attempts to improve interfacial and electrical properties of GaSb devices by inserting passivation layers [65, 78, 81, 91]. Andrew Greene [81] tried to passivate the highly reactive GaSb surface with a thin InAs layer before depositing Al_2O_3. Figure 2.23 shows the Dit distributions and the C-V characteristics at different frequencies of the capacitors that this group fabricated. Masafumi Yokoyama [78] further studied on the impact of interfacial InAs layers on Al_2O_3/Gasb MOS interface properties. They varied the thickness of the InAs layer and figured out that certain thickness is effective to reduce the D_{it} level (figure 2.24). Rei-Lin Chu [91] deposited Y_2O_3 and Al_2O_3 onto GaSb(100) surfaces by molecular beam epitaxy and atomic layer deposition, respectively. This group stated the deposition of Y_2O_3 led to true inversion as indicated in the C-V characteristics, small hysteresis and frequency dispersion, and low gate leakage because of the formation of Ga-O, Ga-Y and Sb-Y bonds instead of the formation of GaO_x and SbO_x only (figure 2.25).

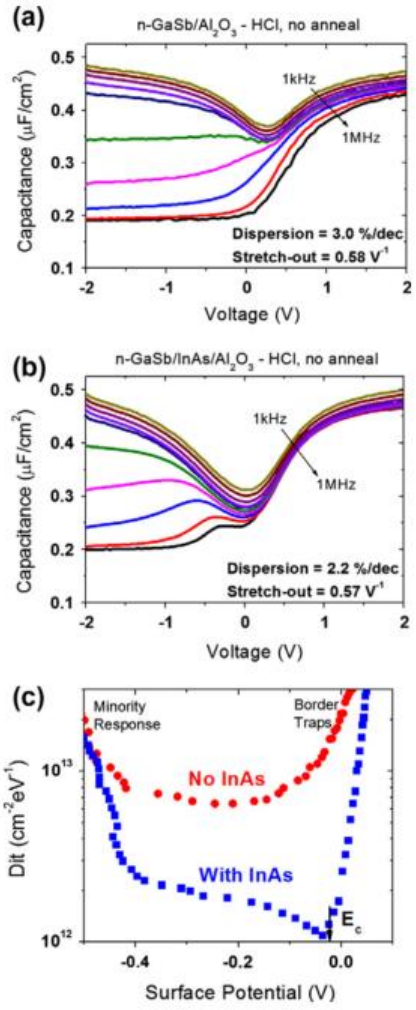

Figure 2.23 C–V characteristics at different frequencies of (a) n-GaSb MOS capacitor with 10 nm ALD Al_2O_3 and HCl pretreatment with no oxide annealing, (b) with interface InAs layer showing improved frequency dispersion in accumulation, and (c) the D_{it} extracted from High–Low frequency method showing that the InAs passivation layer results in a significant reduction in the D_{it}. [81]

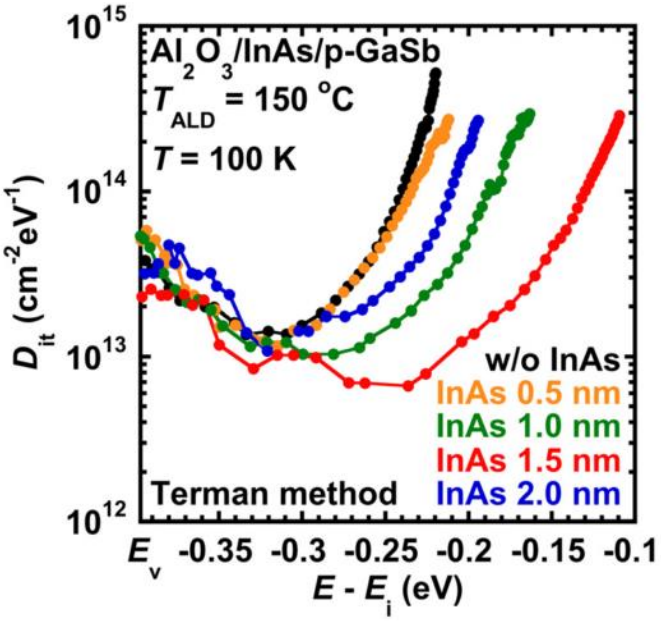

Figure 2.24 The D_{it}-(E-E_i) characteristics of Al_2O_3/InAs/p-GaSb MOSCAPs with the InAs thickness of 0, 0.5, 1.0, 1.5, and 2.0 nm, respectively, estimated by the Terman method using the 1MHz the C-V curves measured at 100 K. The black, orange, green, red, and blue colored curves are for the curves of the 0, 0.5, 1.0, 1.5, and 2.0 nm, respectively. The Al_2O_3 layers were deposited at 150 ℃. [78]

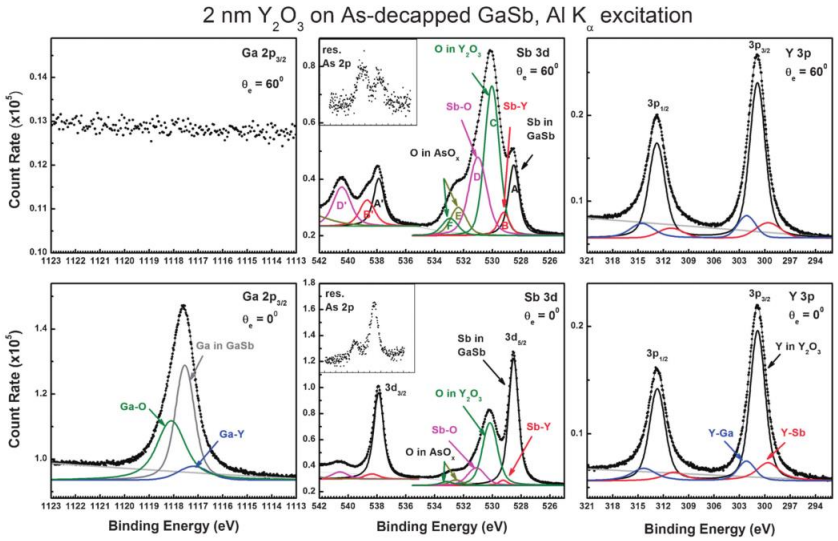

Figure 2.25 Analytical fit to the Ga $2p_{3/2}$, Sb 3d, and Y 3p states. [91]

2.3. Oxide Deposition on GaSb by Atomic Layer Deposition

2.3.1. Deposition of Almina by Atomic Layer Deposition

Atomic layer deposition (ALD) is now one of the very well known deposition techniques. ALD can be adopted in various applications as an important technology for thinfilms deposition [117]. Atomic level controlling of the film is necessary in the semiconductor industry due to the shrinkage of devices' size. Conformal deposition is especially able to be obtained by ALD in the high aspect ratio structure and is much better than that by other deposition techniques. It is resulted from the unique deposition mechanism of ALD. ALD use sequential, self-limiting surface reactions. These are demonstrated in figure 2.26. Normally, a typical ALD process is consisted with two sequences that are two surface reactions. Ideally, a monolayer is deposited per cycle because the number of reactive sites is limited. Therefore, film thickness can be easily controlled by differentiating the number of the cycles.

As mentioned above, ALD should have monolayer growth per cycle but the growth per cycle changes in actual ALD systems. It is resulted from decomposition, condensation, and desorption of precursors. Since temperature especially has a great impact on this behavior, finding the proper region for the ideal ALD is necessary for ALD. So called "ALD window" is the region that

shows nearly ideal ALD behavior. At low temperatures, the reactants are condensed onto the surface or the the thermal energy required for the surface reaction is not sufficient. On the contrary, at high temperatures, the precursors are thermally decomposed or desorbed.

The first reports of Al_2O_3 ALD using TMA and H_2O are back in late 1980s and early 1990s [118-119]. Using TMA and ozone for Al_2O_3 ALD was conducted by Goldstein and JB Kim [120-121]. The surface chemical reactions during Al_2O_3 ALD are described as follows [122-124]

$$AlOH^* + Al(CH_3)_3 \rightarrow AlOAl(CH_3)_2^* + CH_4$$

$$AlCH_3^* + H_2O \rightarrow AlOH^* + CH_4$$

where the asterisks denote the surface species. The Al_2O_3 ALD is a well understood system because the surface reactions are very suitable for self-limiting due to the formation of very strong Al-O bonds. Once calculate the reaction enthalpy, it shows one of the highest reaction enthalpies encountered for any ALD reaction. The reaction and the high reaction enthalpy is as follows [125]

$$2Al(CH_3)_3 + 3H_2O \rightarrow Al_2O_3 + 3CH_4 \qquad \Delta H = -376 \text{ kcal}$$

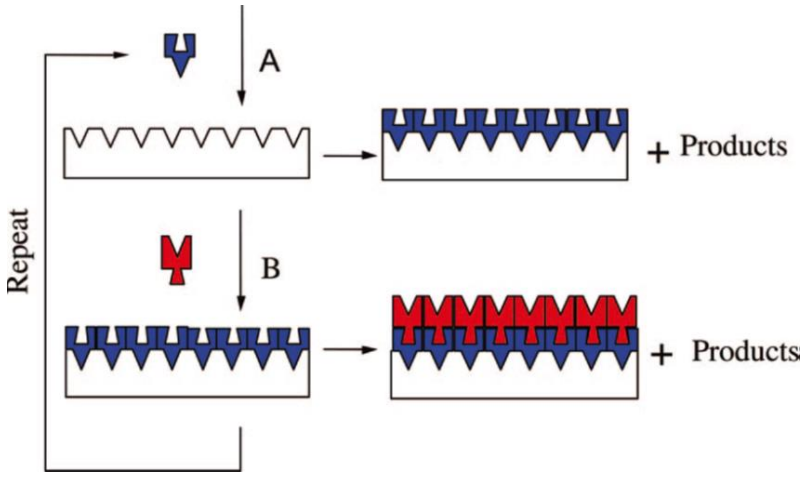

Figure 2.26 Schematic representation of ALD using self-limiting surface chemistry and an AB binary reaction sequence. (Reprinted with permission from ref 5. Copyright 1996 American Chemical Society.) [117]

2.3.2. Low Temperature Atomic Layer Deposition

Performing ALD at low temperatures is very important to maintain a low thermal budget. This low temperature ALD is also needed for thermally fragile substrates such as polymeric or biological materials. Thanks to some favorable thermochemistry, several ALD systems can provide the low temperature environments. Especially, the high exothermicity of the Al_2O_3 ALD surface reactions enables this low temperature ALD [126]. Even though there are a great deal of studies on ALD enhanced by plasma treatments and catalysts, lowering growth temperature should be handled in advance to well understand the ideal Al_2O_3 ALD. M. D. Groner [126] differentiated the reactions parameters. This group also showed that the density of Al_2O_3 decreased as the growth temperature decreased (figure 2.27).

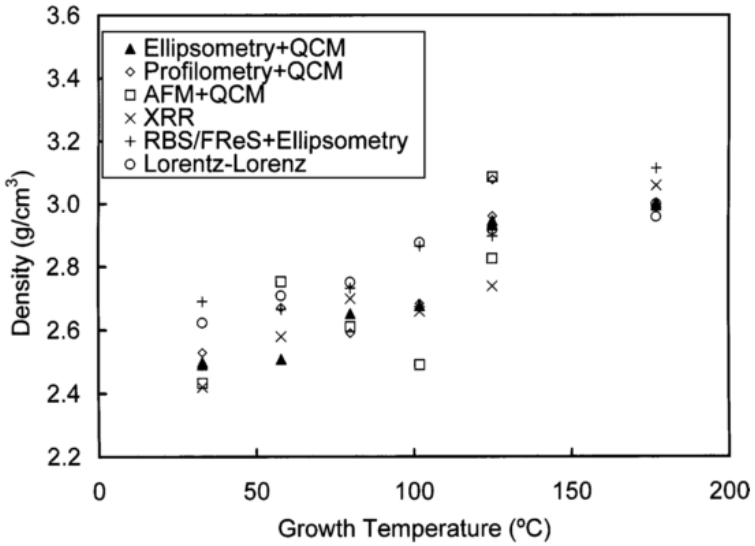

Figure 2.27 Density of Al_2O_3 ALD films versus growth temperature from 33 to 177 °C for the various methods. [126]

2.4. Post-Deposition Thermal Annealing Process

2.4.1. Rapid Thermal Process

IBM started rapid thermal processing (RTP) in the late 1960s on making silicon with sub-micro-meter details. Pulsed laser beams on boron-doped silicon with paint-on phosphorus was used [127]. In the 1970s, laser annealing was frequently used for rapid thermal annealing in inert ambiences [128-131]. The editor of the book called as “Rapid Thermal Processing: Science and Technology” summarized various usages of RTP [132]. RTP has been used for epitaxy growth, thermal oxidation of dielectrics, depositing thinfilms, junction formation, silicides formation, and defects annealing. The defect annealing was focused in this study. Figure 2.28 shows the defect annealing effects. The author addressed various defects formation kinetics including point defect sources and types of extended defects. For the extended defects, five different types of damages were introduced. The damages are well explained in the paper [132]

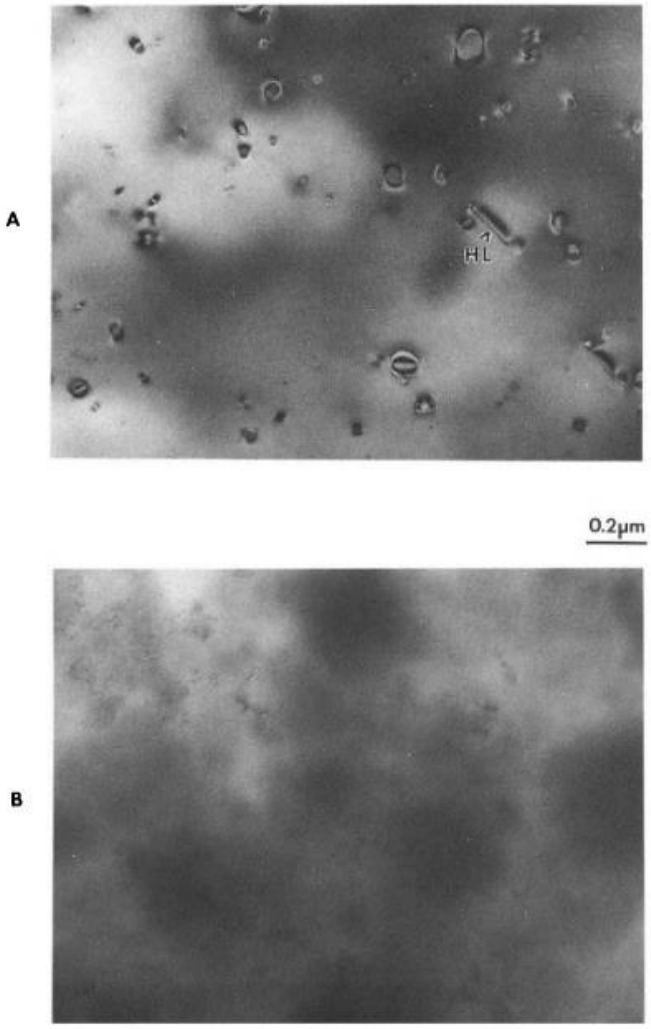

Figure 2.28 Difference between (a) furnace annealing 900 ℃ 120 min and (b) rapid thermal annealing 1100 ℃ 64 seconds. [132]

2.4.2. Forming Gas Annealing

There is a report [156] about that the D_{it} of oxidized silicon surfaces is significantly reduced by Post-Metallization Anneal (PMA). In this study [156], the D_{it} was reduced by PMA in an ambient including H_2, while it was much increased as hydrogen or water in the annealing atmosphere was reduced toward vacuum. Rezouk [157] suggested that the origins of fixed charges and interface states were very similar while Montillo [156] suggested they were not completely the same. Forming gas annealing is used to reduce interfacial trap density between Si and SiO_2. The dangling bonds by SiO_x ($x < 2$) can be filled up with hydrogen by FGA.

2.5. Electrical Characterization of III-V MOS Devices

2.5.1. The Terman Method for the D_{it} Extraction

Terman [158] firstly introduced the Terman method for the D_{it} extraction. The Terman method evaluates the D_{it} by measuring ΔV at a certain temperature. Before talking about the principles of the Terman method, it is necessary to look out what are the donor-like traps and acceptor-like traps in interfacial traps. The interfacial traps are divided into two different types; donor-like traps and acceptor-like traps. Between E_v and E_i, there are normally donor-like traps and between E_c and E_i, there are normally acceptor-like traps. These traps change their charges when the gate voltage is differed. When the donor-like traps are filled with electrons, they are charged neutrally while the acceptor-like traps are charged negatively. When the donor-like traps loses their electrons, then they are charged positively while the acceptor-like traps are charged neutrally. The effect of bias voltage on surface-state occupancy is demonstrated in figure 2.29. Because of this, when measuring the C-V of capacitors, it shows a stretch out of the C-V curves. Figure 2.6 well illustrated the stretch out in the C-V curves. The the Terman method extracts D_{it} by calculating the stretch-out. The stretch out in a C-V curve is obtained by comparing it with an ideal CV curve (no D_{it}) and allows for quantification of D_{it}. The formula for quantifying D_{it} is as follow [158]

$$D_{it}(\Psi_s) = \frac{C_{ox}}{q}\left[\left(\frac{d\Psi_s}{dV_g}\right)^{-1} - 1\right] - C_s(\Psi_s)$$

where,

D_{it}: the interface trap density

C_{ox}: the oxide capacitance

Ψ_s: the semiconductor band bending, surface potential

.$\Delta V_g = V_g - V_{g(ideal)}$

V_g: the applied gate voltage

$C_s(\Psi_s)$: the ideal semiconductor capacitance.

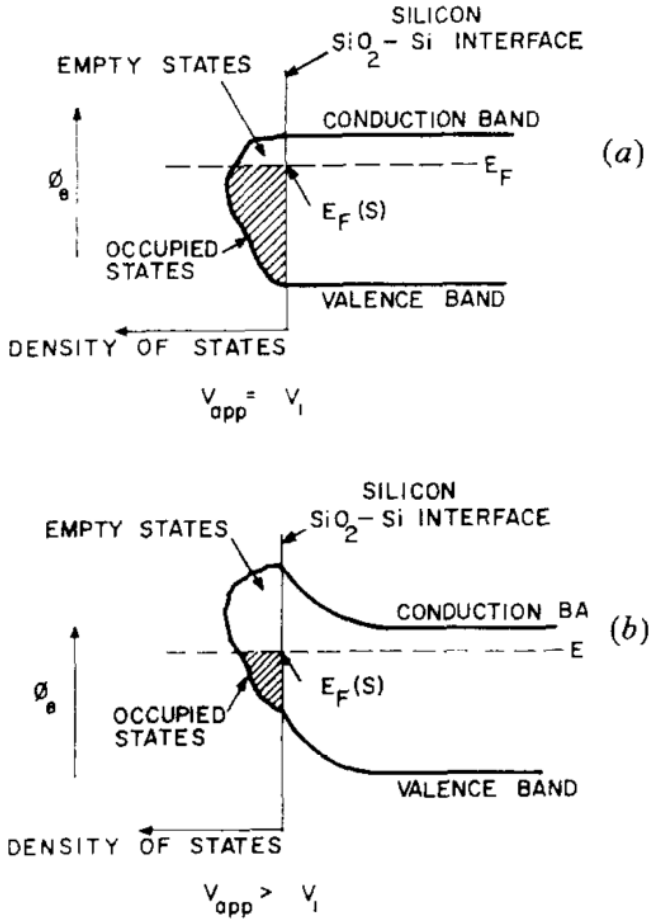

Figure 2.29 Effect of bias voltage on surface-state occupancy. [158]

3. Deposition of Alumina on GaSb by Low-Temperature Atomic Layer Deposition

3.1. Introduction

As mentioned in a chapter 2.1.1., GaSb forms the native oxide rapidly with air exposure. Even worse than that, the native oxide of GaSb actually oxidize GaSb and so the bad circulation of the oxidation of GaSb occurs. Because of this, GaSb capacitors suffer from the severe stretch-out in the C-V curves. Therefore, one of the key approaches to alleviate this stretch-out is to prevent further oxidation in an ALD chamber and right after HCl cleaning. Since the ALD machine that has been used for this study does not have a loading chamber, the samples should be loaded into a hot chamber manually with air exposure. It is inevitable to accelerate the formation of the native oxide when the samples are loaded into the hot chamber. Lowering the process temperature can be a solution to reduce the formation of the native oxide when the samples are loading into the chamber. In this study, the deposition temperature varies from 100 to 310 ℃ to alleviate the formation of the native oxide.

3.2. Experimental Procedures

The schematic configuration of ALD machine is in figure3.1. The detailed conditions for it are also shown in table 3.1. 2 inch p-type undoped GaSb wafers with a carrier concentration of 2 x 10^{17} cm^{-3} were used for fabricating GaSb MOS capacitors. GaSb wafers were diced by dicing saw into ~1 cm length. After dicing the GaSb wafers, degreasing GaSb surfaces was performed by dipping them in acetone, ethanol, isopropyl alcohol (IPA) for 3 minutes each. Prior to depositing gate oxide, the GaSb pieces were dipped in diluted HCl (9 %) for 5 minutes. The GaSb pieces were then transferred to the ALD chamber within several minutes.

To fabricate GaSb MOS capacitors, Al_2O_3 was selected for gate oxide. 10 nm thick Al_2O_3 was deposited by ALD. As mentioned in the introduction part, the deposition temperatures varied from 100 to 310 ℃. Trimethylaluminium ($Al(CH_3)_3$, TMA) and de-ionized water were used as a Al source and an oxidant respectively. The thickness of oxides were measured by a spectroscopic ellipsometry (SE).

For the metal electrode of the MOS capacitors, Platinum was deposited by electron beam evaporation through shadow mask with an area of 6.6 x 10^4 μm^2 placed on each sample to form pattered gate electrodes. Indium paste was applied as the backside contacts.

Figure 3.2 shows the experimental process conditions for MOS capacitors fabrications as addressed above.

For the C-V measurements, Pt gate electrodes and In backside contact of GaSb MOS capacitors were connected with LCR meter (HP4284 Impedance analyzer). Measurement temperature was kept at room temperature.

The C-V frequency dispersions were evaluated using 4 different frequencies from 50 kHz to 1 MHz. The V_g sweep during the measurements was ranged from 2 V to -2 V.

The interface states density (D_{it}) in the GaSb band gap were extracted by the Terman method which can calculate the D_{it} from the stretch out in the C-V curves comparing it to an ideal the C-V curve (no D_{it}).

Surface chemical bonding states of the samples were characterized by x-ray photoelectron spectroscopy (XPS) with monochromatic Al K-α source (hv=14876.7 e/V) For the XPS analysis, 2 nm of gate oxide was deposited on GaSb wafers but the metal contacts were not deposited on the GaSb wafers. Ga 3d and Sb 4d peaks were mainly discussed with the electrical results.

For X-ray reflectometry (XRR) measurements, 10 nm thick oxide was deposited on Si wafers but the metal contacts were not deposited on the Si wafers for XRR analysis.

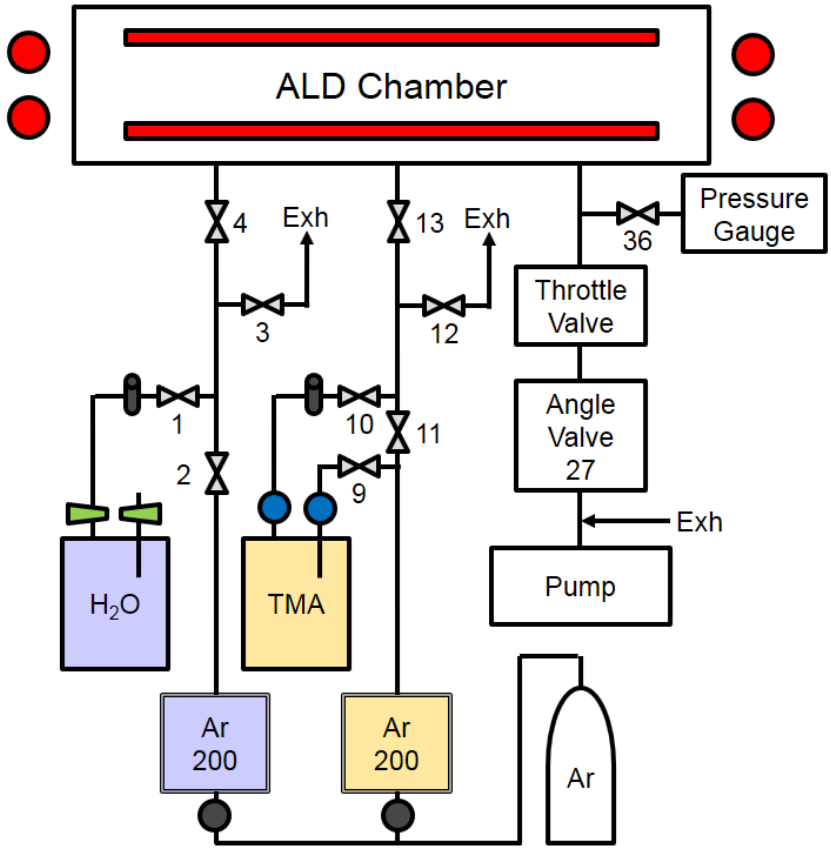

Figure 3.1 The schematic configuration of thermal ALD machine employed in this study. Color red indicates heating area.

Table 3. 1 The detailed conditions for ALD

Substrate	GaSb
Deposition	Al_2O_3
Precursor	TMA
Source temperature	Room temperature
Oxidant	H_2O
Substrate temperature	100~310 ℃
Wall temperature	125 ℃
Carrier Ar flow	200 sccm
Purge Ar flow	200 sccm

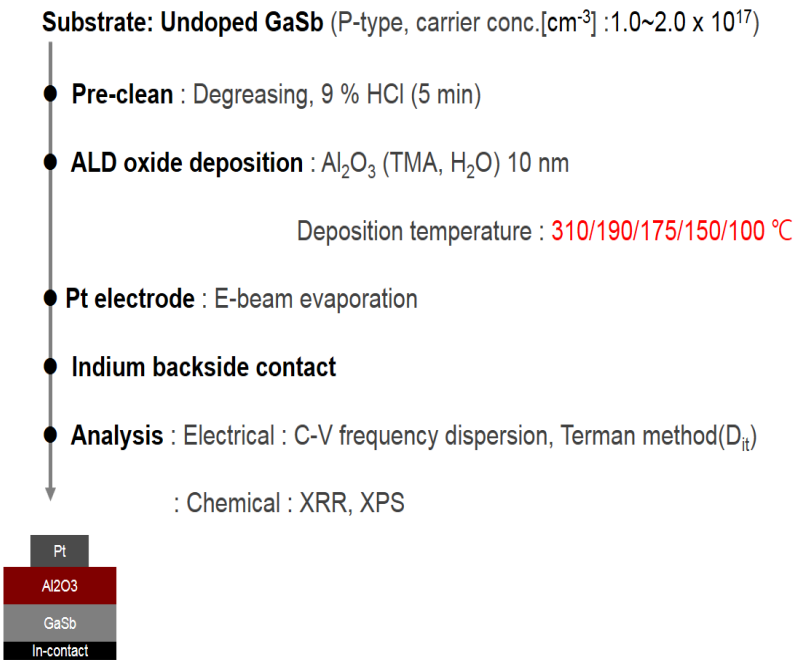

Figure 3.2 The experimental process conditions for MOS capacitors fabrication.

3.3. Results and Discussions

Lowering deposition temperature of ALD is essential to prevent further oxidation after cleaning and before depositing thinfilms.

Figure3.3 shows the normalized capacitance-voltage curves of GaSb MOS capacitors at various deposition temperatures. Clearly, the stretch out in the C-V curve was affected by the deposition temperature. The stretch out in the C-V curves was alleviated as the deposition temperature was lowered. The C-V curve showed the best result at a deposition temperature of 150 ℃. However, the C-V curve at became worse with the deposition temperature of 100 ℃ compared to 150 ℃.

To figure out the deterioration in the sample with the deposition temperature of 100 ℃, X-ray reflectometry (XRR) analysis was conducted. The XRR results are shown in figure 3.4. It showed similar behavior with the results shown in figure2.38. As the deposition temperature decreased, the densities of Al_2O_3 on Si wafers decreased. Since most of Al_2O_3, deposited by ALD, is amorphous, once the density of the Al_2O_3 film decreases, it can cause high structure disorder. Due to this high structure disorder, structural defects such as dangling bonds are formed more. Dangling bonds are known as one of the main causes of deterioration of the C-V curve. Therefore, the deterioration of the C-V curve with the deposition temperature of 100 ℃, was resulted from

increased numbers of structural disorders (i.e dangling bonds) which are formed by reduced density of the amorphous film, Al_2O_3.

In fact, in the range of 150 ~ 300 ℃, the stretch-out in the C-V curves has been improved as the deposition temperature decreased even though the density of the oxide film decreased. This is an interesting result because the dangling bonds, made from low density of amorphous film, can trap charges and have an impact on the C-V curve. It can be explained by X-ray photoelectron spectroscopy (XPS) analysis. To figure out the specific differences, peak devolution was carried out. The XPS results are shown in figure3.5. Once look at the results for Ga3d XPS peaks, it is obvious that the amount of meta-stable Ga_2O was formed less with low deposition temperature. The pure Ga_2O_3 ratio over meta stable Ga_2O decreased as the deposition temperature increases. It shows that GaSb makes the native oxides abruptly at a high temperature. It is because when GaSb forms the native oxides, it abruptly makes metastable and oxygen-deficient oxide (Ga_2O) rather than the pure Ga_2O_3 due to the lattice mismatch between GaSb and the native oxide. As shown in figure2.21 and figure 2.22 and the studies[71, 107], the formation of pure Ga_2O_3 is one of the keys to alleviate the Fermi-level pinning for GaSb devices because pure Ga_2O_3 forms a low-defect interface [71, 107, 159-163].

Finally, the energy distributions of the D_{it} are illustrated in figure3.6. The the D_{it} value decreased as the deposition temperature decreased and increased with

the deposition temperature of 100 ℃. These results are very consistent with the C-V curves results. The reduction in the D_{it} level was resulted from the increased ratio of the pure Ga_2O_3 over metastable Ga_2O which was revealed from XPS analysis.

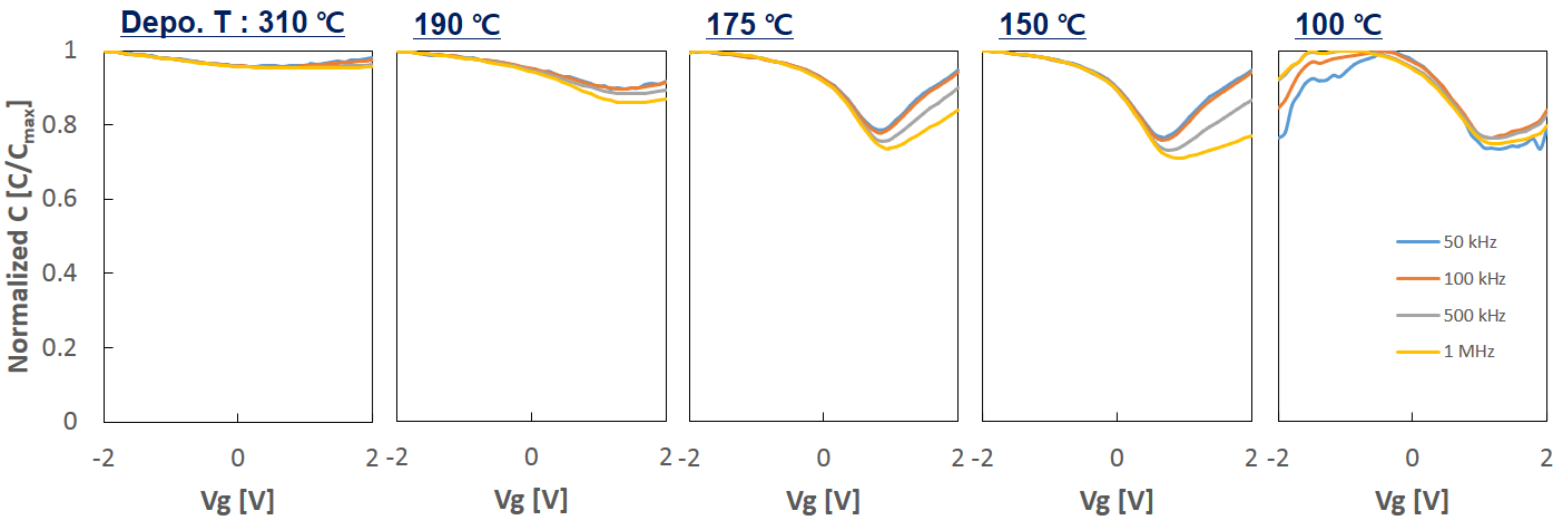

Figure 3.3 Normalized capacitance-voltage curves of GaSb MOS capacitors at various deposition temperatures.

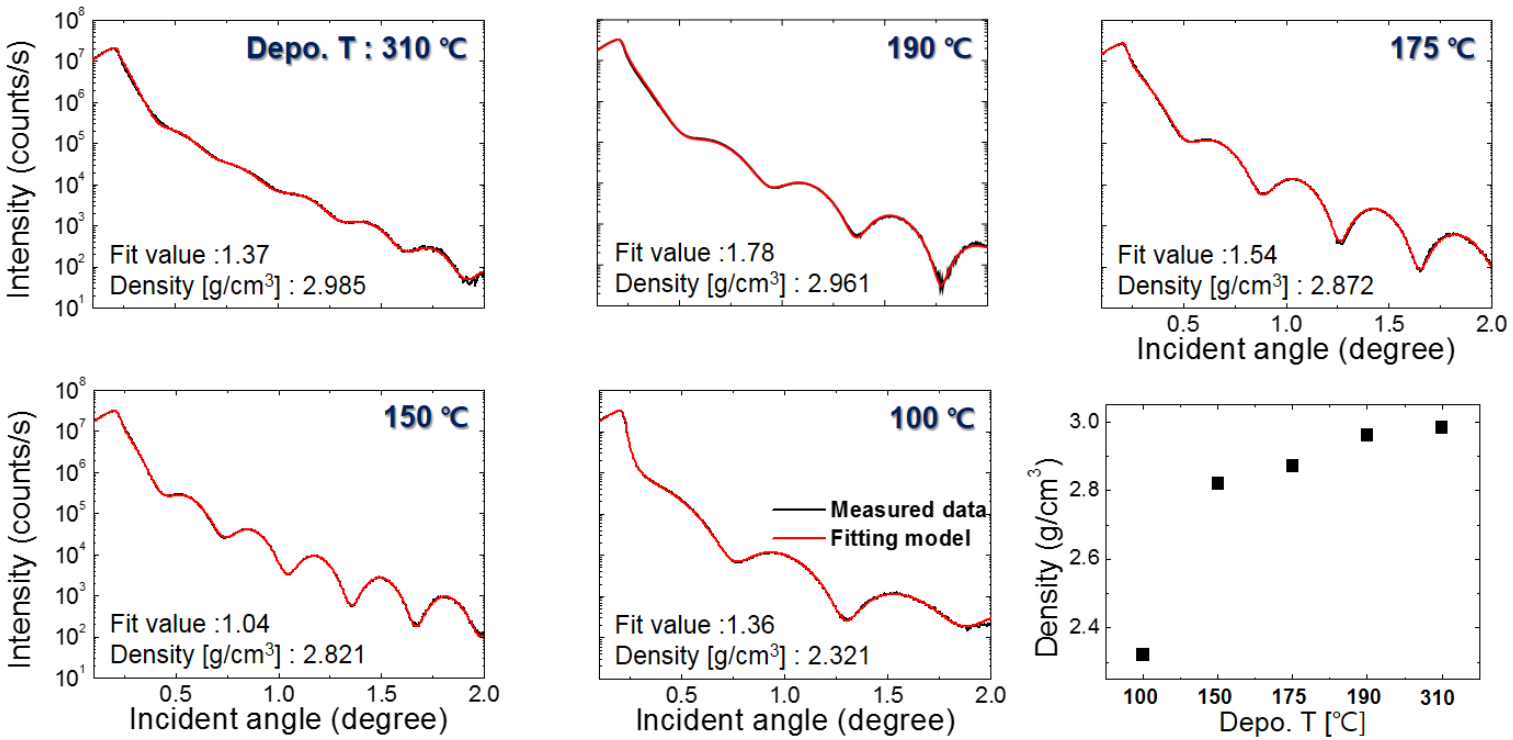

Figure 3.4 X-ray reflectometry (XRR) results of Al_2O_3 on Si wafers with various deposition temperatures. The right bottom graph shows the effects of deposition temperature on density of Al_2O_3 on Si wafers.

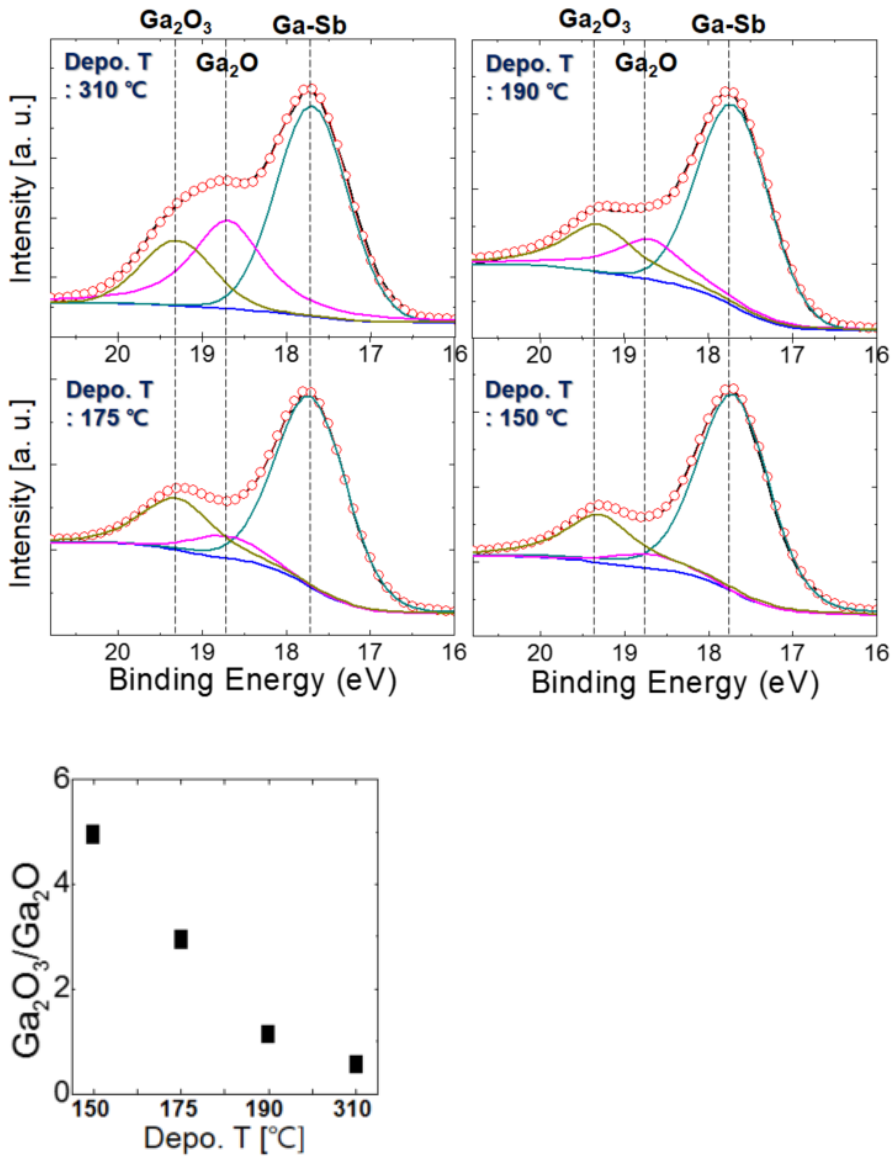

Figure 3.5 XPS spectra of Ga 3d for 2 nm thick Al_2O_3 on GaSb. The left bottom shows the effects of deposition temperature on the ratio of Ga_2O_3 over Ga_2O.

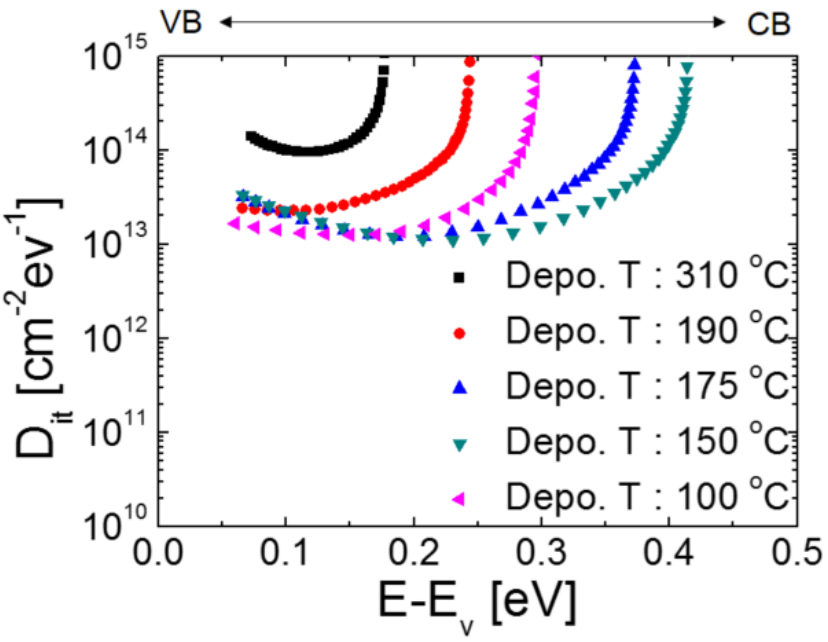

Figure 3.6 Energy distribution of the D_{it} of Al_2O_3/GaSb MOS capacitors.

3.4. Summary

In summary, the stretch-out in the C-V curves was successfully alleviated by lowering the deposition temperature of ALD from 310 ℃ to 150℃. It was resulted from the increased ratio of the pure Ga_2O_3 over meta stable Ga_2O at the deposition of 150 ℃. The pure Ga_2O_3 is known to form a low-defect interface with GaSb.

Fast oxidation of GaSb with air exposure occurs after cleaning the GaSb surfaces with diluted HCl especially when the GaSb substrates are transferred to the chamber. Also due to the absence of a loading chamber, the oxidation of GaSb is accelerated when GaSb is loaded into the hot chamber. Therefore lowering the deposition temperature was essential for ex-situ deposition. The deposition temperature varied from 100 to 310 ℃. At the deposition temperature of 100 ℃, the C-V curve deteriorated because structural defects (i.e. dangling bonds) were formed from high structural disorder which is resulted from the decreased density of the amorphous film, Al_2O_3. In the range of 150 to 310 ℃, however, the stretch out in the C-V curves was improved as the deposition temperature decreased even though the density of Al_2O_3 was decreased. It was turned out that the ratio of pure Ga_2O_3 over meta stable Ga_2O was increased as the deposition temperature decreased. The pure Ga_2O_3 is known as one of the keys to alleviate the Fermi-level pinning since it produces a low-defect interface with GaSb. The D_{it} level also decreased as the deposition temperature decreased but increased at the deposition temperature of 100 ℃.

4. Post-Deposition Rapid Thermal Process of Alumina Deposited GaSb

4.1. Introduction

As mentioned in chapter 2.1.2, there are four different defect charges which can be formed in oxide/semiconductor devices. What we need to carefully consider while fabricating GaSb MOS capacitors are two defects: interface trapped charge (Q_{it}) and fixed oxide charge (Q_f). How they are formed and how they can be removed were already explained in chapter 2.1.2.

Takashi Hori [99] summarized the relationship between fixed-charge density (N_f) and interface state density (D_{it}) (already discussed in chapter 2.4.2.). Figure 2.46 exhibits an apparent correlation between N_f and the D_{it}, indicating that fixed charges and interface states may have a common origin [99]. Therefore, it is helpful to adopt the removal technique for fixed oxide charge to reduce the D_{it} level. The removal technique is annealing in a nitrogen ambience or argon ambience, which are both inert gases. This technique is to give enough thermal energy for reconstruction of bonds to reduce structural disorder.

Also, Q_{it}, which is made in the SiO_2/Si interface, can be removed by hydrogen or hydrogen/nitrogen thermal treatments at low temperatures (~ 450 ℃). It is called as forming gas annealing (FGA). The concept of this method is filling up dangling bonds with hydrogen to reduce the D_{it} level. However, for Ga_2O_3 and Ga_2O, there are studies [77, 93, 164-167] showing that hydrogen thermal treatment causes the reduction of Ga_2O_3 to Ga_2O. The reduction formula is as below [77]

$$Ga_2O_3 + 2H_2 \rightarrow Ga_2O + 2H_2O \uparrow$$

E. Weiss[77] reported that the formation of Ga_2O started at 100 ℃ with H_2 thermal treatment.

4.2. Experimental Procedures

The first experiment was for observing the effects of post deposition RTP in a nitrogen ambience on Al_2O_3/GaSb MOS capacitors.

2 inch p-type undoped GaSb wafers with a carrier concentration of 2 x 10^{17} cm^{-3} were used for fabricating GaSb MOS capacitors. GaSb wafers were diced by dicing saw into ~1 cm length. After dicing the GaSb wafers, degreasing was performed by dipping them in acetone, ethanol, isopropyl alcohol (IPA) for 3 minutes each. Prior to depositing gate oxide, the GaSb pieces were dipped in diluted HCl (18 %) and $(NH_4)_2S$ (5 %) for 5 minutes each. The GaSb pieces were then transferred to the ALD chamber within several minutes.

To fabricate GaSb MOS capacitors, Al_2O_3 was selected as gate oxide. 10 nm thick Al_2O_3 was deposited by ALD. The deposition temperature was set at 150 ℃. Trimethylaluminium ($Al(CH_3)_3$, TMA) and de-ionized water were used as a Al source and an oxidant respectively. The thickness of oxides was measured by a spectroscopic ellipsometry (SE).

After depositing Al_2O_3 by ALD, the samples were transferred into a RTP chamber and annealed in a nitrogen ambience for 30 seconds at various temperatures from 150 ~ 300 ℃. The base pressure of RTP was ~ 7 mTorr. Nitrogen gas flow was 200 sccm to make process pressure to be about 100 mTorr.

For the metal electrode of the MOS capacitors, Platinum was deposited by electron beam evaporation through shadow mask with an area of 6.6 x 10^4 μm^2 placed on each sample to form pattered gate electrodes. Indium paste was applied as the backside contacts.

Figure. 4.1 shows the experimental process conditions for the post deposition RTP in a nitrogen ambience.

For the C-V measurements, Pt gate electrodes and In backside contact of GaSb MOS capacitors were connected with LCR meter (HP4284 Impedance analyzer). Measurement temperature was kept at room temperature.

The C-V frequency dispersions were evaluated by using 4 different frequencies from 50 kHz to 1 MHz. The V_g sweep during the measurements was ranged from 2 V to -2 V.

The interface states density (D_{it}) in GaSb band gap were extracted by the Terman method which can calculate the D_{it} from the stretch-out in the C-V curves compare to an ideal the C-V curve (no D_{it}).

Surface chemical bonding states of the samples were characterized by x-ray photoelectron spectroscopy (XPS) with monochromatic Al K-α source (hv=14876.7 e/V) For the XPS analysis, 2 nm of gate oxide was deposited on GaSb wafers but the metal contacts were not deposited on the GaSb wafers. Ga 3d and Sb 4d peaks were mainly discussed with the electrical results.

For X-ray reflectometry (XRR) measurements, 10 nm thick oxide was deposited on Si wafers but the metal contacts were not deposited on the Si wafers for XRR analysis.

Atomic force microscope (AFM) analysis was performed to evaluate the roughness of the samples. For this, 10 nm thick oxide was deposited on GaSb wafers but the metal contacts were not deposited on the GaSb wafers.

The second experiment was for observing the effects of 5 % H_2 thermal treatment on Al_2O_3/GaSb MOS capacitors.

Most of the experimental process conditions are same as above except cleaning method (same as the one in the experiment with pre-deposition RTP in chapter 6) and post deposition annealing conditions. The different cleaning conditions are as below. The GaSb pieces were dipped in diluted HCl (9 %) and $(NH_4)_2S$ (5 %) for 1 minutes and 5 minutes respectively. After wet cleaning, the

GaSb pieces were transferred to a RTP chamber and annealed at 575 ℃ for 30 seconds. Prior to deposit a thinfilm by ALD, the GaSb pieces were dipped in 5% $(NH_4)_2S$ for 1 min. The gas mixed with 5 % H_2 and 95 % N_2 was used for the post-deposition annealing process at various temperatures (250 ~ 550 ℃) for 5 minutes.

Figure 4.2 shows the experimental process conditions for the 5 % H_2 thermal treatment.

The third experiment was for verifying the actual effects of the hydrogen gas annealing by doubling the flux of hydrogen gas.

All of the experimental process conditions are same as the ones for the second experiment except the annealing conditions. The only difference is the flux of hydrogen gas. The gas mixed with 10 % H_2 and 90 % N_2 was used at various temperatures (200 ~ 350 ℃) for 5 minutes.

Figure 4.3 shows the experimental process conditions for the 5 % H_2 thermal treatment.

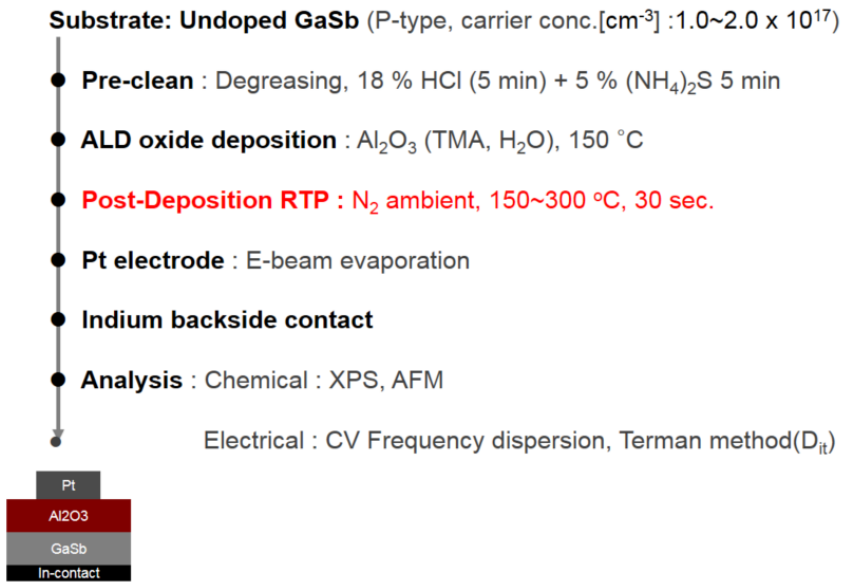

Figure 4.1 The experimental process conditions for MOS capacitors fabrication. (to see the effects of post deposition RTP in a nitrogen ambience on Al_2O_3/GaSb.)

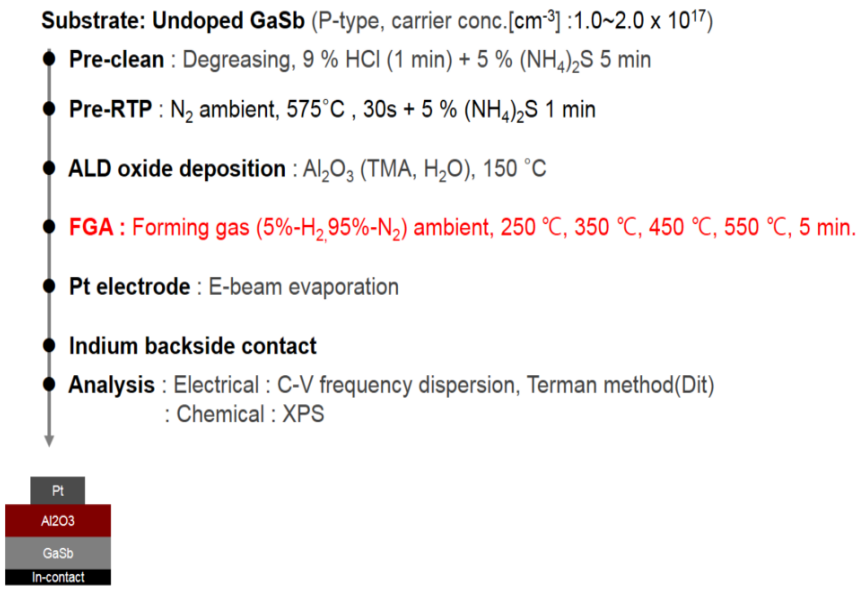

Figure 4.2 The experimental process conditions for MOS capacitors fabrication. (to see the effects of 5 % H_2 thermal treatment on Al_2O_3/GaSb.)

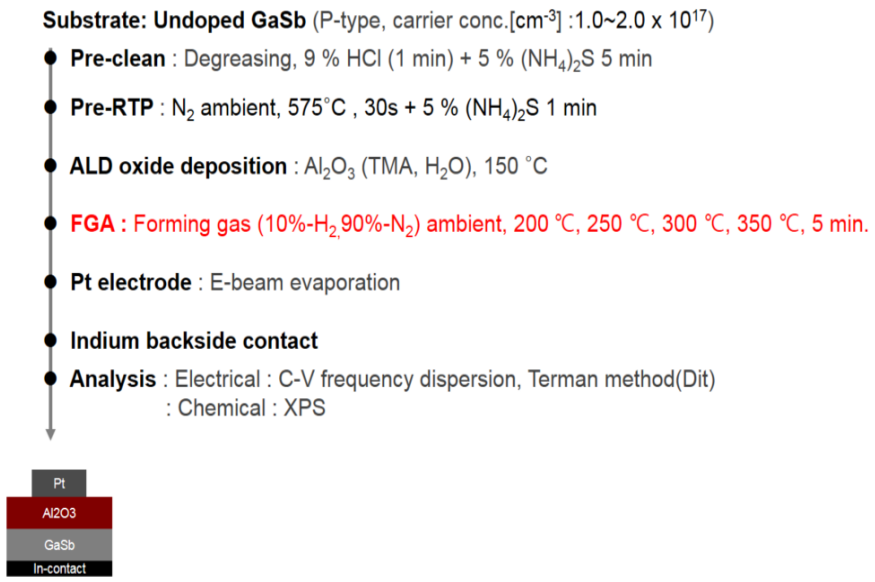

Figure 4.3 The experimental process conditions for MOS capacitors fabrication. (to see the effects of 5 % H_2 thermal treatment on Al_2O_3/GaSb.)

4.3. Results and Discussions

4.3.1. Post-Deposition Rapid Thermal Process in a Nitrogen Ambience

The removal technique for Q_f is annealing the samples in a nitrogen ambience or argon ambience, which are both inert gases. This technique is to give enough thermal energy for reconstruction of bonds to reduce structural disorder.

In figure 4.4, the normalized capacitance-voltage curves of GaSb MOS capacitors with the post-deposition RTP at various RTP temperatures in a nitrogen ambience are demonstrated. The stretch-out in the C-V curves was alleviated by the post-deposition RTP at 150 ℃, 200 ℃, and 250 ℃ and deteriorated by the post-deposition RTP at 300 ℃. Once compare the normalized the C-V curve at 1 MHz frequency, it is clear that as the RTP temperature increased the minimum normalized capacitance in depletion region was reduced (figure.4.5). When there are oxygen vacancies, the C-V curve moves parallel to left (negative voltage side) because the oxygen vacancies are positively charged. The voltage shift (ΔV_{shift}) by oxygen vacancies was recovered a little in figure 4.5. It shows that oxygen vacancies from amorphous Al_2O_3 and interface between Al_2O_3 and GaSb were slightly recovered by the post-deposition RTP in a nitrogen ambience because of the low annealing temperature.

Figure 4.6 shows the AFM analysis results of 10 nm thick Al_2O_3 on GaSb after the post-deposition RTP in a nitrogen ambience at various temperatures for 30 seconds. The surface roughness decreased by the post-deposition RTP at 150 ℃, 200 ℃, and 250 ℃ and increased by the post-deposition RTP at 300 ℃. Increased roughness indicates that structural defects (i.e. dangling bonds) are increased. These structural defects have an impact on the C-V curves.

Figure.4.7 illustrates Ga3d XPS peaks of 2 nm thick Al_2O_3 on GaSb after the post-deposition RTP in a nitrogen ambience at various temperatures for 30 seconds. The ratio of the pure Ga_2O_3 over meta-stable Ga_2O increases as the post-deposition RTP increases (the best at 250 ℃) and decreased with the post-deposition RTP at 300 ℃. It indicates that meta-stable Ga_2O changed to stable Ga_2O_3 by thermal energy given from the post-deposition RTP at 250 ℃. Also, oxidation of GaSb was accelerated by the post-deposition RTP at 300 ℃. The increased amount of metastable Ga_2O is the clue that shows that the GaSb was oxidized abruptly.

Figure 4.8 demonstrates Sb 4d peaks results of 2 nm thick Al_2O_3 on GaSb after the post-deposition RTP in a nitrogen ambience at various temperatures for 30 seconds. The Sb-oxide decreases as the post-deposition RTP temperature increases. The ratio of the elemental Sb over Sb-oxide increases as the post-deposition RTP temperature increases. It indicates that remaining Sb-oxide oxidized GaSb and changed to the elemental Sb by the post-deposition RTP at 300 ℃.

Finally, figure 4.9 shows the energy distribution of the D_{it} of Al_2O_3/GaSb MOS capacitors. the D_{it} level decreased by the post-deposition RTP at 150 ℃, 200 ℃, and 250 ℃ and increased by the post-deposition RTP at 300 ℃. This result is very consistent with the normalized the C-V curves and other chemical analysis results.

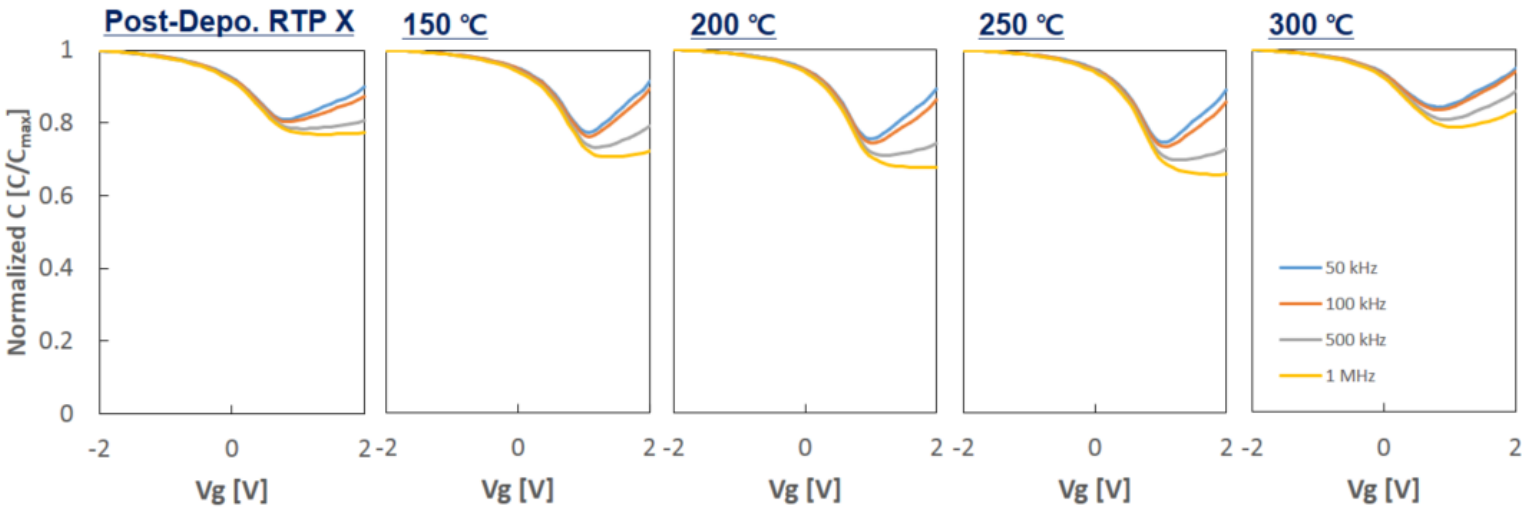

Figure 4.4 Normalized capacitance-voltage curves of GaSb MOS capacitors with the post-deposition RTP at various RTP temperatures in a nitrogen ambience.

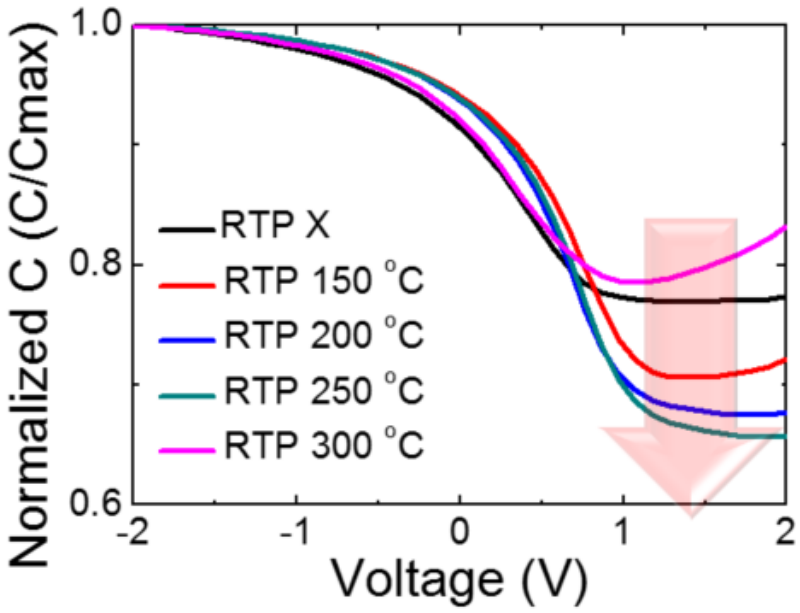

Figure 4.5 The normalized capacitance-voltage curves at 1 MHz frequency.

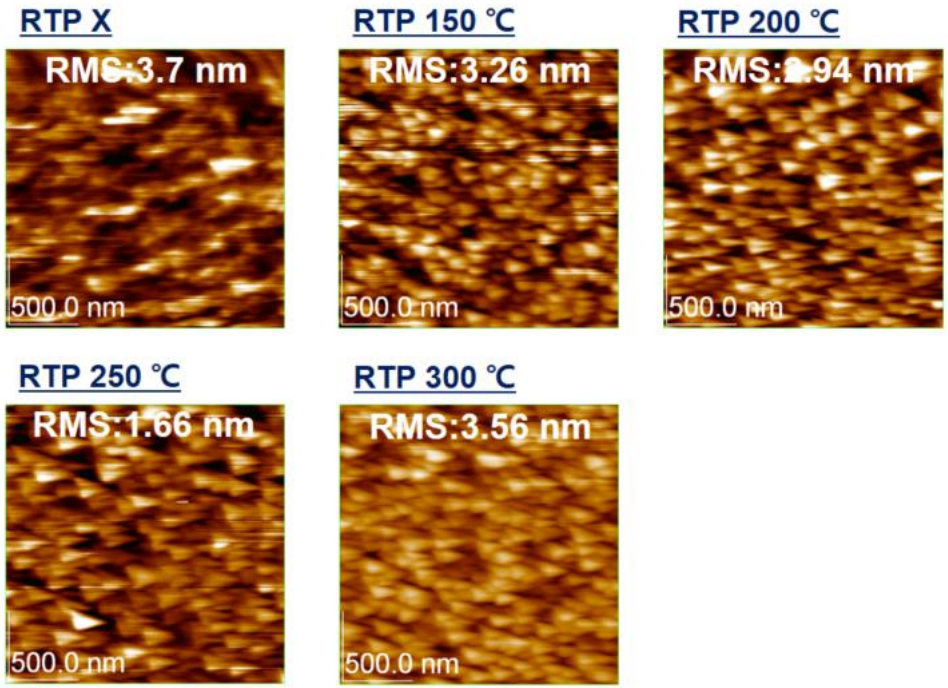

Figure 4.6 AFM analysis results of 10 nm thick Al_2O_3 on GaSb after the post-deposition RTP in a nitrogen ambience at various temperatures for 30 seconds.

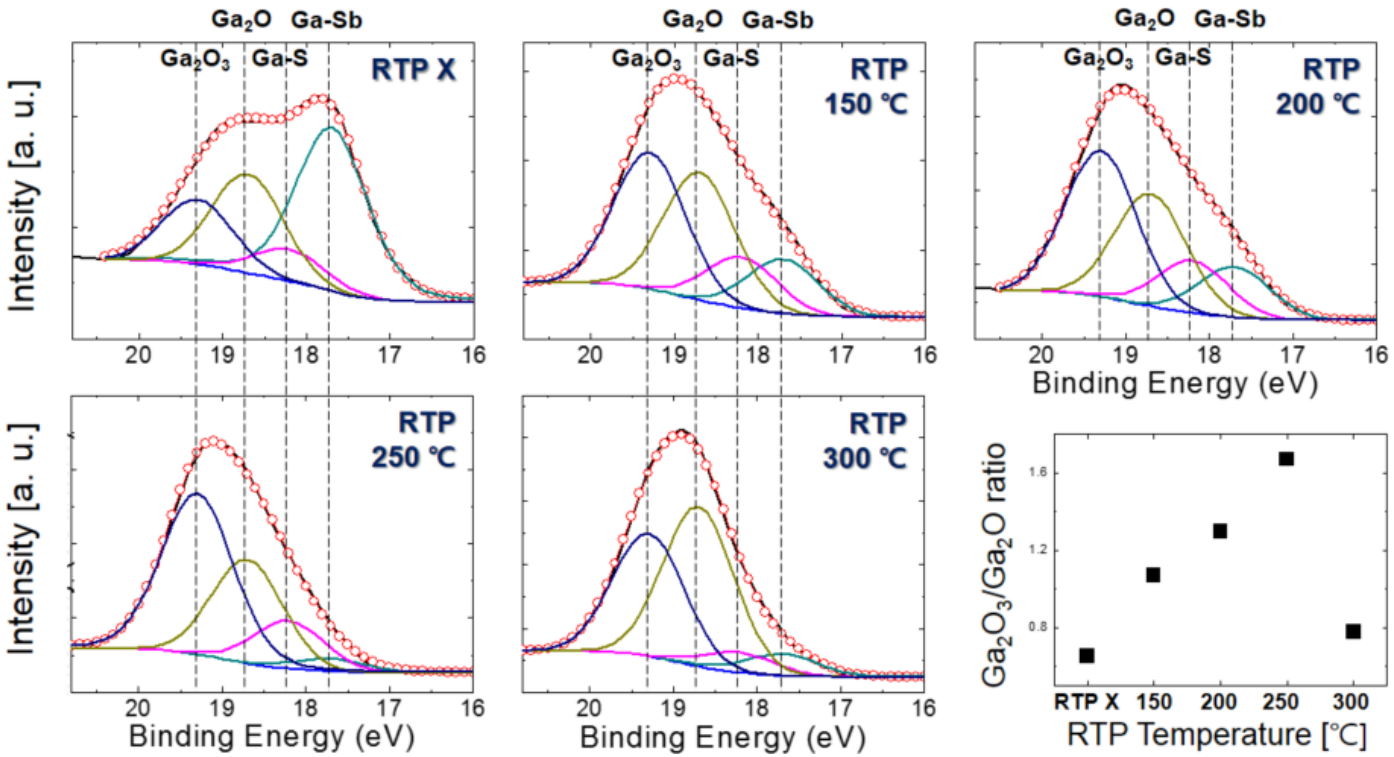

Figure 4.7 XPS spectra of Ga 3d for 2 nm thick Al_2O_3 on GaSb. The right bottom shows the effects of RTP temperature in a nitrogen ambience on the ratio of Ga_2O_3 over Ga_2O.

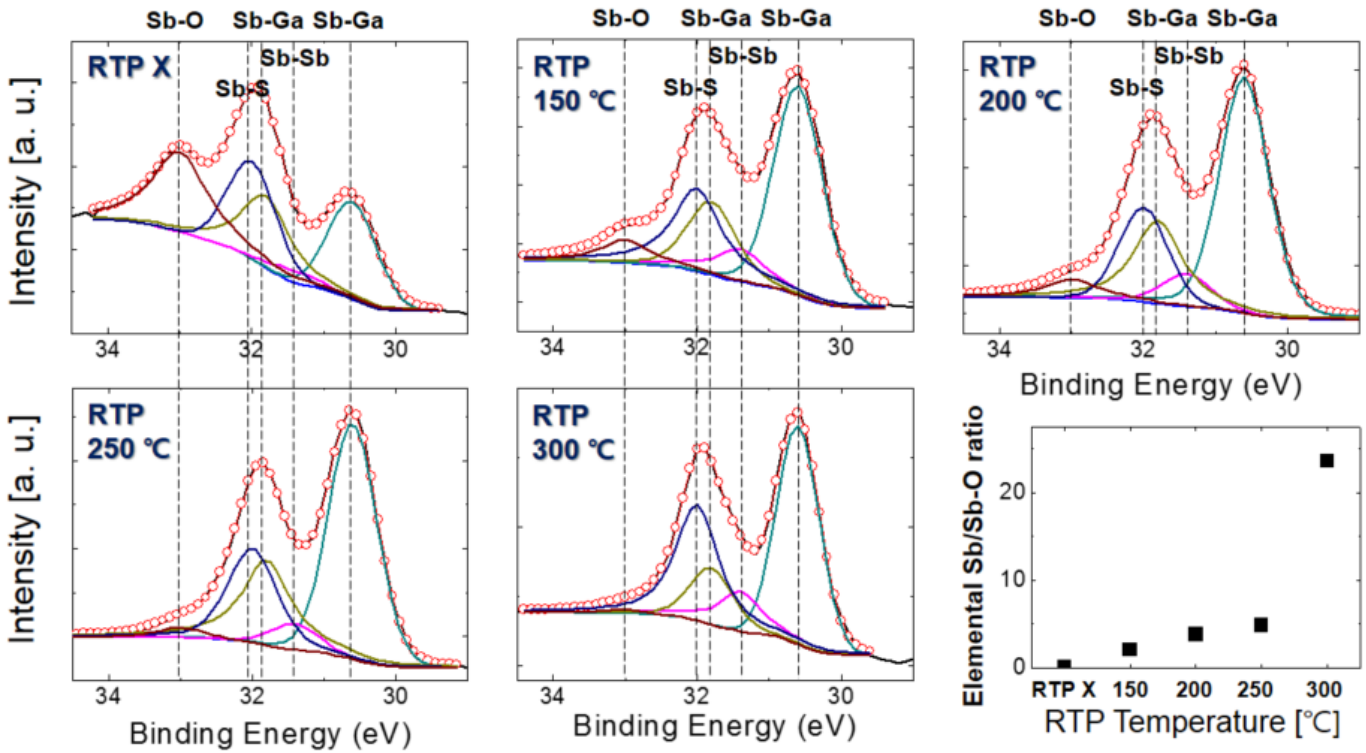

Figure 4.8 XPS spectra of Sb 3d for 2 nm thick Al_2O_3 on GaSb. The right bottom shows the effects of RTP temperature in a nitrogen ambience on the ratio of elemental Sb over Sb-oxide.

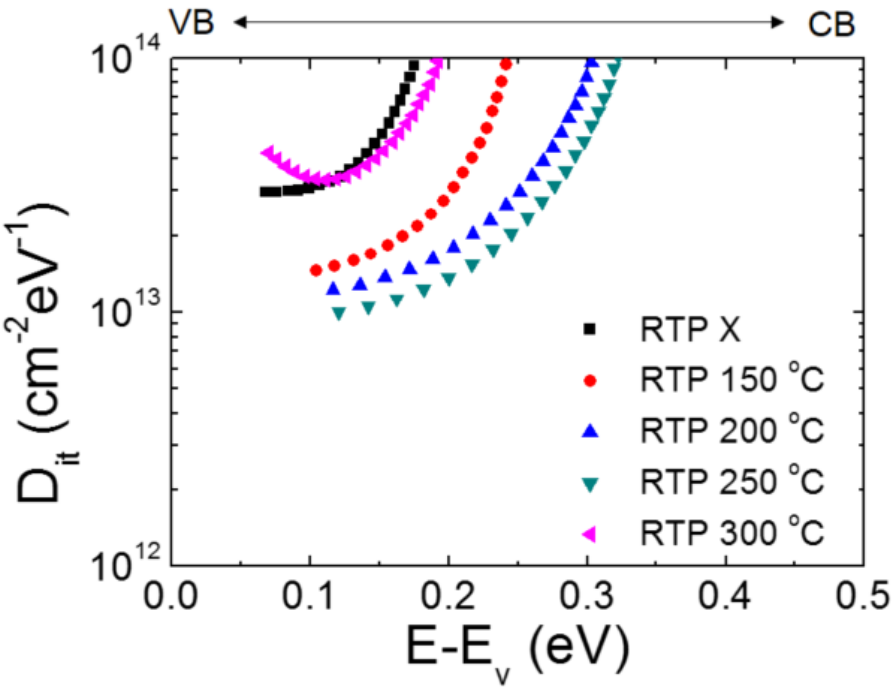

Figure 4.9 Energy distribution of the D_{it} of Al_2O_3/GaSb MOS capacitors.

4.3.2. Post-Deposition Annealing in a Gas Mixture Ambience (5 % H_2 and 95 % N_2)

FGA is known as one of the effective methods to reduce the D_{it} on oxides/Si because dangling bonds are filled up with hydrogen. As mentioned in chapter 4.1, however, there have been many studies on the reduction of Ga_2O_3 to Ga_2O by hydrogen annealing. Therefore it is meaningful to verify which effect is more dominant on oxide/GaSb.

Figure 4.10 shows the normalized the C-V curves of GaSb MOS capacitors with hydrogen annealing at various temperatures in a gas mixture (5 % H_2/95 % N_2) ambience. As the annealing temperature increases, the stretch out in the C-V curves worsened.

In figure 4.11, the energy distribution of the D_{it} of Al_2O_3/GaSb MOS capacitors is shown. From fig 4.11, the D_{it} level after FGA over 250 ℃ increased signicantly. This is a quite interesting result because FGA is usually used to reduce the D_{it} level.

Now XPS spectra of Ga3d for 2 nm thick Al_2O_3 on GaSb are shown in figure 4.12. Also figure 4.12 shows a graph about the effects of hydrogen annealing in a gas mixture (5 % H_2/95 % N_2) ambience on the ratio of Ga_2O_3 over Ga_2O. Compare to the XPS result without FGA, the XPS results with FGA show that the amount of pure Ga_2O_3 decreased while the amount of meta-stable Ga_2O increased as the FGA temperature increased. It indicates that the reduction of Ga_2O_3 to Ga_2O occurred by the FGA. This could be resulted from the reduction effect by the hydrogen annealing.

To figure out the effect of hydrogen annealing, the hydrogen flux was doubled for the next experiment in chapter 4.3.3.

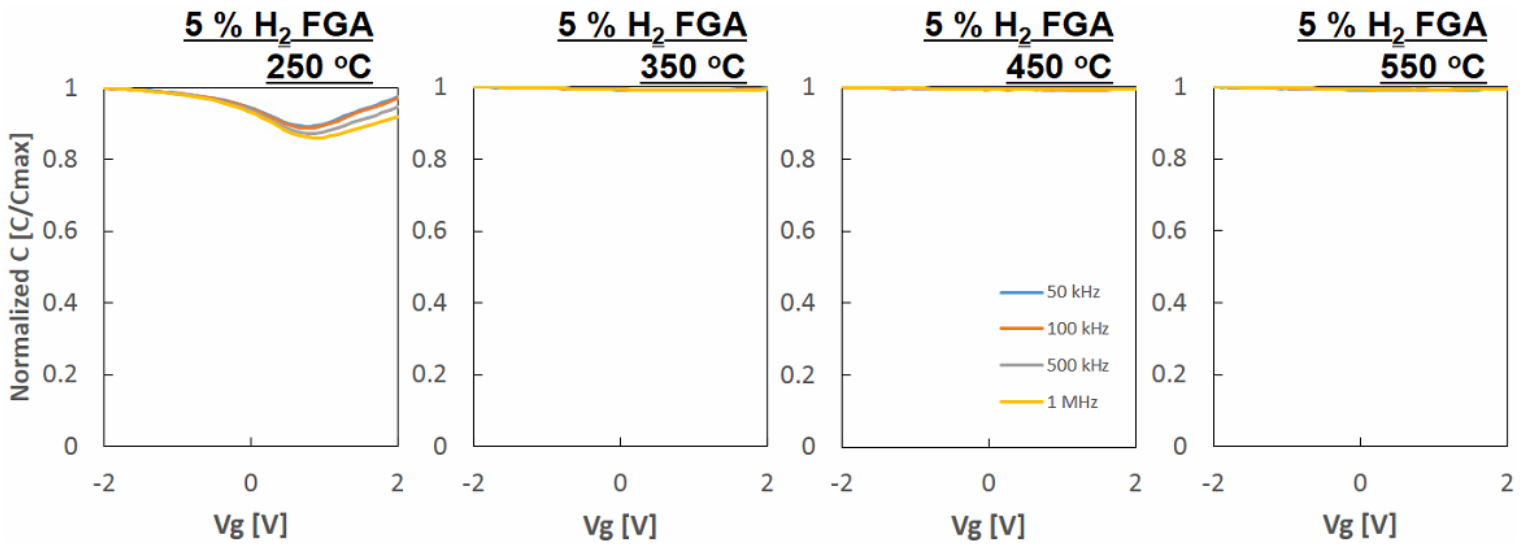

Figure 4.10 Normalized capacitance-voltage curves of GaSb MOS capacitors with the hydrogen annealing at various temperatures in a gas mixture (5 % H_2/95 % N_2) ambience.

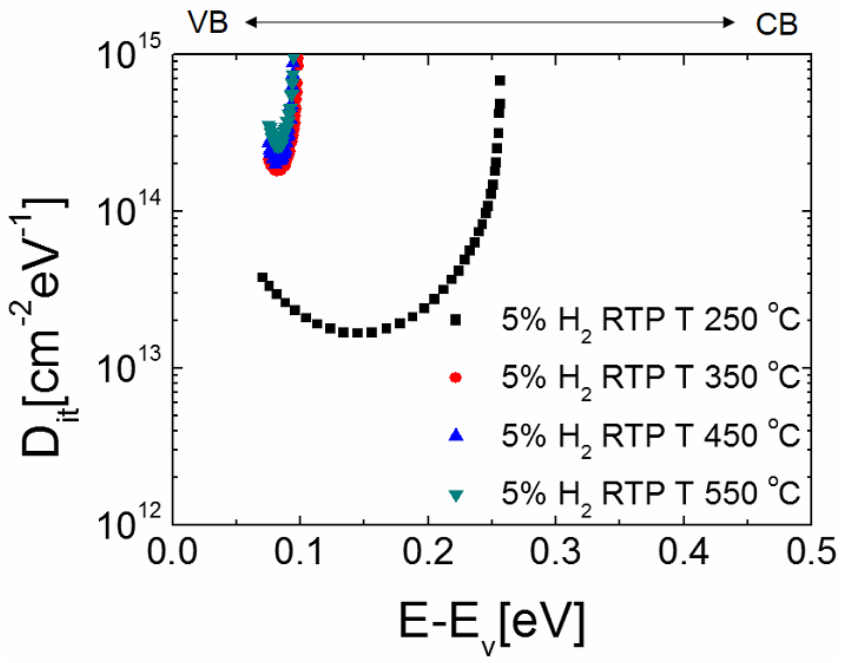

Figure 4.11 Energy distribution of the D_{it} of Al_2O_3/GaSb MOS capacitors.

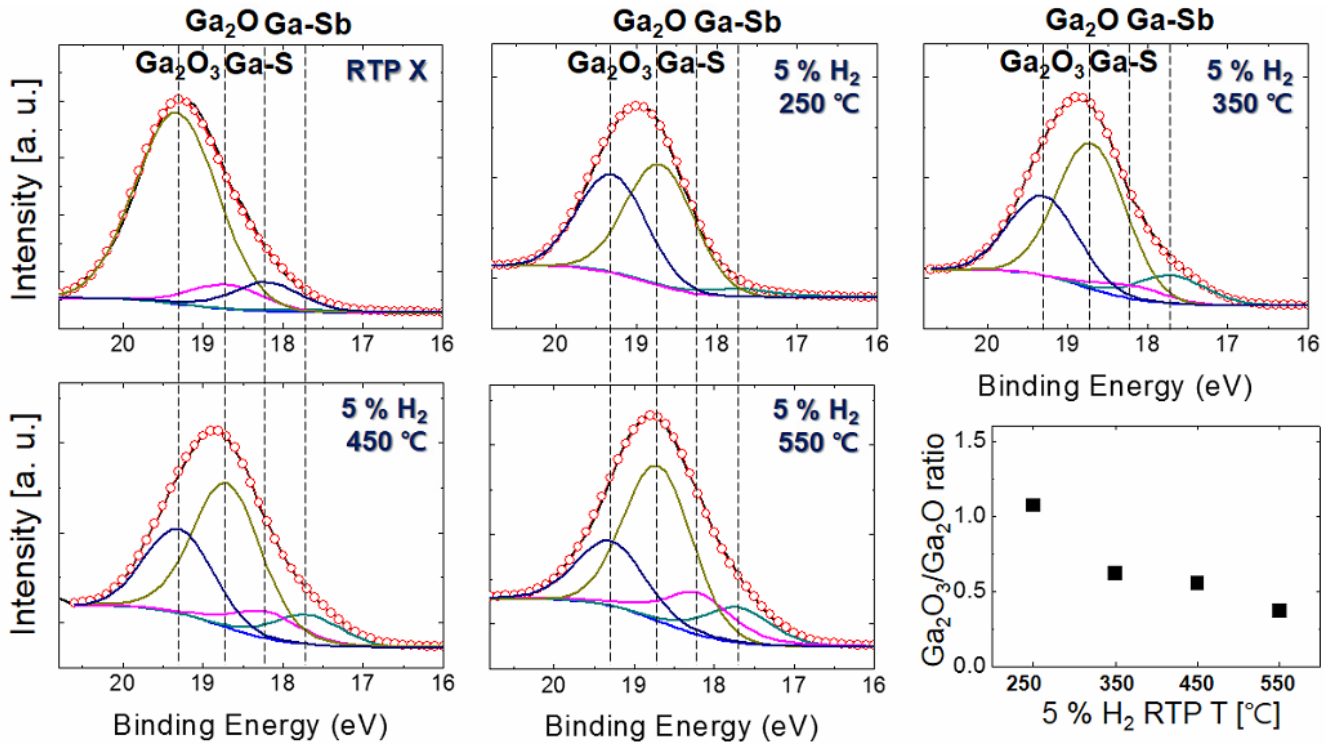

Figure 4.12 XPS spectra of Ga 3d for 2 nm thick Al_2O_3 on GaSb. The right bottom shows the effects of the hydrogen annealing in a gas mixture (5 % H_2/95 % N_2) ambience on the ratio of Ga_2O_3 over Ga_2O.

4.3.3. Post-Deposition Annealing in a Gas Mixture Ambience (10 % H_2 and 90 % N_2)

According to the last chapter, it is necessary to increase the hydrogen flux to verify whether the deterioration of the stretch-out in the C-V curves was resulted from the effects of hydrogen annealing on Al_2O_3/GaSb. Since the reduction of Ga_2O_3 to Ga_2O follows the formula as below,

$$Ga_2O_3 + 2H_2 \rightarrow Ga_2O + 2H_2O \uparrow$$

therefore, the hydrogen flux increased to 10 % to accelerate the reduction of the Ga_2O_3.

Figure4.13 shows the normalized the C-V curves of GaSb MOS capacitors with hydrogen annealing at various temperatures in a gas mixture (10 % H_2/90 % N_2) ambience. Even though the annealing temperature is lower than the one in the previous experiment with the gas mixture (5 % H_2/95 % N_2), the stretch out in the C-V curves became worse with the post-deposition annealing in a gas mixture ambience (10 % H_2/90 % N_2).

Figure4.14 illustrates the energy distribution of the D_{it} of Al_2O_3/GaSb MOS capacitors. The D_{it} level was significantly increased from the sample with 10 % H_2 gas annealing at 200 ℃ to the samples with 10 % H_2 gas annealing at 250, 300, and 350 ℃.

The XPS spectra of Ga3d for 2 nm thick Al_2O_3 on GaSb are shown in figure4.15. As the annealing temperature increased, the ratio of the pure Ga_2O_3 over meta-stable Ga_2O decreased. It is the cause of the stretch-out in the C-V curves. The substrate peak slightly increased as the annealing temperature increased. It indicates that extra reduction of Ga_2O to Ga was occurred as well.

Now, the reduction effects of Ga_2O_3 by hydrogen annealing will be discussed. Figure 4.16 shows the normalized C-V curve of the samples that were annealed at 250 ℃, for 5 minutes but in different hydrogen contents. One was annealed in 5 % H_2, and another was annealed in 10 % H_2. The C-V curve with 10 % H_2 annealing showed more stretched out in the C-V curve, compare to the one with 5 % H_2 annealing. Since the only difference is the flux of H_2, it is clear that H_2 annealing has an impact on the stretch-out in the C-V curves.

Figure 4.17 shows the energy distribution of the D_{it} of GaSb MOS capacitors under different hydrogen flux. The D_{it} level significantly increased by 10 % H_2 annealing compare to the one by 5 % H_2 annealing. Since the only difference is the content of H_2, it is, of course, clear that 5 % H_2 annealing and 10 % H_2 annealing have an effect on the D_{it} level as well.

To verify whether the actual reduction of Ga_2O_3 to Ga_2O occurred, deconvolution of XPS peaks is shown in figure.4.18. The figure.4.18 indicates that the amount of the meta-stable Ga_2O decreased by 10 % H_2 annealing compare to the one by 5 % H_2 annealing. It is obviously because that the increased H_2 flux accelerated the reduction of Ga_2O_3 to Ga_2O described as below.

$Ga_2O_3 + 2H_2 \rightarrow Ga_2O + 2H_2O \uparrow$.

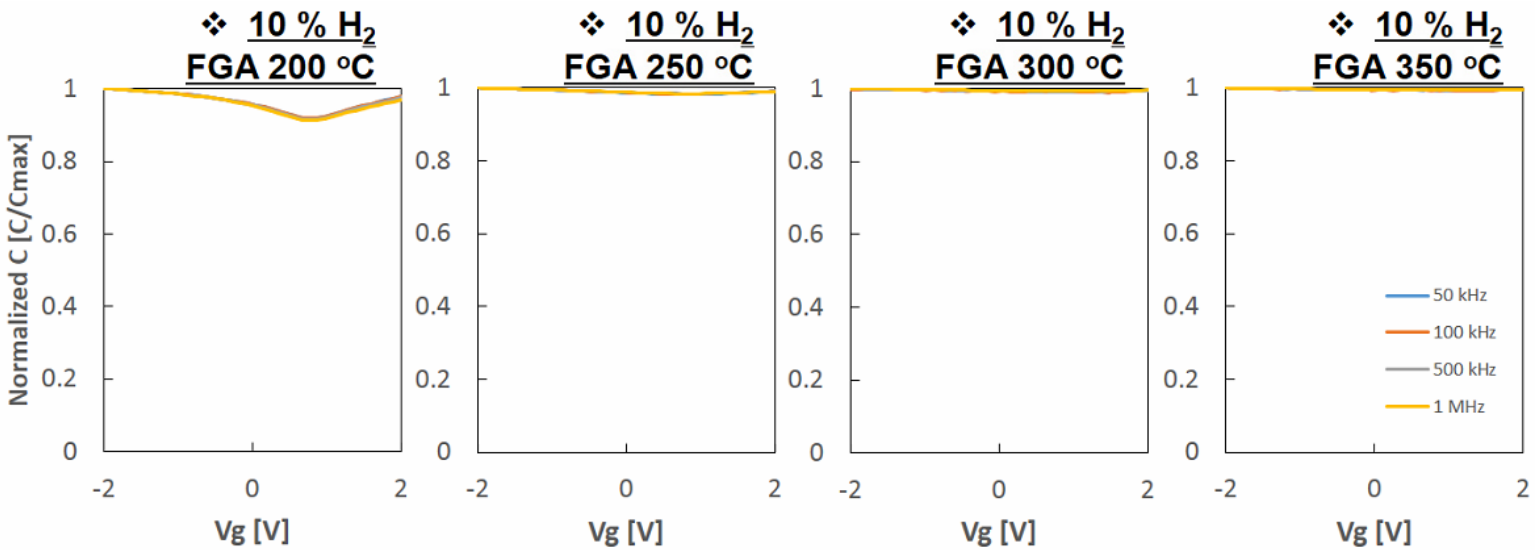

Figure 4.13 Normalized capacitance-voltage curves of GaSb MOS capacitors with the hydrogen annealing at various temperatures in a gas mixture(10 % H_2/90 % N_2) ambience.

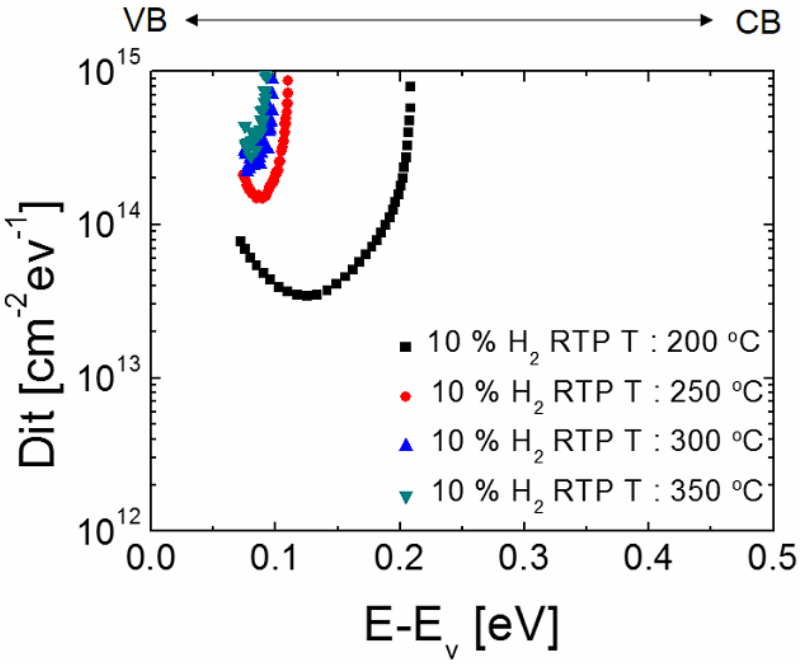

Figure 4.14 Energy distribution of the D_{it} of Al_2O_3/GaSb MOS capacitors.

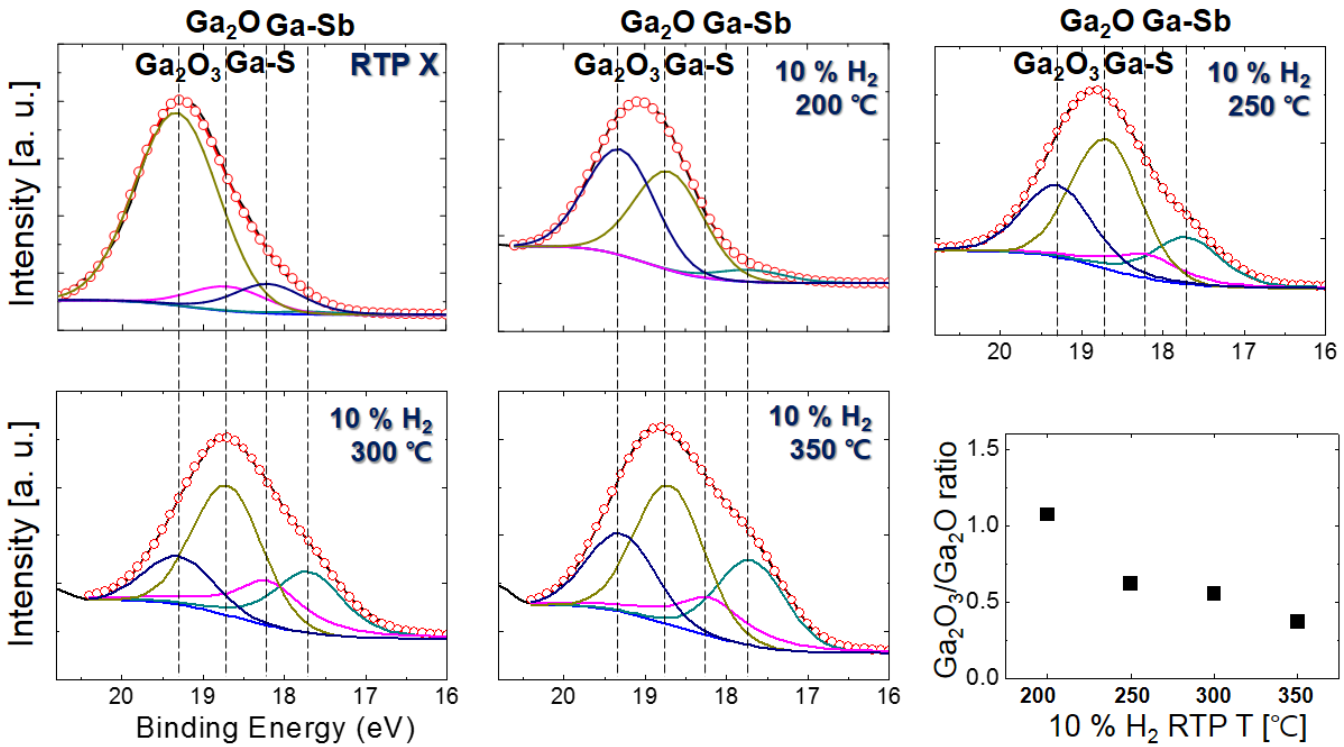

Figure 4.15 XPS spectra of Ga 3d for 2 nm thick Al_2O_3 on GaSb. The right bottom shows the effects of the hydrogen annealing in a gas mixture (10 % H_2/90 % N_2) ambience on the ratio of Ga_2O_3 over Ga_2O.

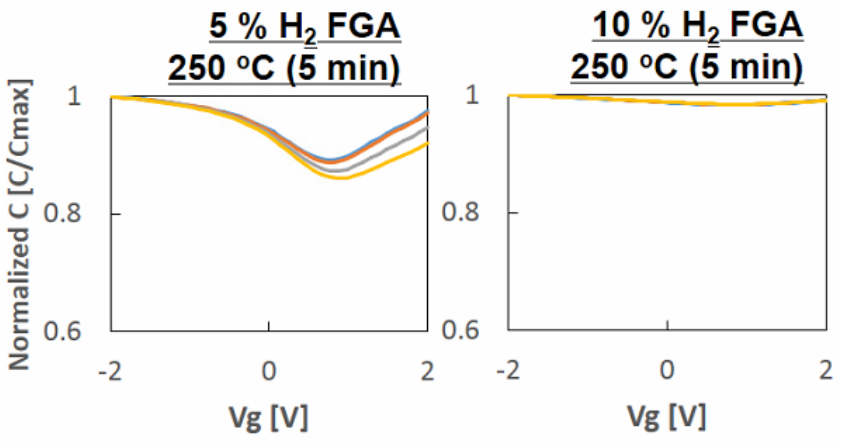

Figure 4.16 Comparison of the normalized capacitance-voltage curves of GaSb MOS capacitors under different hydrogen contents (left: 5 % H_2/95 % N_2, right: 10 % H_2/90 % N_2).

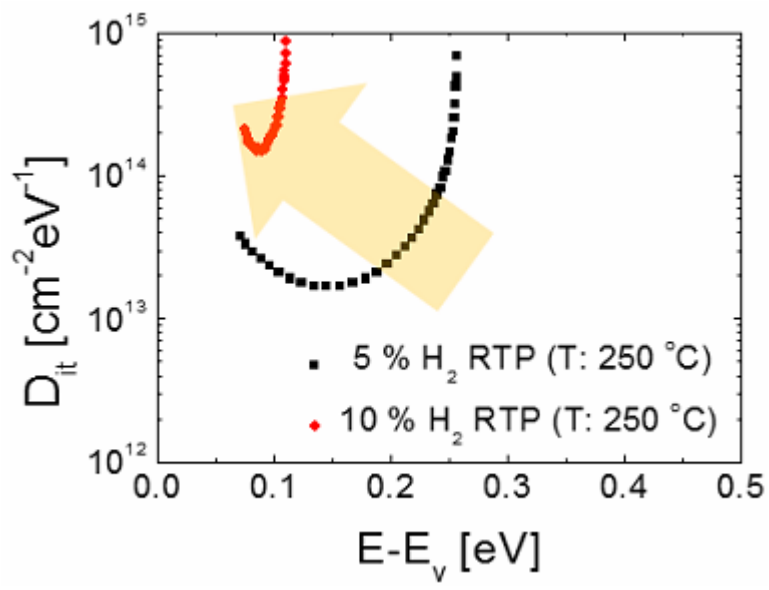

Figure 4.17 Comparison of the energy distribution of the D_{it} of GaSb MOS capacitors under different hydrogen contents.

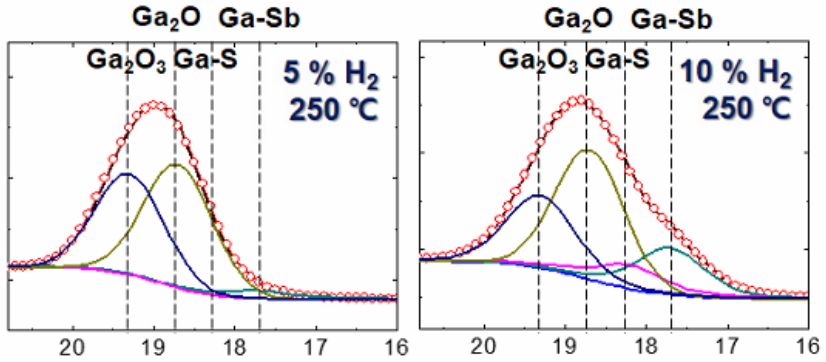

Figure 4.18 Comparison of the XPS spectra of Ga 3d for 2 nm thick Al_2O_3 on GaSb under different hydrogen contents (left: 5 % H_2/95 % N_2, right: 10 % H_2/90 % N_2).

4.4. Summary

Three different experiments had been conducted to see the effects by the post-deposition annealing. The first experiment was the post-deposition annealing in a nitrogen ambience while the second and the third were the H_2 included gas mixture annealing.

The stretch-out in the C-V curves was alleviated with the post-deposition annealing in a nitrogen ambience at 250 ℃. The D_{it} value was decreased by the post-deposition annealing in a nitrogen ambience at 250 ℃. It is resulted from the increased ratio of the pure Ga_2O_3 over meta-stable Ga_2O. The C-V curve, however, deteriorated by the post-deposition annealing in a nitrogen ambience at 300 ℃. The D_{it} value was increased by the post-deposition annealing in a nitrogen ambience at 300 ℃. It is resulted from the decreased ratio of the pure Ga_2O_3 over meta-stable Ga_2O. From the AFM analysis, the surface roughness of 10 nm thick Al_2O_3 on GaSb decreased as the post-deposition annealing temperature increased and increased by the post-deposition annealing at 300 ℃. It indicates that thermal reconstruction of Ga_2O to Ga_2O_3 occurred by the post-deposition annealing at 150, 200, and 250 ℃ and the oxidation of GaSb occurred at 300 ℃. The XPS analysis results are also supporting these phenomena. From the XPS peak deconvolution, the ratio of pure Ga_2O_3 over meta-stable Ga_2O increased as the post-deposition annealing temperature increased and decreased by the post-deposition annealing at 300 ℃.

In the second and third experiments, it showed that the H_2 including mixture gas annealing induced the stretch-out in the C-V curves and increased the D_{it} level of Al_2O_3/GaSb MOS capacitors even though the FGA is famous of one of the effective methods to reduce the D_{it} level in the SiO_2/Si systems.

The gas mixed with 5 % H_2 and 95 % N_2 was used for the second experiment to check the effect of the FGA on Al_2O_3/GaSb MOS capacitors.

The stretch-out in the C-V curves became worse with the 5 % H_2 annealing and almost flat by the 5 % H_2 annealing at 350, 450, 550 ℃. The D_{it} value was increased by the 5 % H_2 annealing as well. It is resulted from the reduction of the pure Ga_2O_3 to meta-stable Ga_2O by H_2 annealing. The XPS analysis results showed that the ratio of the pure Ga_2O_3 over meta-stable Ga_2O decreased as the 5 % H_2 annealing temperature increased.

To verify whether the severe stretch-out in the C-V curves and the increased D_{it} value were actually from the reduction of Ga_2O_3 to Ga_2O by the H_2 annealing, the H_2 flux was doubled for the third experiment.

The gas mixed with 10 % H_2 and 90 % N_2 was used for the second experiment.

The stretch-out in the C-V curves became much worse with the 10 % H_2 annealing compare to the ones with the 5 % H_2 annealing even though the annealing temperature was lower than the one in second experiment. The D_{it} value was increased by the 10 % H_2 annealing. It is resulted from the reduction of the pure Ga_2O_3 to the meta-stable Ga_2O by H_2 annealing. The XPS analysis results also supported this. The ratio of the pure Ga_2O_3 over the meta-stable Ga_2O decreased as the 10 % H_2 annealing temperature increased.

Once compare two samples' results (annealed at 250 ℃ for 5 minutes but in different H_2 contents) from the second and third experiments, it is clear that the H_2 annealing induces the formation of meta-stable Ga_2O. Because of this, the stretch-out in the C-V curves deteriorated and the D_{it} level was increased by the H_2 annealing. In summary, H_2 annealing induces the formation of metastable Ga_2O as below

$$Ga_2O_3 + 2H_2 \rightarrow Ga_2O + 2H_2O \uparrow$$

Therefore, the post-deposition annealing, which can actually improve the stretch-out in the C-V curves and reduce the D_{it} level, should be in a nitrogen ambience.

The post-deposition annealing in an oxygen ambience was also conducted at 200 ℃ but it oxidized GaSb substrate and formed metastable Ga_2O and Sb-oxides. (not shown here but verified by XPS analysis) The C-V curve was also stretched out and the D_{it} was increased by the oxygen annealing.

5. Sulfuric Passivation of GaSb

5.1. Introduction

As discussed in chapter 2, there are enormous studies on chemical cleaning of the native oxide of GaSb. The most effective chemical for it was known as HCl. However, with the most effective chemical, HCl, Sb-oxides cannot be completely eliminated because Sb_2O_5 does not dissolve in diluted HCl. GaSb forms the native oxides rapidly with air exposure. Moreover, Sb-oxides oxidize GaSb to form Ga-oxide and change to elemental Sb. It is natural to think of the re-oxidation of GaSb after HCl cleaning. Of course, the Sb-oxide, which is formed by the re-oxidation of GaSb, oxidizes GaSb again in an ALD chamber. Therefore it is essential to adopt passivation of GaSb surface right after the cleaning to prevent the further oxidation of GaSb for ex-situ deposition.

Sulfuric passivation was chosen for it. It is quite simple to adopt the sulfuric passivation because the only thing to do is just dipping GaSb in sulfuric solution. After the sulfur treatment, the surfaces of GaSb wafers are passivated by forming Ga-S and Sb-S bonds, which will improve the electrical properties of the MOSCAPs.

To optimize the sulfuric passivation conditions, GaSb wafers were immersed in 5 % $(NH_4)_2S$ for various times.

5.2. Experimental Procedures

2 inch p-type undoped GaSb wafers with a carrier concentration of 2 x 10^{17} cm^{-3} were used for fabricating GaSb MOS capacitors. GaSb wafers were diced by dicing saw into ~1 cm length. After dicing the GaSb wafers, degreasing was performed by dipping them in acetone, ethanol, isopropyl alcohol (IPA) for 3 minutes each. The GaSb pieces were, then, dipped in diluted HCl (9 %) for 1 minute. Prior to depositing gate oxide, the GaSb pieces were immersed in $(NH_4)_2S$ (5 %) for various times (1, 5, 10, and 15 minutes). The GaSb pieces were then transferred to the ALD chamber within several minutes.

To fabricate GaSb MOS capacitors, Al_2O_3 was selected as gate oxide. 10 nm thick Al_2O_3 was deposited by ALD. The deposition temperature was set at 150 ℃. Trimethylaluminium ($Al(CH_3)_3$, TMA) and de-ionized water were used as a Al source and an oxidant respectively. The thickness of oxides was measured by a spectroscopic ellipsometry (SE).

For the metal electrode of the MOS capacitors, Platinum was deposited by electron beam evaporation through shadow mask with an area of 6.6 x 10^4 μm^2 placed on each sample to form pattered gate electrodes. Indium paste was applied as the backside contacts.

Figure 5.1 shows the experimental process conditions for the sulfuric passivation.

For the C-V measurements, Pt gate electrodes and In backside contact of GaSb MOS capacitors were connected with LCR meter (HP4284 Impedance analyzer). Measurement temperature was kept at room temperature.

The C-V frequency dispersions were evaluated using 4 different frequencies from 50 kHz to 1 MHz. The Vg sweep during the measurements was ranged from 2 V to -2 V.

The interface states density (D_{it}) in GaSb band gap were extracted by the Terman method which can calculate the D_{it} from the stretch-out in the C-V curves compare to an ideal the C-V curve (no D_{it}).

Surface chemical bonding states of the samples were characterized by x-ray photoelectron spectroscopy (XPS) with monochromatic Al K-α source (hv=14876.7 e/V) For the XPS analysis, 2 nm of gate oxide was deposited on GaSb wafers but the metal contacts were not deposited on the GaSb wafers. Ga 3d and Sb 4d peaks were mainly discussed with the electrical results.

For the composition depth profiles of the oxide deposited GaSb samples, Auger electron spectroscopy (AES) was used. 10 nm thick oxide was deposited on GaSb wafers but the metal contacts were not deposited on the GaSb wafers for AES analysis.

Atomic force microscope (AFM) analysis was performed to evaluate the roughness of the samples. For this, oxide was not deposited on GaSb wafers and also the metal contacts were not deposited on the GaSb wafers.

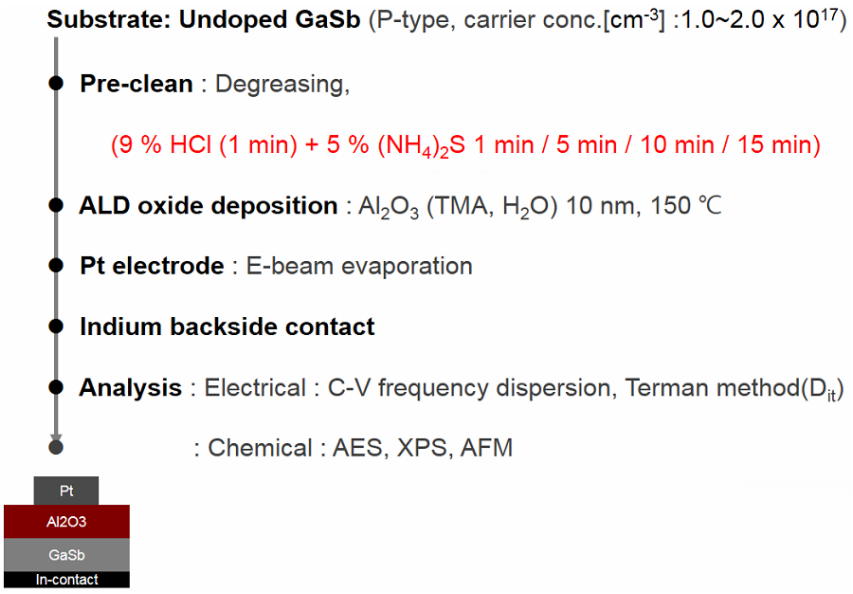

Figure 5.1 The experimental process conditions for MOS capacitors fabrication. (to see the effects of sulfuric passivation on Al_2O_3/GaSb.)

5.3. Results and Discussions

Figure 5.2 shows the normalized capacitance-voltage curves of GaSb MOS capacitors with immersing in $(NH_4)_2S$ solution for various times (1, 5, 10, and 15 minutes). The stretch out in the C-V curve was alleviated by immersing in a sulfuric solution for 1 and 5 minutes but then became worse by immersing in a sulfuric solution for 10 and 15 minutes. The C-V curve was expected to be better with longer dipping time because $(NH_4)_2S$ solution can also eliminate the native oxide as follow [82].

$$(NH_4)_2S + H_2O \rightarrow NH_4OH + NH_4SH$$

$$SbO_x + NH_4SH \rightarrow SbS_y + NH_4OH$$

$$GaO_x + NH_4SH \rightarrow GaS_y + NH_4OH$$

To figure out the deterioration of the C-V curve with immersion in a sulfuric solution for 10 and 15 minutes, AFM analysis was conducted. Figure 5.3 illustrates AFM analysis results of GaSb after immersing in $(NH_4)_2S$ solution for various times. The surface roughness of GaSb elevated as the immersion time increased. The increased roughness can be problematic because it forms high structural disorder which indeed generates structural defects. The reason why the surface roughness was increased was because $(NH_4)_2S$ etched GaSb as below [82].

$$(NH_4)_2S + H_2O \rightarrow NH_4OH + NH_4SH$$

$$GaSb + NH_4OH \rightarrow GaO_x + SbO_y + NH_4 + H_2$$

As shown above, $(NH_4)_2S$ makes NH_4OH once it meets H_2O. This NH_4OH actually reacts with GaSb and forms Ga-oxide and Sb-oxide. And these native oxides react with NH_4SH and change to Sb-S and Ga-S as mentioned above. Thus, it remains high surface roughness with fewer native oxides.

Figure 5.4 illustrates the AES analysis results of 10 nm thick Al_2O_3 on GaSb after immersing in $(NH_4)_2S$ solution for various times. The interface layer is lengthened when the immersion time is increased to 10 and 15 minutes from 5 minutes. Also Al and O diffused towards the substrate deeply with the immersion in the sulfuric solution for 10 and 15 minutes. It supports the discussion that were dealt above. The inter layer is known for having defects from structural disorder. Therefore it is clear that longer immersion time will aggravate the C-V curves.

Figure 5.5 demonstrates the XPS spectra of Ga 3d for 2 nm thick Al_2O_3 on GaSb. The right bottom graph shows the effects of sulfuric passivation by immersing the samples in $(NH_4)_2S$ solution for various times on the ratio of pure Ga_2O_3 over meta stable Ga_2O. The ratio of the pure Ga_2O_3 over the meta-stable Ga_2O was highest with immersing the samples in the sulfuric solution for 5 minutes and decreased as the immersion time increased. Overall, the amount of Ga-oxides was decreased with sulfuric passivation. It indicates that Ga-oxides can be eliminated by sulfuric passivation.

The energy distribution of the D_{it} of Al_2O_3/GaSb MOS capacitors is shown in figure 5.6. The D_{it} level decreased by immersing the samples in a sulfuric solution for 5 minutes and increased as the immersion time increased.

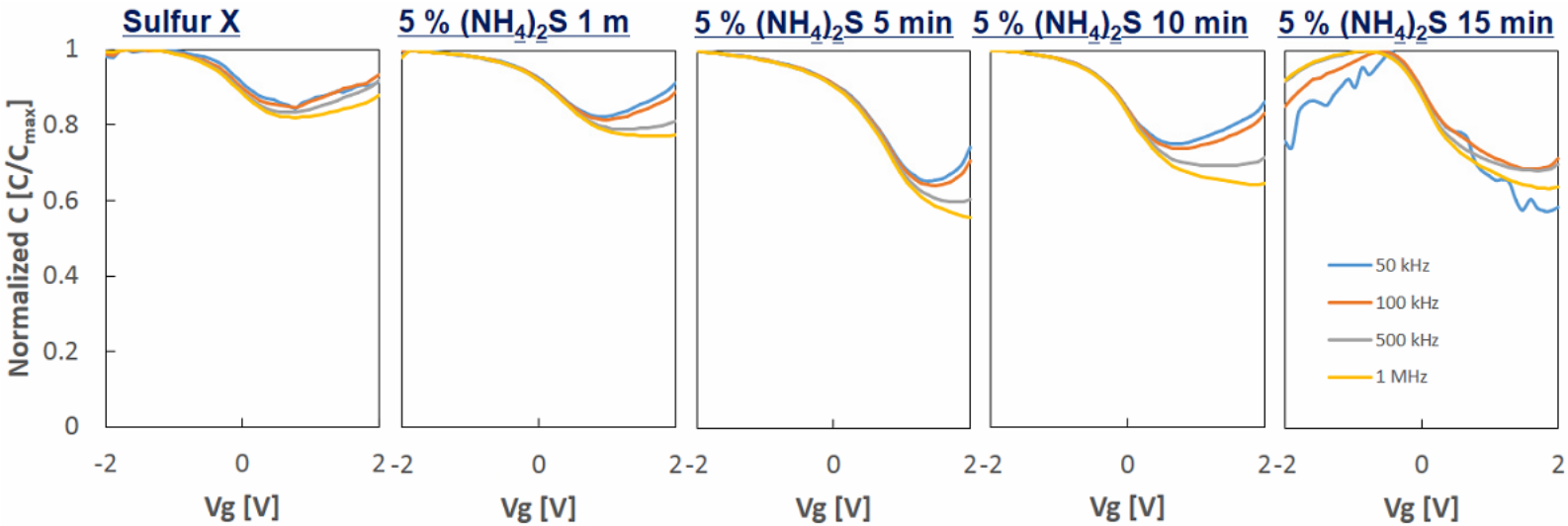

Figure 5.2 Normalized capacitance-voltage curves of GaSb MOS capacitors with immersing the samples in $(NH_4)_2S$ solution for various times.

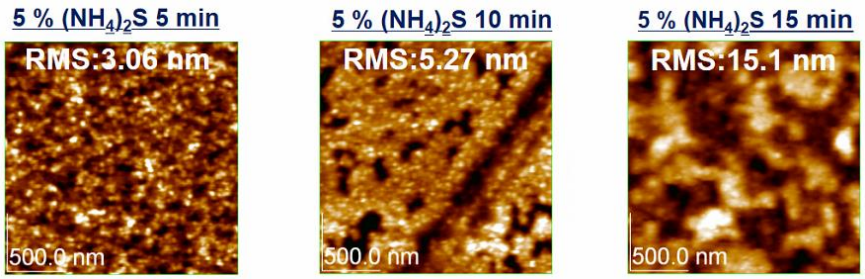

Figure 5.3 AFM analysis results of GaSb after immersing the samples in $(NH_4)_2S$ solution for various times.

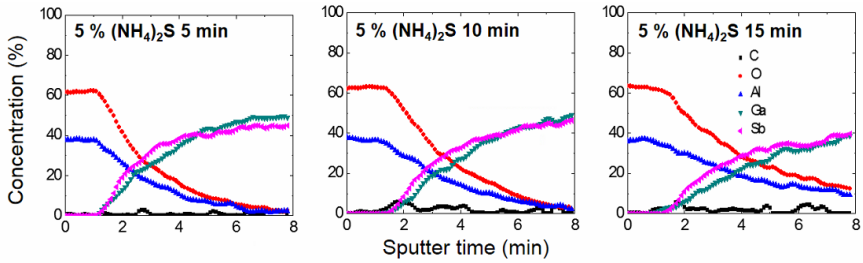

Figure 5.4 AES analysis results of 10 nm thick Al_2O_3 on GaSb after immersing the samples in $(NH_4)_2S$ solution for various times.

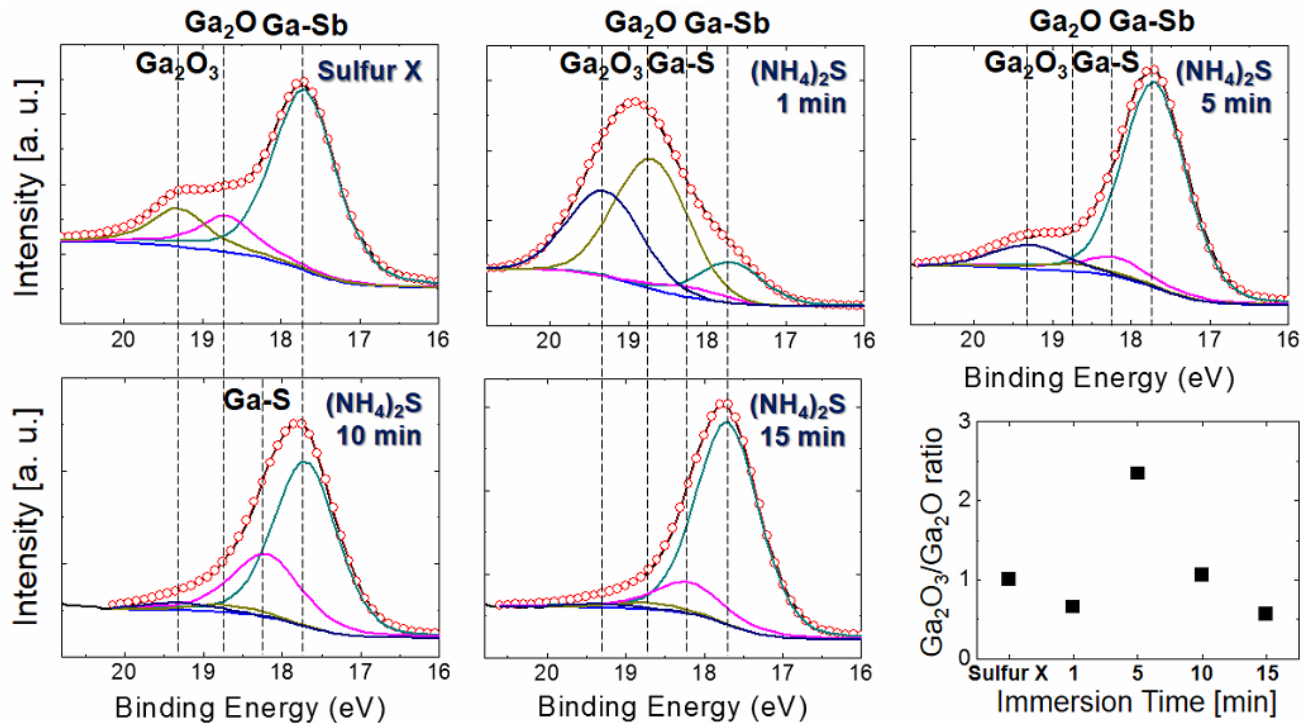

Figure 5.5 XPS spectra of Ga 3d for 2 nm thick Al_2O_3 on GaSb. The right bottom shows the effects of sulfuric passivation by immersing the samples in $(NH_4)_2S$ solution for various times on the ratio of Ga_2O_3 over Ga_2O.

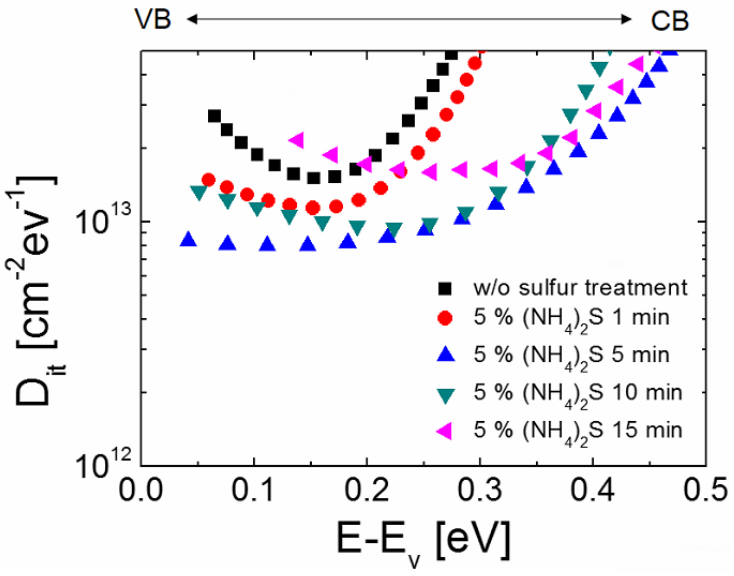

Figure 5.6 Energy distribution of the D_{it} of Al_2O_3/GaSb MOS capacitors.

5.4. Summary

When GaSb moves to the chamber after cleaning GaSb surface, GaSb forms the native oxides quickly due to the fast oxidation of GaSb with air exposure. Especially Sb-oxide oxidizes GaSb and continuous oxidation of GaSb occurs. Even with the most effective chemical, HCl, Sb-oxide cannot be eliminated completely because Sb_2O_5 does not dissolve in dilute HCl. Thus, it is essential to adopt surface passivation after cleaning to prevent further oxidation for ex-situ deposition.

GaSb wafers were dipped in $(NH_4)_2S$ for various times (1, 5, 10, and 15 minutes). The stretch-out in the C-V curves was alleviated and the D_{it} level was reduced by immersing GaSb in the sulfuric solution for 5 minutes. It was resulted from the increased ratio of pure Ga_2O_3 over meta-stable Ga_2O, which was proven by the XPS results. However, once the immersion time increased over 5 minutes, the stretch-out in the C-V curves became worse. The AFM results showed that the surface roughness increased as the immersion time increased. This was because NH_4OH, which was made from $(NH_4)_2S$ and water, etched GaSb. The Ga-oxide and Sb-oxide, which were made by NH_4OH, reacted with NH_4SH and changed to Ga-S and Sb-S respectively. Because of this, in the XPS results, Ga-oxide peaks decreased by immersing the samples in the sulfuric solution.

6. Pre-Deposition Rapid Thermal Annealing of GaSb in a Nitrogen Ambient

6.1. Introduction

As mentioned in chapter 5, the most effective chemical, HCl, cannot eliminate all of the native oxide because Sb_2O_5 does not dissolve in HCl. The remaining Sb-oxide is problematic since it oxidizes GaSb continuously. Thus, it is needed to adopt extra cleaning procedure to get rid of Sb-oxide after HCl cleaning.

Figure.6.1 shows the schematic of surface reactions for heating the GaSb wafers in an ultra high vacuum system ($<10^{-9}$ Torr). In a relatively low temperature region, the formation of native oxides is accelerated. Once increasing the temperature, Sb-oxide and elemental Sb are thermally desorbed and diffused out between oxide/GaSb interface and surface.

To adopt this desorption mechanism for eliminating the native oxides, RTP was implemented because it is a process that increases and decreases the process temperature quickly. The RTP was used before depositing gate oxide. This pre-deposition RTP for improving the electrical properties of Al_2O_3/GaSb was firstly introduced by this author. Since RTP machine's base pressure (~ 7 mTorr) is not the same as the one ($<10^{-9}$ Torr) in a UHV system, nitrogen flux of 200 sccm was used for the pre-deposition RTP.

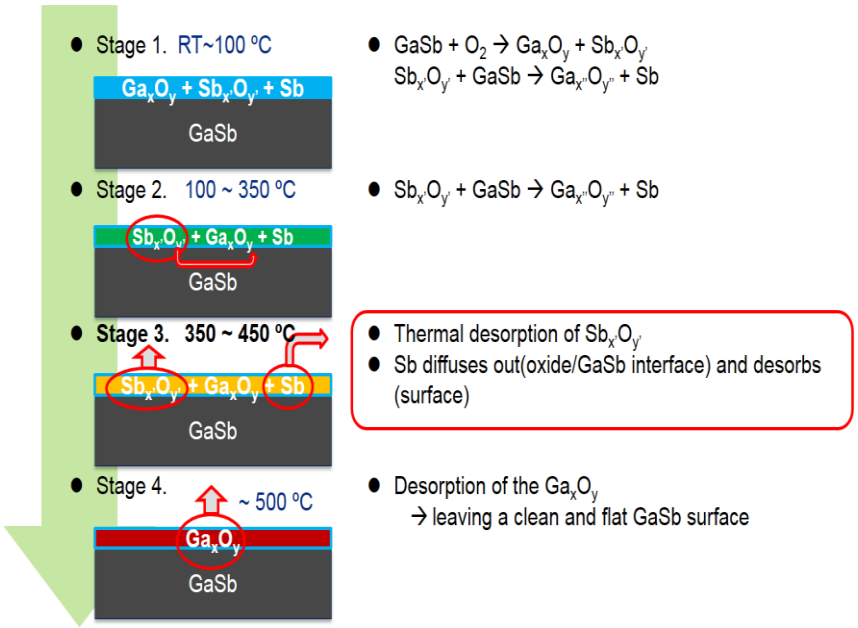

Figure 6.1 The schematic of surface reactions for the heating the GaSb wafers in a ultra high vacuum system (<10^{-9} Torr). The informations are from these two papers [68, 100].

6.2. Experimental Procedures

2 inch p-type undoped GaSb wafers with a carrier concentration of 2 x 10^{17} cm^{-3} were used for fabricating GaSb MOS capacitors. GaSb wafers were diced by dicing saw into ~1 cm length. After dicing the GaSb wafers, degreasing was performed by dipping them in acetone, ethanol, isopropyl alcohol (IPA) for 3 minutes each. Prior to pre-deposition RTP, the GaSb pieces were dipped in diluted HCl (9 %) and $(NH_4)_2S$ (5 %) for 1 and 5 minutes each. The GaSb pieces were then transferred to the RTP chamber for the pre-deposition RTP. The base pressure of the pre-deposition RTP was ~ 7 mTorr and the process pressure was ~ 100 mTorr with nitrogen gas flux of 200 sccm. The process temperatures varied from 500 to 575 ℃. The process time was 30 seconds. Prior to depositing gate oxide, the GaSb pieces were immersed in 5 % $(NH_4)_2S$ for 1 minute. The GaSb pieces were then transferred to the ALD chamber within several minutes.

To fabricate GaSb MOS capacitors, gate oxide was selected as Al_2O_3. 10 nm thick Al_2O_3 was deposited by ALD. The deposition temperature was set at 150 ℃. Trimethylaluminium ($Al(CH_3)_3$, TMA) and de-ionized water were used as a Al source and an oxidant respectively. The thickness of oxides were measured by a spectroscopic ellipsometry.

For the metal electrode of the MOS capacitors, Platinum was deposited by electron beam evaporation through shadow mask with an area of 6.6 x 10^4 μm^2 placed on each sample to form pattered gate electrodes. Indium paste was applied as the backside contacts.

Figure. 6.2 shows the experimental process conditions for the pre-deposition RTP in a nitrogen ambience.

For the C-V measurements, Pt gate electrodes and In backside contact of GaSb MOS capacitors were connected with LCR meter (HP4284 Impedance analyzer). Measurement temperature was kept at room temperature.

The C-V frequency dispersions were evaluated using 4 different frequencies from 50 kHz to 1 MHz. The Vg sweep during the measurements was ranged from 2 V to -2 V.

The interface states density (D_{it}) in GaSb band gap were extracted by the Terman method which can calculate the D_{it} from the stretch-out in the C-V curves by comparing it to an ideal the C-V curve (no D_{it}).

Surface chemical bonding states of the samples were characterized by x-ray photoelectron spectroscopy (XPS) with monochromatic Al K-α source (hv=14876.7 e/V) For the XPS analysis, 2 nm of gate oxide was deposited on GaSb wafers but the metal contacts were not deposited on the GaSb wafers. Ga 3d and Sb 4d peaks were mainly discussed with the electrical results.

For the composition depth profiles of the oxide deposited GaSb samples, Auger electron spectroscopy (AES) was used. 10 nm thick oxide was deposited on GaSb wafers but the metal contacts were not deposited on the GaSb wafers for AES analysis.

Atomic force microscope (AFM) analysis was performed to evaluate the roughness of the samples. For this, 10 nm thick oxide was deposited on GaSb wafers but the metal contacts were not deposited on the GaSb wafers.

For transmittance electron microscope (TEM) analysis, 10 nm thick oxide was deposited on GaSb wafers. On top of that, about 60 nm thick Pt was deposited to prevent carbon re-deposition while fabricating TEM samples by focused ion beam (FIB).

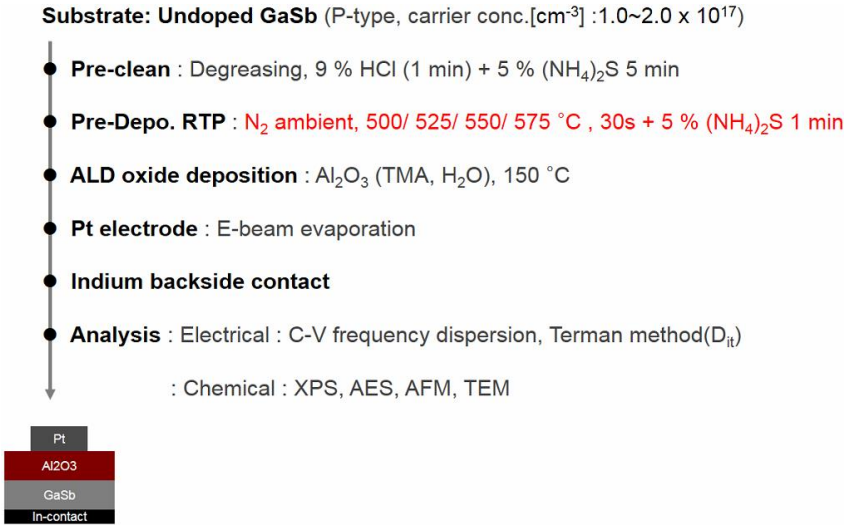

Figure 6.2 The experimental process conditions for MOS capacitors fabrication. (to see the effects of pre-deposition RTP on GaSb.)

6.3. Results and Discussions

Figure 6.3 shows the normalized capacitance-voltage curves of GaSb MOS capacitors with the pre-deposition RTP at various RTP temperatures in a nitrogen ambience. It shows a striking improvement in the stretch-out in the C-V curves with the pre-deposition RTP at 550 and 575 ℃. However, the stretch-out in the C-V curves with the pre-deposition RTP at 500 and 525 ℃ became worse than the one without the pre-deposition RTP.

Figure 6.4 demonstrates the C-V hysteresis of Al_2O_3/GaSb MOS capacitors with and without the pre-deposition RTP. Mostly, trapping and emission through oxide bulk traps give a rise to the C-V hysteresis. The C-V hysteresis of the sample without the pre-deposition RTP and with the pre-deposition RTP at 575 ℃ was 0.94 V and 0.7 V respectively. The C-V hysteresis decreased slightly. It means that oxide bulk traps slightly reduced by the pre-deposition RTP at 575 ℃. Therefore, the improvement of the C-V curves were resulted from the decreased D_{it} level than from the decreased density of oxide bulk traps.

The energy distributions of the D_{it} of Al_2O_3/GaSb MOS capacitors are shown in figure 6.5. The D_{it} level was successfully reduced by the pre-deposition RTP at 550 and 575 ℃. The lowest D_{it} value is 1.05×10^{12} $cm^{-2}ev^{-1}$ (at $E\text{-}E_v = 0.004$) with the pre-deposition RTP at 575 ℃. This is the lowest D_{it} value among other D_{it} values in sulfur treated GaSb MOS capacitors in literature.

Figure 6.6 illustrates the XPS spectra of Ga 3d for 2 nm thick Al_2O_3 on GaSb. The graph in figure 6.6 shows the effects of the pre-deposition RTP temperature in a nitrogen ambience on the ratio of Ga_2O_3 over Ga_2O. The ratio of pure Ga_2O_3 over meta-stable Ga_2O decreased by the pre-deposition RTP at 500 and 525 ℃. It indicates that the oxidation of GaSb was accelerated by the pre-deposition RTP at 500 and 525 ℃. After this, the ratio of pure Ga_2O_3 over meta-stable

Ga_2O increased as the pre-deposition RTP temperature increased. Since the pure Ga_2O_3 is known to make a low-defect interface with GaSb, the increased amount of Ga_2O_3 can actually improve the electrical properties. The increase of the ratio of Ga_2O_3 over meta-stable Ga_2O was resulted from the broken Sb-O bonds. The Sb-O bonds were broken by thermal energy. The broken Sb-O bonds leaved liberated Sb. This liberated Sb desorbed out as elemental Sb since there was no extra Sb flux. Finally, it leaved an oxygen rich environment. This oxygen rich environment generated the Ga_2O_3 layer. The series of the reactions to generate the Ga_2O_3 layer were also discussed in literature [71].

In figure 6.7, the AFM analysis results of 10 nm thick Al_2O_3 on GaSb after pre-deposition RTP in a nitrogen ambience at various temperatures for 30 seconds. The surface roughness of 10 nm thick Al_2O_3 on GaSb increased after the pre-deposition RTP in a nitrogen ambience. The surface roughness then decreased as the pre-deposition RTP temperature increased. It is resulted from the reconstruction of metastable Ga_2O to pure Ga_2O_3 and the elimination of Sb species. The increased surface roughness is problematic for the C-V curves and the D_{it} value since structural disorder increases as the surface roughness increases and makes more structural defects such as dangling bonds.

Figure 6.8 demonstrated the AES analysis results of 10 nm thick Al_2O_3 on GaSb after pre-deposition RTP in a nitrogen ambience at various temperatures for 30 seconds. The interlayer between Al_2O_3 and GaSb was lengthened by the pre-deposition RTP at 500 ℃ and shortened by the pre-deposition RTP 575 ℃. The Al and O also diffused towards the substrate deeply. It indicates that the oxidation of GaSb occurred by the pre-deposition RTP at 500 ℃.

Finally, the TEM images are illustrated in figure 6.9. It also supports that the oxidation of GaSb occurred by the pre-deposition RTP at 500 ℃.

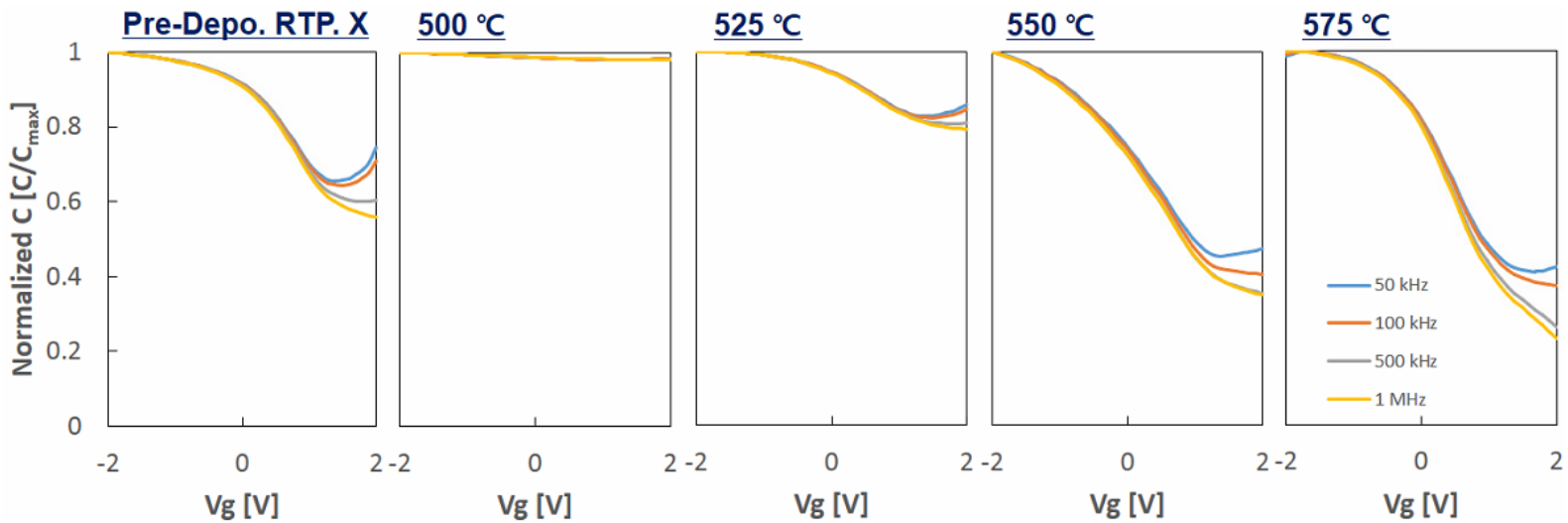

Figure 6.3 Normalized capacitance-voltage curves of GaSb MOS capacitors with the pre-deposition RTP at various RTP temperatures in a nitrogen ambience.

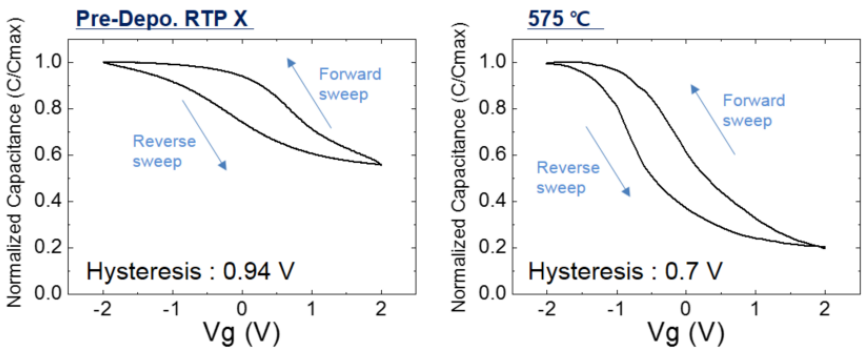

Figure 6.4 The C-V hysteresis of Al_2O_3 on GaSb substrates. (left: without pre-deposition RTP, right: with pre-deposition RTP at 575 ℃)

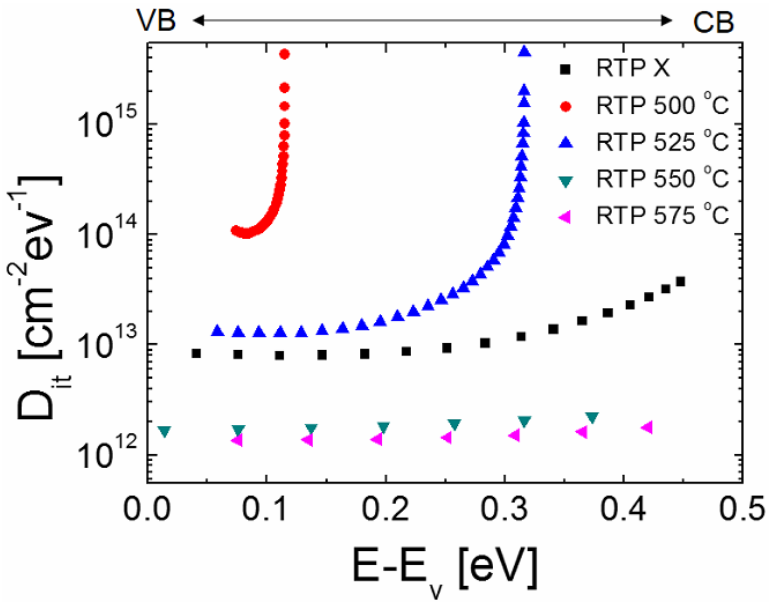

Figure 6.5 Energy distribution of the D_{it} of Al_2O_3/GaSb MOS capacitors.

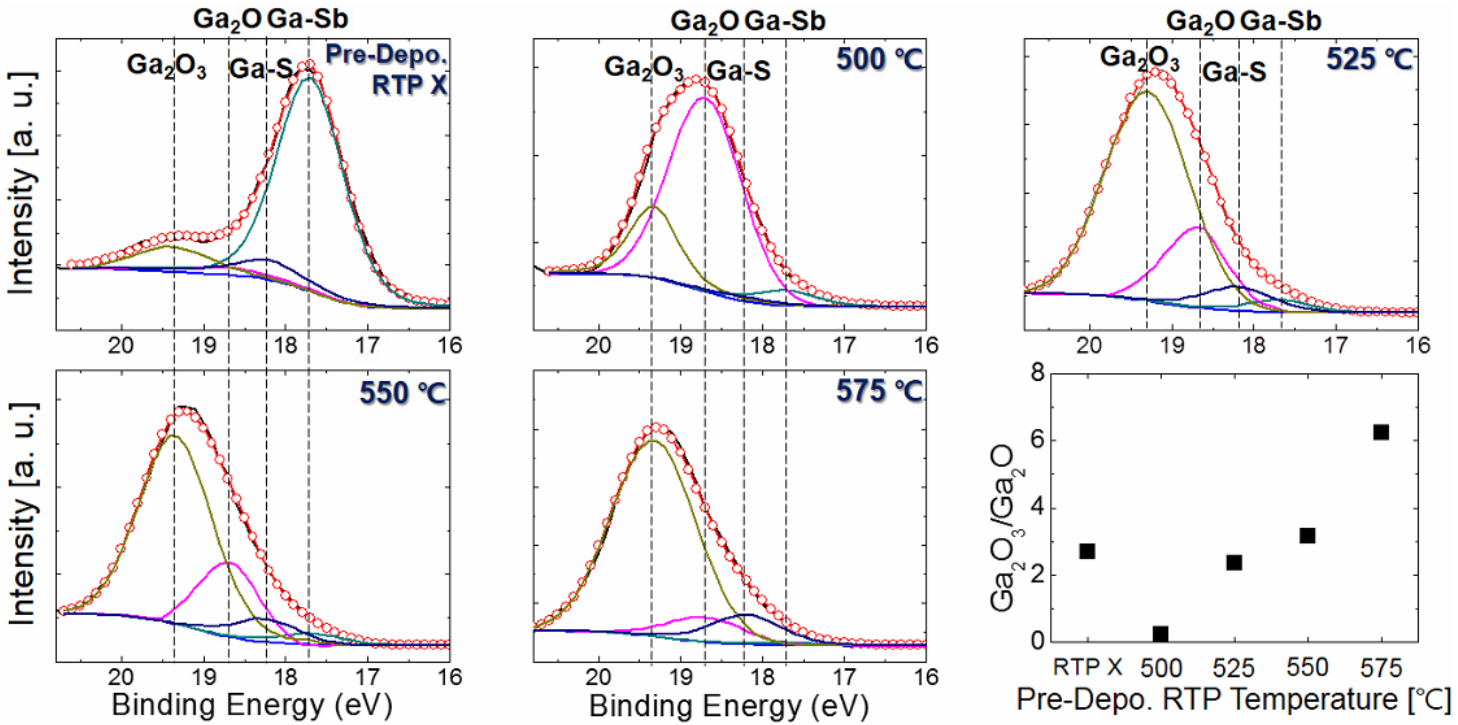

Figure 6.6 XPS spectra of Ga 3d for 2 nm thick Al_2O_3 on GaSb. The right bottom shows the effects of the pre-deposition RTP temperature in a nitrogen ambience on the ratio of Ga_2O_3 over Ga2O.

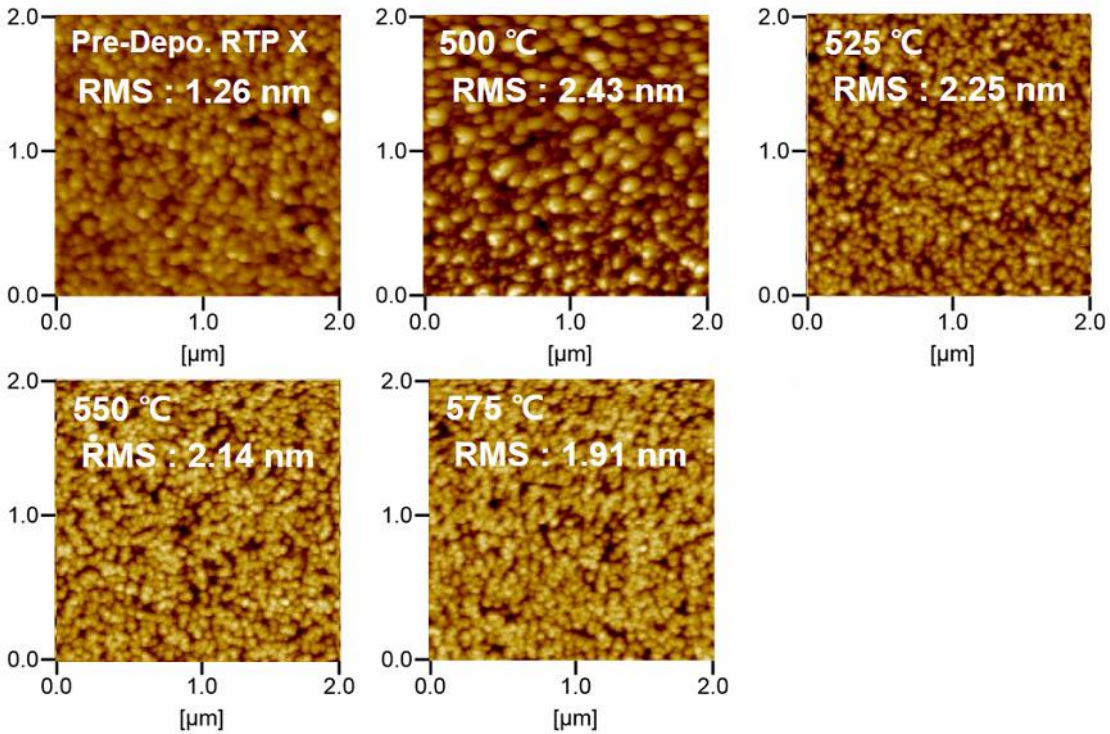

Figure 6.7 AFM analysis results of 10 nm thick Al_2O_3 on GaSb after the pre-deposition RTP in a nitrogen ambience at various temperatures for 30 seconds.

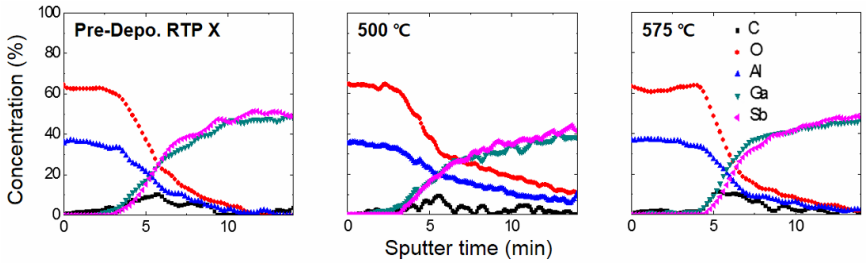

Figure 6.8 AES analysis results of 10 nm thick Al_2O_3 on GaSb after the pre-deposition RTP in a nitrogen ambience at various temperatures for 30 seconds.

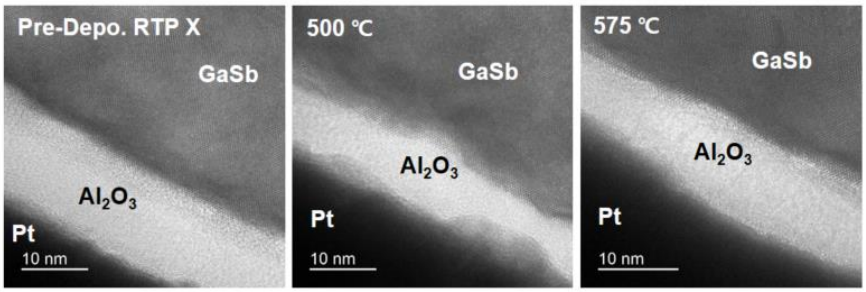

Figure 6.9 TEM images of 10 nm thick Al_2O_3 on GaSb after the pre-deposition RTP in a nitrogen ambience at various temperature for 30 seconds.

6.4. Summary

HCl is known as the most effective wet chemical to remove the native oxides of GaSb. Even with this HCl cleaning, there are still remaining antimony oxides because Sb_2O_5 does not dissolve in dilute HCl. Thermal desorption and diffusion out of Sb-oxides and elemental Sb occur at a high temperature annealing in an UHV system. Instead of setting an UHV system, RTP was chosen because the fast temperature control was available with it and also it was a facile route to do so. Prior to deposit gate oxide on GaSb, GaSb was annealed in the RTP chamber after wet chemical cleaning to get rid of the native oxides. The pre-deposition RTP for Al_2O_3/GaSb MOS capacitors was firstly introduced by this author. The stretch-out in the C-V curves was significantly improved and the D_{it} level was strikingly reduced by the pre-deposition RTP at 550 and 575 ℃. It is resulted from the increased ratio of Ga_2O_3 over Ga_2O that were proven by XPS peak deconvolution (Ga3d peak). The formation of Ga_2O_3 was enhanced by the pre-deposition RTP because the Sb-O bonds were broken by thermal energy. The broken Sb-O bonds leaved liberated Sb and this liberated Sb was diffused out. An oxygen rich-environment was finally generated by this series of reactions and formed Ga_2O_3 layer, which makes a low defect interface with GaSb. The D_{it} value was decreased by the pre-deposition RTP at 550 and 575 ℃ and the lowest value was 1.06×10^{12} $cm^{-2}eV^{-1}$ at $E\text{-}E_v$=0.004 eV. The D_{it} value was the lowest among the ones of other sulfur treated GaSb MOS capacitors in literature.

However, the stertch out in the C-V curves deteriorated with the pre-deposition RTP at 500 and 525 ℃. It is resulted from the decreased ratio of pure Ga_2O_3 over meta stable Ga_2O that were proven by XPS peak deconvolution (Ga3d peak). It indicates that the oxidation of GaSb was accelerated by the pre-deposition RTP at 500 ℃. It was also supported by AFM, AES, and TEM analysis. From the AFM analysis results, the surface roughness increased by the pre-deposition RTP at 500 ℃. The increased roughness had an impact on the C-V curve because the increased roughness formed high

structure disorder which made structural defects. In AES analysis results, the interlayer between Al_2O_3 and GaSb was lengthened by the pre-deposition RTP at 500 ℃. Also the Al and O diffused towards the substrate deeply. The interface layer is also known to aggravate C-V curves. The TEM images also showed that the interface roughness increased by the pre-deposition RTP at 500 ℃.

7. Conclusion

In conclusion, alleviating the stretch-out in the C-V curves is successfully achieved by various surface treatments (figure.7.1). Also the deterioration of the C-V curves by the hydrogen annealing was discussed.

The fast oxidation of GaSb with air exposure was the main cause for the stretch-out in the C-V curves and the Fermi-level pinning behavior. To improve the electrical properties, four different parts of experiments had been conducted.

Since a hot chamber accelerated the oxidation of GaSb, deposition temperature was lowered. By lowering the deposition temperature to 150 ℃ from 310 ℃, the stretch-out in the C-V curves was alleviated and the D_{it} value was reduced. It is resulted from the prevention of the formation of meta-stable Ga_2O that is normally made by abrupt oxidation of GaSb. The formula of the oxidation of GaSb is as follow.

$$GaSb + O_2 \rightarrow Ga_xO_y + Sb_{x'}O_{y'}$$

To reduce the D_{it} level, the post-deposition annealing of Al_2O_3 on GaSb was implemented in a nitrogen ambience and a hydrogen including gas ambience at various temperatures. The stretch-out in the C-V curves was alleviated and the D_{it} value was reduced by the post-deposition annealing in a nitrogen ambience at 250 ℃. It was resulted from the reconstruction of meta-stable Ga_2O to pure Ga_2O_3. However, the stretch-out in the C-V curves deteriorated and the D_{it} value was increased by the post-deposition annealing in a hydrogen including gas ambience. It was resulted from the reduction of the pure Ga_2O_3 to the meta-stable Ga_2O. To prove this, the extra experiment that doubled the hydrogen flux

was performed. The reduction formula is as below.

$Ga_2O_3 + 2H_2 \rightarrow Ga_2O + 2H_2O \uparrow$.

Sulfuric passivation was implemented to prevent the further oxidation of GaSb after HCl cleaning. GaSb samples were immersed in a 5 % $(NH_4)_2S$ solution for various times. The stretch-out of the C-V curve was alleviated and the D_{it} value was reduced by immersing GaSb in a 5 % $(NH_4)_2S$ solution for 5 minutes. It was due to the increased ratio of pure Ga_2O_3 over meta-stable Ga_2O. However, the C-V curves deteriorated as the immersion time increased. It was resulted from the chemical etching of GaSb by NH_4OH which was made once $(NH_4)_2S$ met water. The AFM results showed that the surface roughness was increased by longer immersion time. The AES analysis the interlayer between Al_2O_3 and GaSb was lengthened and Al and O diffused towards GaSb deeply by longer immersion time. The XPS results showed that the Ga-oxide was decreased by the sulfuric passivation. Overall, immersing the samples longer than 5 minutes induced high surface roughness with fewer native oxides. The related formulas are as follow.

$$(NH_4)_2S + H_2O \rightarrow NH_4OH + NH_4SH$$

$$GaSb + NH_4OH \rightarrow GaO_x + SbO_y + NH_4 + H_2$$

$$SbO_x + NH_4SH \rightarrow SbS_y + NH_4OH$$

$$GaO_x + NH_4SH \rightarrow GaS_y + NH_4OH$$

Finally, the pre-deposition RTP on GaSb was firstly introduced by this author.

The most effective chemical, HCl, cannot eliminate Sb-oxide completely as mentioned already, so it is necessary to adopt an extra procedure to get rid of the remaining native oxides. The Sb-oxide and elemental Sb are thermally desorbed and diffuse out at a high temperature in an UHV system. Instead of setting an UHV system, the RTP was implemented to do so. Prior to deposit gate oxide on GaSb, GaSb was annealed in a RTP chamber for 30 seconds in a nitrogen ambience at various temperatures after chemical cleaning. The stretch-out in the C-V curves was successfully alleviated and the D_{it} level was reduced by the pre-deposition RTP at 550 and 575 ℃. The lowest D_{it} value was 1.06 x 10^{12} $cm^{-2}eV^{-1}$ at $E\text{-}E_v$ = 0.004 eV by the pre-deposition RTP at 575 ℃. This value is the lowest among the ones in other sulfur treated GaSb MOS capacitors in literature. It is resulted from the increased ratio of the pure Ga_2O_3 over the meta-stable Ga_2O which were shown in XPS peak deconvolution. The broken Sb-O bonds by thermal energy leaved liberated Sb and the liberated Sb desorbed as elemental Sb since there was no extra Sb flux. It made an oxygen rich environment to form Ga_2O_3 layer. The Ga_2O_3 layer is known to make a low-defect interface with GaSb.

However, the stretch-out in the C-V curves deteriorated by the pre-deposition RTP at 500 and 525 ℃. It was because of the accelerated oxidation of GaSb. It was supported by the AFM, AES, and TEM analysis. The AFM results showed that surface roughness was increased by the pre-deposition RTP at 500 ℃. The increased surface roughness caused high structural disorder that formed structural defects. In the AES results, the interlayer between Al_2O_3 and GaSb was lengthened and Al and O diffused towards GaSb deeply by the pre-deposition RTP at 500 ℃. The TEM images also showed that the interface roughness was increased by the pre-deposition RTP at 500 ℃.

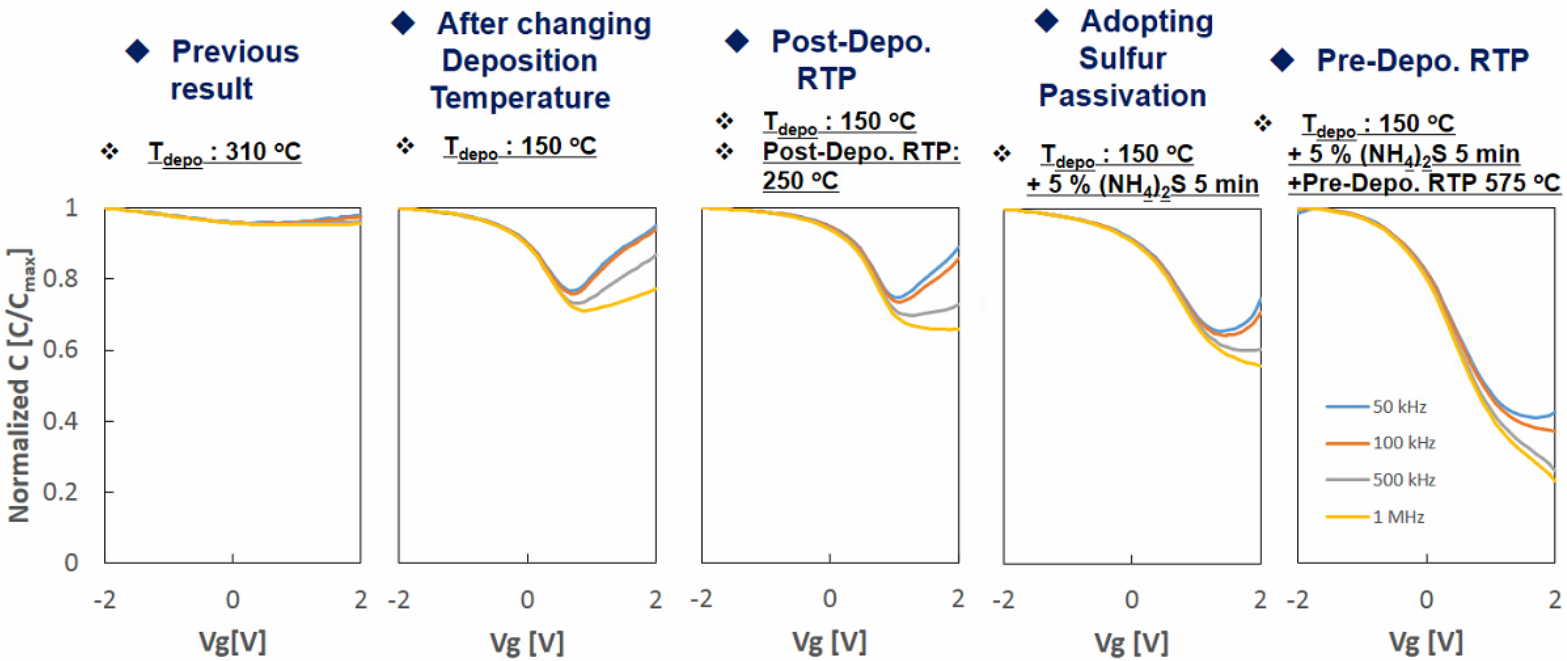

Figure 7.1 The improved stretch-out in the C-V curves by four different experimental parts.

8. References

[1] ERDGroup(ITRS) https://www.dropbox.com/sh/5yyp1h60uyjh6o5/AAB6FG1A4ZfMNFYqTmEBvwrqa?dl=0&preview=6_1507_12_Beyond+CMOS.pdf (accessed 2017 April 17th).

[2] Hausmann, D. M.; Kim, E.; Becker, J.; Gordon, R. G., *Chemistry of Materials* **14** (2002), 4350-4358.

[3] Hurley, P.; Cherkaoui, K. Microelectronics, 2006 25th International Conference on)IEEE: pp 53-58.

[4] Robertson, J., *The European physical journal applied physics* **28** (2004), 265-291.

[5] Huang, F.; Chu, M.; Tanner, M.; Wang, K.; U'Ren, G.; Goorsky, M., *Applied Physics Letters* **76** (2000), 2680-2682.

[6] Wilk, G. D.; Wallace, R. M.; Anthony, J., *Journal of Applied Physics* **89** (2001), 5243-5275.

[7] Triyoso, D.; Hegde, R.; Zollner, S.; Ramon, M.; Kalpat, S.; Gregory, R.; Wang, X.-D.; Jiang, J.; Raymond, M.; Rai, R., *Journal of Applied Physics* **98** (2005), 054104.

[8] Powell, A.; Iyer, S.; LeGoues, F., *Applied Physics Letters* **64** (1994), 1856-1858.

[9] Wong, H.; Iwai, H., *Microelectronic Engineering* **83** (2006), 1867-1904.

[10] Triyoso, D. H.; Hegde, R. I.; White Jr, B. E.; Tobin, P. J., *Journal of Applied Physics* **97** (2005), 124107.

[11] Kim, Y.-H.; Lee, J. C., *Microelectronics Reliability* **44** (2004), 183-193.

[12] Ribes, G.; Mitard, J.; Denais, M.; Bruyere, S.; Monsieur, F.; Parthasarathy, C.; Vincent, E.; Ghibaudo, G., *IEEE Transactions on Device and materials Reliability* **5** (2005), 5-19.

[13] Mooney, P., *Materials Science and Engineering: R: Reports* **17** (1996), 105-146.

[14] Kuhn, K. J., *IEEE Transactions on Electron Devices* **59** (2012), 1813-1828.

[15] ITRS https://www.semiconductors.org/clientuploads/Research_Technology/ITRS/2015/0_2015%20ITRS%202.0%20Executive%20Report%20(1).pdf (accessed 2017-April-14th).

[16] Thompson, S. Intel Technology Journal)Citeseer: 1998.

[17] He, W.; Schuetz, S.; Solanki, R.; Belot, J.; McAndrew, J., *Electrochemical and Solid-State Letters* **7** (2004), G131-G133.

[18] Chen, F.; Bin, X.; Hella, C.; Shi, X.; Gladfelter, W.; Campbell, S., *Microelectronic Engineering* **72** (2004), 263-266.

[19] Clark, R. D., *Materials* **7** (2014), 2913-2944.

[20] Yu, B.; Chang, L.; Ahmed, S.; Wang, H.; Bell, S.; Yang, C.-Y.; Tabery, C.; Ho, C.; Xiang, Q.; King, T.-J. Electron Devices Meeting, 2002. IEDM'02. International)IEEE: 2002; pp 251-254.

[21] Hisamoto, D.; Lee, W.-C.; Kedzierski, J.; Takeuchi, H.; Asano, K.; Kuo, C.; Anderson, E.; King, T.-J.; Bokor, J.; Hu, C., *IEEE Transactions on Electron Devices* **47** (2000), 2320-2325.

[22] Ferain, I.; Colinge, C. A.; Colinge, J.-P., *Nature* **479** (2011), 310-316.

[23] Choi, Y.-K.; Lindert, N.; Xuan, P.; Tang, S.; Ha, D.; Anderson, E.; King, T.-J.; Bokor, J.; Hu, C. Electron Devices Meeting, 2001. IEDM'01. Technical Digest. International)IEEE: 2001; pp 19.1. 1-19.1. 4.

[24] Nowak, E. J.; Aller, I.; Ludwig, T.; Kim, K.; Joshi, R. V.; Chuang, C.-T.; Bernstein, K.; Puri, R., *IEEE Circuits and Devices Magazine* **20** (2004), 20-31.

[25] Suzuki, R.; Taoka, N.; Yokoyama, M.; Lee, S.; Kim, S.; Hoshii, T.; Yasuda, T.; Jevasuwan, W.; Maeda, T.; Ichikawa, O., *Applied Physics Letters* **100** (2012), 132906.

[26] Chadi, D., *Journal of Vacuum Science & Technology A: Vacuum, Surfaces, and Films* **5** (1987), 834-837.

[27] Antoniadis, D. A.; Aberg, I.; Chleirigh, C. N.; Nayfeh, O. M.; Khakifirooz, A.; Hoyt, J. L., *IBM Journal of Research and Development* **50** (2006), 363-376.

[28] Ye, P.; Wilk, G.; Yang, B.; Kwo, J.; Chu, S.; Nakahara, S.; Goss

mann, H.-J.; Mannaerts, J.; Hong, M.; Ng, K., *Applied Physics Letters* **83** (2003), 180-182.

[29] Bai, W.; Lu, N.; Liu, J.; Ramirez, A.; Kwong, D.; Wristers, D.; R itenour, A.; Lee, L.; Antoniadis, D. VLSI Technology, 2003. Digest of Technical Papers. 2003 Symposium on)IEEE: 2003; pp 121-122.

[30] Chui, C. O.; Ramanathan, S.; Triplett, B. B.; McIntyre, P. C.; Sara swat, K. C., *IEEE Electron Device Letters* **23** (2002), 473-475.

[31] Zhang, J. Purdue University, (2015).

[32] Zhang, R.; Iwasaki, T.; Taoka, N.; Takenaka, M.; Takagi, S., *Micro electronic Engineering* **88** (2011), 1533-1536.

[33] Xie, Q.; Deduytsche, D.; Schaekers, M.; Caymax, M.; Delabie, A.; Qu, X.-P.; Detavernier, C., *Applied Physics Letters* **97** (2010), 112905.

[34] Lee, K.-W.; Sze, P.-W.; Lin, Y.-J.; Yang, N.-Y.; Houng, M.-P.; Wan g, Y.-H., *IEEE Electron Device Letters* **26** (2005), 864-866.

[35] Ye, P. D., *Journal of Vacuum Science & Technology A: Vacuum, S urfaces, and Films* **26** (2008), 697-704.

[36] Svarnas, P.; Botzakaki, M.; Skoulatakis, G.; Kennou, S.; Ladas, S.; Tsamis, C.; Georga, S.; Krontiras, C., *Thin Solid Films* **599** (2016), 49-53.

[37] Murthy, M. K.; Aguayo, J., *Journal of the American Ceramic Soci ety* **47** (1964), 444-447.

[38] Murthy, M.; Long, L.; Ip, J., *Journal of the American Ceramic So ciety* **51** (1968), 661-662.

[39] Posthuma, N.; Flamand, G.; Geens, W.; Poortmans, J., *Solar energ y materials and solar cells* **88** (2005), 37-45.

[40] Xu, M.; Wang, R.; Ye, P. D., *Electron Device Letters, IEEE* **32** (2 011), 883-885.

[41] del Alamo, J. A., *Nature* **479** (2011), 317-323.

[42] Basu, S.; Basu, N.; Barman, P., *Materials Science and Engineering: B* **9** (1991), 47-50.

[43] Matsubara, H.; Sasada, T.; Takenaka, M.; Takagi, S., *Applied Physi cs Letters* **93** (2008), 032104.

[44] Kuzum, D.; Krishnamohan, T.; Pethe, A. J.; Okyay, A. K.; Oshim a, Y.; Sun, Y.; McVittie, J. P.; Pianetta, P. A.; McIntyre, P. C.; Saraswa t, K. C., *IEEE Electron Device Letters* **29** (2008), 328-330.

[45] He, G.; Liu, J.; Chen, H.; Liu, Y.; Sun, Z.; Chen, X.; Liu, M.; Z hang, L., *Journal of Materials Chemistry C* **2** (2014), 5299-5308.

[46] Siddiqui, J. J. University of Michigan, (2012).

[47] Mizokawa, Y.; Komoda, O.; Miyase, S., *Thin Solid Films* **156** (19 88), 127-143.

[48] Da Silva, S.; Rolim, G. K.; Soares, G. V.; Baumvol, I. J. R.; Kru g, C.; Miotti, L.; Freire Jr, F.; da Costa, M.; Radtke, C., *Applied Physi cs Letters* **100** (2012), 191907.

[49] Perotin, M.; Coudray, P.; Gouskov, L.; Luquet, H.; Llinares, C.; B onnet, J.; Soonckindt, L.; Lambert, B., *Journal of Electronic Materials* **23** (1994), 7-12.

[50] Tsunoda, K.; Matsukura, Y.; Suzuki, R.; Aoki, M. SPIE Defense+ Security)International Society for Optics and Photonics: 2016; pp 98190 S-98190S-6.

[51] Butcher, D.; Sealy, B., *Journal of Physics D: Applied Physics* **11** (1978), 1451.

[52] Koshiga, F.; Sugano, T., *Japanese Journal of Applied Physics* **16** (1977), 465.

[53] Barman, P.; Basu, S., *Applied Surface Science* **55** (1992), 173-177.

[54] Navratil, K., *Czechoslovak Journal of Physics* **18** (1968), 266-274.

[55] Barman, P.; Basu, N.; Basu, S., *Semiconductor Science and Techno logy* **6** (1991), 129.

[56] Koveshnikov, S.; Adamo, C.; Tokranov, V.; Yakimov, M.; Kambha mpati, R.; Warusawithana, M.; Schlom, D.; Tsai, W.; Oktyabrsky, S., *Ap plied Physics Letters* **93** (2008), 012903.

[57] Martens, K.; Wang, W. F.; Dimoulas, A.; Borghs, G.; Meuris, M.; Groeseneken, G.; Maes, H. E., *Solid-State Electronics* **51** (2007), 1101-1 108.

[58] Ali, A.; Madan, H. S.; Kirk, A. P.; Zhao, D. A.; Mourey, D. A.;

Hudait, M. K.; Wallace, R. M.; Jackson, T. N.; Bennett, B. R.; Boos, J. B.; Datta, S., *Applied Physics Letters* **97** (2010), 143502.

[59] Lin, H.; Brammertz, G.; Martens, K.; de Valicourt, G.; Negre, L.; Wang, W.-E.; Tsai, W.; Meuris, M.; Heyns, M., *Applied Physics Letters* **94** (2009), 153508.

[60] Martens, K.; Wang, W.; De Keersmaecker, K.; Borghs, G.; Groesen eken, G.; Maes, H., *Microelectronic Engineering* **84** (2007), 2146-2149.

[61] Brudnyi, V. N.; Grinyaev, S. N.; Kolin, N. G., *Physica B: Conden sed Matter* **348** (2004), 213-225.

[62] Newman, N.; Spicer, W. E.; Kendelewicz, T.; Lindau, I., *Journal o f Vacuum Science & Technology B* **4** (1986), 931-938.

[63] Spicer, W. E.; Chye, P. W.; Garner, C. M.; Lindau, I.; Pianetta, P., *Surface Science* **86** (1979), 763-788.

[64] Ruppalt, L. B.; Cleveland, E. R.; Champlain, J. G.; Prokes, S. M.; Brad Boos, J.; Park, D.; Bennett, B. R., *Applied Physics Letters* **101** (2012), 231601.

[65] Tan, Z.; Zhao, L.; Wang, J.; Xu, J., *ECS Solid State Letters* **2** (20 13), P61-P62.

[66] Nainani, A.; Sun, Y.; Irisawa, T.; Yuan, Z.; Kobayashi, M.; Pianett a, P.; Bennett, B. R.; Brad Boos, J.; Saraswat, K. C., *Journal of Applie d Physics* **109** (2011), 114908.

[67] Tokranov, V.; Madisetti, S.; Yakimov, M.; Nagaiah, P.; Faleev, N.; Oktyabrsky, S., *Journal of Crystal Growth* **378** (2013), 631-635.

[68] Liu, Z. Y.; Hawkins, B.; Kuech, T. F., *Journal of Vacuum Science & Technology B: Microelectronics and Nanometer Structures* **21** (2003), 71.

[69] Connelly, N. G.; Geiger, W. E., *Chemical Reviews* **96** (1996), 877-910.

[70] Liu, Z. Y.; Kuech, T. F.; Saulys, D. A., *Applied Physics Letters* **8 3** (2003), 2587.

[71] Cleveland, E. R.; Ruppalt, L. B.; Bennett, B. R.; Prokes, S. M., *A pplied Surface Science* **277** (2013), 167-175.

[72] Zhao, L.; Tan, Z.; Wang, J.; Xu, J., *Applied Surface Science* **289** (2014), 601-605.

[73] Tan, Z.; Zhao, L.; Cui, N.; Wang, J.; Xu, J., (2013), 21-24.

[74] Zhao, L.; Tan, Z.; Bai, R.; Cui, N.; Wang, J.; Xu, J., *Applied Phy sics Express* **6** (2013).

[75] Peralagu, U.; Povey, I. M.; Carolan, P.; Lin, J.; Contreras-Guerrero, R.; Droopad, R.; Hurley, P. K.; Thayne, I. G., *Applied Physics Letters* **105** (2014), 162907.

[76] Lu, Z.; Jiang, Y.; Wang, W. I.; Teich, M. C.; Osgood, R. M., *Jou rnal of Vacuum Science & Technology B* **10** (1992), 1856-1861.

[77] Weiss, E.; Klin, O.; Grossman, S.; Greenberg, S.; Klipstein, P. C.; Akhvlediani, R.; Tessler, R.; Edrei, R.; Hoffman, A., *Journal of Vacuum Science & Technology A: Vacuum, Surfaces, and Films* **25** (2007), 736.

[78] Yokoyama, M.; Yokoyama, H.; Takenaka, M.; Takagi, S., *Applied Physics Letters* **106** (2015), 122902.

[79] Murape, D.; Eassa, N.; Nyamhere, C.; Neethling, J.; Betz, R.; Coet see, E.; Swart, H.; Botha, J.; Venter, A., *Physica B: Condensed Matter* **407** (2012), 1675-1678.

[80] Lian-Feng, Z.; Zhen, T.; Jing, W.; Jun, X., *Chinese Physics B* (20 14).

[81] Greene, A.; Madisetti, S.; Nagaiah, P.; Yakimov, M.; Tokranov, V.; Moore, R.; Oktyabrsky, S., *Solid-State Electronics* **78** (2012), 56-61.

[82] Zhen, T.; Lian-Feng, Z.; Jing, W.; Jun, X., *Chinese Physics B* **23** (2014), 017701.

[83] Peralagu, U.; Povey, I.; Hurley, P.; Droopad, R.; Thayne, I., (2013).

[84] Chen, C.-Y.; Hsueh, W.-J.; Chang, C.-M.; Hsu, H.-M.; Chyi, J.-I., *ECS Transactions* **66** (2015), 3-9.

[85] Perotin, M.; Coudray, P.; Gouskov, L.; Luquet, H.; Llinares, C.; B onnet, J. J.; Soonckindt, L.; Lambert, B., *Journal of Electronic Material s* **23** (1994), 7-12.

[86] Papis-Polakowska, E.; Kaniewski, J.; Szade, J.; Rzodkiewicz, W.; J asik, A.; Jurenczyk, J.; Orman, Z.; Wawro, A., *Thin Solid Films* **567** (2

014), 77-81.

[87] Eric K. Propst, K. W. V., * and Paul A. Kohl**).

[88] Lebedev, M. V.; Kunitsyna, E. V.; Calvet, W.; Mayer, T.; Jaegerma nn, W., *The Journal of Physical Chemistry C* **117** (2013), 15996-16004.

[89] Papis, E.; Piotrowska, A.; Kamińska, E.; Gołaszewska, K.; Kruszka, R.; Piotrowski, T.; Rzodkiewicz, W.; Szade, J.; Winiarski, A.; Wawro, A., *physica status solidi (c)* **4** (2007), 1448-1453.

[90] Zhernokletov, D. M.; Dong, H.; Brennan, B.; Yakimov, M.; Tokran ov, V.; Oktyabrsky, S.; Kim, J.; Wallace, R. M., *Applied Physics Letters* **102** (2013), 131602.

[91] Chu, R.-L.; Hsueh, W.-J.; Chiang, T.-H.; Lee, W.-C.; Lin, H.-Y.; L in, T.-D.; Brown, G. J.; Chyi, J.-I.; Huang, T.-S.; Pi, T.-W., *Applied Ph ysics Express* **6** (2013), 121201.

[92] Murape, D. M.; Eassa, N.; Neethling, J. H.; Betz, R.; Coetsee, E.; Swart, H. C.; Botha, J. R.; Venter, A., *Applied Surface Science* **258** (20 12), 6753-6758.

[93] Möller, K.; Töben, L.; Kollonitsch, Z.; Giesen, C.; Heuken, M.; W illig, F.; Hannappel, T., *Applied Surface Science* **242** (2005), 392-398.

[94] Vineis, C. J.; Wang, C. A.; Jensen, K. F., *Journal of Crystal Gro wth* **225** (2001), 420-425.

[95] Lin, Chuing L.; Su, Yan K.; Se, Than S.; Li, Wen L., *Japanese Jou rnal of Applied Physics* **37** (1998), L1543.

[96] Barin, I., VCH: Germany, (1989).

[97] McDonnell, S.; Brennan, B.; Bursa, E.; Wallace, R. M.; Winkler, K.; Baumann, P., *Journal of Vacuum Science & Technology B* **32** (201 4).

[98] Dutta, P.; Bhat, H.; Kumar, V., *Journal of Applied Physics* **81** (19 97), 5821-5870.

[99] hori, T., New York, (1997)Vol. Springer-Verlag.

[100] Zazo, L. G.; Montojo, M.; Castano, J.; Piqueras, J., *Journal of th e Electrochemical Society* **136** (1989), 1480-1484.

[101] Propst, E. K.; Vogt, K. W.; Kohl, P. A., *Journal of the Electroch*

emical Society **140** (1993), 3631-3635.

[102] Papis, E.; Kudła, A.; Piotrowski, T. T.; Gołaszewska, K.; Kamińs ka, E.; Piotrowska, A., *Materials Science in Semiconductor Processing* **4** (2001), 293-295.

[103] Papis-Polakowska, E., *Electron Technology* **37-38** (2005), 1-34.

[104] Hwang, E.; Eaton, C.; Mujumdar, S.; Madan, H.; Ali, A.; Bhatia, D.; Datta, S.; Ruzyllo, J., *ECS Transactions* **41** (2011), 157-162.

[105] Nainani, A.; Irisawa, T.; Yuan, Z.; Bennett, B. R.; Boos, J. B.; N ishi, Y.; Saraswat, K. C., *IEEE Transactions on Electron Devices* **58** (2 011), 3407-3415.

[106] Cotirlan, C.; Ghita, R. V.; Negrila, C. C.; Logofatu, C.; Frumosu, F.; Lungu, G. A., *Applied Surface Science* **363** (2016), 83-90.

[107] Ruppalt, L. B.; Cleveland, E. R.; Champlain, J. G.; Bennett, B. R.; Boos, J. B.; Prokes, S. M., *Journal of Vacuum Science & Tech nology B* **33** (2015), 04E102.

[108] Polyakov, A. Y.; Milnes, A. G.; Li, X.; Balmashnov, A. A.; Smir nov, N. B., *Solid-State Electronics* **38** (1995), 1743-1745.

[109] Liu, Z. Y.; Kuech, T. F.; Saulys, D. A., *Applied Physics Letters* **83** (2003), 2587-2589.

[110] Liu, Z. Y.; Saulys, D. A.; Kuech, T. F., *Applied Physics Letters* **85** (2004), 4391.

[111] McDonnell, S.; Zhernokletov, D. M.; Kirk, A. P.; Kim, J.; Wallac e, R. M., *Applied Surface Science* **257** (2011), 8747-8751.

[112] An, N.; Liu, G.; Wei, Z.; Li, M.; Fang, F.; Fang, X.; Hao, Y.; L i, Z.; Sui, Q.; Zhang, Z.; Qu, Y., *Integrated Ferroelectrics* **136** (2012), 147-155.

[113] Ning, A.; Guojun, L.; Zhipeng, W.; Rui, D.; Xuan, F.; Xian, G.; Yonggang, Z.; Mei, L.; Xiaohui, M. Optoelectronics and Microelectronic s (ICOM), 2012 International Conference on, (23-25 Aug. 2012)2012; p p 25-29.

[114] Plis, E. A.; Kutty, M. N.; Myers, S.; Rathi, A.; Aifer, E. H.; Vur gaftman, I.; Krishna, S., *Infrared Physics & Technology* **55** (2012), 216-

219.

[115] Wang, B.; Wei, Z.; Li, M.; Liu, G.; Zou, Y.; Xing, G.; Tan, T. T.; Li, S.; Chu, X.; Fang, F.; Fang, X.; Li, J.; Wang, X.; Ma, X., *Chemical Physics Letters* **556** (2013), 182-187.

[116] Wang, B.; Zhipengwei; Li, M.; Li, X.; Fang, X.; Gao, X.; Zou, Y.; Lu, P.; Liu, G.; Ma, X., *Integrated Ferroelectrics* **146** (2013), 110-114.

[117] George, S. M., *Chemical Reviews* **110** (2009), 111-131.

[118] Higashi, G.; Fleming, C., *Applied Physics Letters* **55** (1989), 1963-1965.

[119] Soto, C.; Tysoe, W., *Journal of Vacuum Science & Technology A: Vacuum, Surfaces, and Films* **9** (1991), 2686-2695.

[120] Goldstein, D. N.; McCormick, J. A.; George, S. M., *The Journal of Physical Chemistry C* **112** (2008), 19530-19539.

[121] Kim, J.; Kwon, D.; Chakrabarti, K.; Lee, C.; Oh, K.; Lee, J., *Journal of Applied Physics* **92** (2002), 6739-6742.

[122] George, S.; Ott, A.; Klaus, J., *The Journal of Physical Chemistry* **100** (1996), 13121-13131.

[123] Ott, A.; Klaus, J.; Johnson, J.; George, S., *Thin Solid Films* **292** (1997), 135-144.

[124] Dillon, A.; Ott, A.; Way, J.; George, S., *Surface Science* **322** (1995), 230-242.

[125] Chemistry, H., 5.11 edition; Outokumpu Research Oy: Pori, Finland. Values are given at 0 ^{o}C.

[126] Groner, M. D.; Fabreguette, F. H.; Elam, J. W.; George, S. M., *Chemistry of Materials* **16** (2004), 639-645.

[127] Fairfield, J. M.; Schwuttke, G., *Solid-State Electronics* **11** (1968), 1175IN5-1176IN6.

[128] Singh, R., *Journal of Applied Physics* **63** (1988), R59-R114.

[129] Hart, M.; Evans, A., *Semiconductor Science and Technology* **3** (1988), 421.

[130] Gibbons, J. F.; Sigmon, T.; Hess, L. D., North Holland: (1981)Vo

l. 1.

[131] Hill, C.; Jones, S.; Boys, D.; Levy, R., Reduced thermal processi ng for ULSI. Plenum Press, New York: (1989).

[132] Fair, R. B., Academic Press: (2012).

[133] Jones, K. S.; Prussin, S.; Weber, E., *Applied Physics A: Materials Science & Processing* **45** (1988), 1-34.

[134] Vandervorst, W.; Houghton, D.; Shepherd, F.; Swanson, M.; Plattn er, H.; Carpenter, G., *Canadian Journal of Physics* **63** (1985), 863-869.

[135] Sadana, D.; Washburn, J.; Booker, G., *Philosophical Magazine B* **46** (1982), 611-633.

[136] Tan, T.-Y., *Philosophical Magazine A* **44** (1981), 101-125.

[137] Tan, T.; Föll, H.; Hu, S., *Philosophical Magazine A* **44** (1981), 1 27-140.

[138] Krakow, W.; Tan, T.; Foell, H., *North Holland-New York* **2** (198 1), 173.

[139] Narayan, J.; Fletcher, J.; White, C.; Christie, W., *Journal of Appli ed Physics* **52** (1981), 7121-7128.

[140] Rozgonyi, G. A., Academic Press, Orlando: (1992).

[141] Bartsch, H.; Hoehl, D.; Kästner, G., *physica status solidi (a)* **83** (1984), 543-551.

[142] Wu, W. K.; Washburn, J., *Journal of Applied Physics* **48** (1977), 3742-3746.

[143] Hoehl, D.; Bartsch, H., *physica status solidi (a)* **112** (1989), 419-424.

[144] Sadana, D.; Washburn, J.; Magee, C., *Journal of Applied Physics* **54** (1983), 3479-3484.

[145] Prussin, S.; Margolese, D. I.; Tauber, R. N.; Hewitt, W. B., *Jour nal of Applied Physics* **56** (1984), 915-923.

[146] Kim, Y.; Massoud, H. Z.; Fair, R. B., *Applied Physics Letters* **53** (1988), 2197-2199.

[147] Carter, C.; Maszara, W.; Sadana, D.; Rozgonyi, G.; Liu, J.; Wort man, J., *Applied Physics Letters* **44** (1984), 459-461.

[148] Sands, T.; Washburn, J.; Gronsky, R.; Maszara, W.; Sadana, D.; Rozgonyi, G., *Applied Physics Letters* **45** (1984), 982-984.

[149] Cerofolini, G.; Meda, L.; Queirolo, G.; Armigliato, A.; Solmi, S.; Nava, F.; Ottaviani, G., *Journal of Applied Physics* **56** (1984), 2981-298 3.

[150] Rozgonyi, G.; Myers, E.; Sadana, D., *Proc. Series* **86** (1986), 4.

[151] Ajmera, A.; Rozgonyi, G., *Applied Physics Letters* **49** (1986), 126 9-1271.

[152] Wen, D.; Smith, P.; Osburn, C.; Rozgonyi, G., *Applied Physics L etters* **51** (1987), 1182-1184.

[153] Jones, K. S.; Prussin, S.; Weber, E., *Journal of Applied Physics* **6 2** (1987), 4114-4117.

[154] Sedgwick, T., *Journal of the Electrochemical Society* **130** (1983), 484-493.

[155] Seidel, T.; Lischner, D.; Pai, C.; Knoell, R.; Maher, D.; Jacobson, D., *Nuclear Instruments and Methods in Physics Research Section B: Beam Interactions with Materials and Atoms* **7** (1985), 251-260.

[156] Montillo, F.; Balk, P., *Journal of the Electrochemical Society* **118** (1971), 1463-1468.

[157] Razouk, R. R.; Deal, B. E., *Journal of the Electrochemical Societ y* **126** (1979), 1573-1581.

[158] the Terman, L. M., *Solid-State Electronics* **5** (1962), 285-299.

[159] Passlack, M.; Hong, M.; Mannaerts, J., *Solid-State Electronics* **39** (1996), 1133-1136.

[160] Hong, M.; Mannaerts, J.; Bower, J.; Kwo, J.; Passlack, M.; Hwan g, W.-Y.; Tu, L., *Journal of Crystal Growth* **175** (1997), 422-427.

[161] Passlack, M.; Droopad, R.; Fejes, P.; Wang, L., *IEEE Electron D evice Letters* **30** (2009), 2-4.

[162] Cheng, C.-W.; Apostolopoulos, G.; Fitzgerald, E. A., *Journal of A pplied Physics* **109** (2011), 023714.

[163] Lin, C.; Chiu, H.; Chiang, T.; Chang, Y.; Lin, T.; Kwo, J.; Wang, W.-E.; Dekoster, J.; Heyns, M.; Hong, M., *Journal of Crystal Growth*

323 (2011), 99-102.

[164] Ide, Y.; Yamada, M., *Journal of Vacuum Science & Technology A: Vacuum, Surfaces, and Films* **12** (1994), 1858-1863.

[165] Hirsch, L.; Yu, Z.; Buczkowski, S.; Myers, T.; Richards-Babb, M., *Journal of Electronic Materials* **26** (1997), 534.

[166] Allwood, D. A.; Mason, N. J.; Walker, P. J., *Journal of Crystal Growth* **195** (1998), 163-167.

[167] Lee, K.-K.; Doyle, K.; Chai, J.; Dinan, J. H.; Myers, T. H., *Jour nal of Electronic Materials* **41** (2012), 2799.

Abstract (in Korean)

갈륨안티모나이드 (GaSb) 는 차세대 나노 스케일 로직 금속 산화물 반도체 전계효과 트랜지스터 (MOSFETs) 용 채널 물질로 많은 주목을 받아오고 있는데 그 이유는 현존하는 규소 기반의 소자에 비한 GaSb 의 뛰어난 홀 이동도 (~ 3000 cm^2/Vs) 와 자연산화막의 물에 대한 화학적 저항성, 높은 준위 유효 밀도 (1.8 x 10^{19} cm^{-3}) 때문이다. 그러나 높은 계면 준위 등의 MOSFETs 에 GaSb 를 적용하기에는 단점이 존재한다. 높은 계면 준위 때문에 III-V 족 채널 물질을 적용한 MOSFETs 소자를 작동할 때 페르미 레벨 피닝 현상이 일어나고 이것에 의해 문제점들 중 하나인 축전-전압 측정에서의 늘어짐 현상 (stretch-out) 이 일어나게 된다. 페르미 레벨 피닝은 특히나 GaSb 의 산소에의 노출에 의한 자연산화막과 자연상태의 안티모니(Sb)에 의해서 온다. 갈륨안티모나이드는 공기중의 노출에 의해 매우 빠르게 자연산화막을 형성하는 것으로 알려져 있고, 이것에 의해 자연산화막을 줄이는데 어려움이 있다.

이 연구에서는, GaSb 금속-산화막-반도체 (MOS) 축전지를 저온 원자층 증착(ALD)을 통해 만들었다. 전기적 특성은 축전량-전압 (C-V) 진동수 분산에 의해 평가되었고 계면 트랩 밀도 (D_{it}) 는 털만 (the Terman) 방법에 의해 평가되었다. 계면 분석은 성분, 거칠기, 두께, 밀도를 오제 전자 분광학 (AES), 분광기를 이용한 조사의 타원편광 해석법 (SE), 엑스레이 반사 측정 (XRR), 원자력현미경 (AFM), 엑스레이 광전자 분광학 (XPS), 투과 전자 현미경 (TEM) 을 이용하여 수행하였다.

저온 ALD 를 산화규소(Al_2O_3)를 게이트 산화막으로 GaSb 기판 위에 증착하기 위해서 다양한 증착 공정 온도 (100 ~ 310 ℃)에서 사용하였다. 150 ℃의 저온 ALD 를 이용하여 D_{it} 레벨이 낮아졌고

페르미 레벨 피닝 거동이 C-V 곡선에서 완화된 것을 보였다. XPS 결과를 통해, 150 ℃의 저온 ALD 를 이용하여 준안정적 Ga_2O 에 대한 순수한 Ga_2O_3 의 비율이 증착온도가 감소할수록 증가하는 것을 보였다. C-V 곡선은 100 ℃의 낮은 온도 ALD 에 의해 더 악화되었다. 이것은 XRR 결과로 설명이 되는데, XRR 결과에서는 100 ℃의 낮은 온도 ALD 에 의해 Al_2O_3 의 밀도가 많이 감소한 것을 보였다.

D_{it} 를 줄이기 위해, 후증착 열처리 공정이 Al_2O_3 증착 후에 질소분위기에서 다양한 온도 (150 ~ 300 ℃) 로 30 초 동안 적용되었다. C-V 곡선의 늘어짐은 250 ℃의 후증착 고속 열적 공정 (RTP)에 의해 완화 되었지만 300 ℃의 RTP 로는 C-V 곡선이 오히려 더 늘어짐이 보였다. 거칠기는 RTP 온도가 증가할수록 감소하다가 300 ℃ 이상에서는 다시 증가하는 것을 보였다. 준안정적 Ga_2O 에 대한 순수한 Ga_2O_3 의 비율을 RTP 온도가 증가할수록 증가하다가 300 ℃ 이상의 RTP 온도에서는 다시 감소함을 보였다. D_{it} 는 계면 결과와 잘 부합한다. 성형 가스 열처리 (FGA) 은 끊어진 결합을 수소로 채움으로써 산화규소/규소 시스템에서 D_{it} 를 줄이는 효과적인 방법들 중 하나로 알려져 있다. 이러한 수소 열처리 효과를 확인하기 위해, Al_2O_3/GaSb 를 수소가 포함된 가스(5 % 수소/95 % 질소 가스와 10 % 수소/ 90 % 질소 가스)로 후증착 열처리하였다. 이 두 가지 가스를 이용한 시험에서 나온 결과를 보면, 수소 열처리에 의해 순수한 Ga_2O_3 가 준안정한 Ga_2O 로의 환원이 일어난다는 것을 알 수 있다. 준안정한 Ga_2O 에 대한 순수한 Ga_2O_3 의 비율은 공정온도가 증가하고 수소의 유입량이 증가할수록 감소하였다. 수소 열처리에 의해 준안정한 Ga_2O 에 대한 순수한 Ga_2O_3 의비율이 감소하였기 때문에 C-V 곡선의 늘어짐도 심해졌고 D_{it} 값도 심각하게 증가했다.

앞서 언급되었듯이, GaSb 는 공기노출에 의해 매우 빠르게 자연 산화막을 형성한다. 그러므로 현장외 (ex-situ) 에서 GaSb 축전기를

만들기 위해서는 부동화가 필수적으로 고려되어야 한다. GaSb 의 표면이 Ga-S 와 Sb-S 결합을 형성하면서 부동화 하여 MOS 축전기의 전기적 특성을 향상시킬 수 있기 때문에 이를 위해 황화 부동화가 선택 되었다. 각각의 샘플을 황화 용액 (5 % $(NH_4)_2S$) 에 다양한 시간 (1~15 분) 동안 담그었다. C-V 곡선의 늘어짐은 5 분 동안 황화 용액에 담금으로써 성공적으로 완화할 수 있었다. 하지만 5 분보다 더 긴 시간동안 담그면 C-V 곡선이 악화되었다. AFM 결과에서는 담금시간이 길어질수록 거칠기가 증가한 것을 보였다. 중간층 (IL) 또한 담금시간이 증가할수록 길어졌다.

염산이 GaSb 의 자연산화막을 제거하기에 가장 효과적인 습식 화합물이라고 알려져 있지만, 안티모니 산화물은 염산에 의해 완벽하게 제거되지 않는다. 남아있는 안티모니산화막은 GaSb 을 산화시켜 갈륨산화막을 만들고 스스로는 자연상태의 안티모니가 된다. 이를 위해, Al_2O_3/GaSb MOS 축전기의 전기적 특성을 개선하기 위한 전증착 RTP (질소 분위기)가 처음으로 여기에 적용 되었다. C-V 곡선의 늘어짐의 개선이 눈에 띈다. D_{it} 는 550 ℃와 575 ℃의 전증착 RTP 에 의해 효과적으로 감소하였고 이 D_{it} 값은 문헌상에서 보고된 황화 처리를 한 GaSb MOS 축전기의 D_{it} 값에 비해 가장 낮은 값을 가진다 (1.06×10^{12} $cm^{-2}ev^{-1}$ @ $E\text{-}E_v$=0.004). 페르미 레벨 피닝 현상은 500 ℃의 전증착 RTP 에 의해 악화되었다. 그 이유는 자연산화막을 만드는 화학적 반응이 500 ℃의 전증착 RTP 에 의해 가속화 되었기 때문이다. 이 가속화 된 화학적 반응은 XPS, AFM, AES, TEM 분석으로 증명되었다. 준안정한 Ga_2O 에 대한 순수한 Ga_2O_3 의 비율 역시 전기적 결과와 잘 부합한다.

결과적으로 저온 ALD, 후증착 RTP, 황화 부동화, 전증착 RTP 를 통해 C-V 곡선의 늘어짐을 유발하는 페르미 레벨 피닝 현상을 효과적으로 완화할 수 있었다.

주요어: 갈륨안티모나이드 (GaSb), 계면 준위, 페르미레벨 피닝, 갈륨 산화막 (Ga_2O_3), 자연상태의 안티모니, 원자층 증착, 황화 부동화, 전증착 고속 열적 공정

학번: 2014-30207

김 성 경